Mechanisms for Enhancing the Efficiency of Composite Semiconductor/Metal Photocatalysts

by

Paul Andrew Hernley

A dissertation submitted in partial fulfillment
of the requirements for the degree of
Doctor of Philosophy
(Chemical Engineering)
in the University of Michigan
2017

Doctoral Committee:

Professor Suljo Linic, Chair
Professor Mark A. Barteau
Associate Professor Stephen Maldonado
Professor Levi T. Thompson

Paul Andrew Hernley

ringoh@umich.edu

ORCID: 0000-0002-2631-8880

This dissertation is dedicated to Caitlyn and my family for supporting me and being patient throughout this challenging endeavor.

ACKNOWLEDGEMENTS

First of all, I would like to thank Professor Suljo Linic for being my mentor and adviser during my time at the University of Michigan. He has pushed me to become a better researcher and has helped me appreciate my abilities, which I have often failed to recognize in the past. I would also like to thank the members of my committee: Professor Mark Barteau, Associate Professor Stephen Maldonado, and Professor Levi Thompson. Their input during the later stages of this work has been valuable. Additionally, I would like to thank Professors Phillip Savage and Charles Monroe for their help early on in my PhD work.

I have worked with many students in the Linic group, and I appreciate all of my interactions with them. I would specifically like to thank David Ingram and Matthew Morabito for teaching me how to do experiments and work with the computer cluster, respectively. I'd like to thank Kevin Hu, Joe Quinn, Steven Chavez, and Devesh Shah for making things happen in the lab. I would also like to acknowledge Tim Van Cleve and Brittany Farrell. They joined the group at the same time as me and have been great friends for me both in and out of the lab.

There are a lot of people outside of the lab that have made my time in Ann Arbor great. Luke Griffith was a great workout partner and a fun dude to be around. I'd also like to acknowledge my water polo team, specifically Ian, Jack, Steven, and David. I'll always remember the road trips, beating Michigan State, and winning Big Tens. Go Blue!

Thank you to my family for supporting me through my entire education. It hasn't been easy being away from home for most of the past 12 years. I would never have learned what I am capable of without your help.

Caitlyn, it's been hard for both of us over the past 3+ years. Thank you for putting up with my inability to multitask and helping me to focus on what I can control and not on what I cannot. With the completion of my work here, I hope this means we can soon start having adventures together instead of adventures to one another.

TABLE OF CONTENTS

LIST OF FIGURES

LIST OF TABLES

LIST OF APPENDICES

ABSTRACT

The global demand for energy and the consequences of prolonged dependence on fossil fuels are present and future issues that must be addressed. Renewable and clean hydrogen produced from sunlight and water is part of the potential solution. In this dissertation, the processes involved with driving photocatalytic and photoelectrochemical water splitting reactions are investigated, with a particular focus on the hydrogen evolution reaction. The key parameters that govern these systems are identified through the development of simple and transparent models. Using a model system of a planar silicon absorber and platinum nanoparticle electrocatalysts, these key parameters are tuned to identify strategies for optimally incorporating these two components into an efficient composite system. The first part of this dissertation discusses the enhancement of light-harvesting and surface reaction rates through the embedding of the Pt electrocatalysts into the Si absorber. Through this method, the losses in the system due to reflection, parasitic absorption by Pt, and slow surface reaction rates are decreased simultaneously. The last part of this dissertation investigates the transformation of the Si/Pt and Si/electrolyte interfaces and its effect on the transport of charge to the Pt electrocatalysts.

CHAPTER 1

Introduction

1.1 Summary

The global demand for energy and the consequences of prolonged dependence on fossil fuels is discussed. The sun is identified as a potential source of energy that is largely untapped, and the concept of solar fuel generation is introduced. Finally, the structure of this dissertation is outlined.

1.2 World Energy Production/Consumption

1.2.1 Current and Future Usage

The global energy demand in 2012 was estimated to be 549 quadrillion BTU ($5.79 \cdot 10^{20}$ J), and it is expected to increase significantly in the future, with projections of a 48% increase over the next 30 years.[1] This growth is expected due to rapid development and population growth within countries that are not members of the Organization for Economic Cooperation and Development (OECD).

1.2.2 Issues with Fossil Fuels

The combustion of fossil fuels has been recognized as an unsustainable practice from both a supply and environmental impact perspective. While there is a finite amount of potential fossil fuel energy stored in the Earth's crust, it should be recognized that the adverse impact of fossil fuels on the environment is by far the most problematic issue.

The World Energy Council has compiled data to determine the reserves to production ratio (R/P) for coal, crude oil, and natural gas. This ratio can be used to estimate the longevity of given resource, assuming the rate of consumption is constant and no additional reserves are found. For coal, crude oil, and natural gas, the global R/P is >100, 56, and 55, respectively.[2] This is a simplistic approach at estimating the remaining accessible resources, but the point is this: scarcity is going to be a problem in the future. Economic principles, however, will drive decisions to focus on exploration, technological innovation, and increased renewable energy usage to overcome the problem.

The adverse effects that fossil fuels have on the environment, however, will not be naturally mitigated through economics. This impact on the environment is an imminent threat to mankind's well-being, unlike the finite nature of fossil fuels, and is a more pressing matter. The most recognized environmental effect of fossil fuel use is the emission of carbon dioxide into the atmosphere. From the year 1800 to 2012, the atmospheric concentration of CO_2 increased by nearly 40%.[3] This increase is undeniably a result of human behavior. Two arguments to support this are that both the global energy demand and population track very closely with the carbon dioxide concentration, especially post 1950, as shown in the top panels of Figure 1.1.

CO_2 is a greenhouse gas, so increased atmospheric concentrations result in elevated atmospheric temperatures. The bottom panel of Figure 1.1 demonstrates the connection between CO_2 concentration and global temperature. If the global temperature increases enough, food and water supplies will likely be threatened, coastal cities will have to deal with rising sea levels, and the frequency and intensity of natural disasters can be expected to increase.[4] To prevent this from happening, significant efforts to reduce emissions and

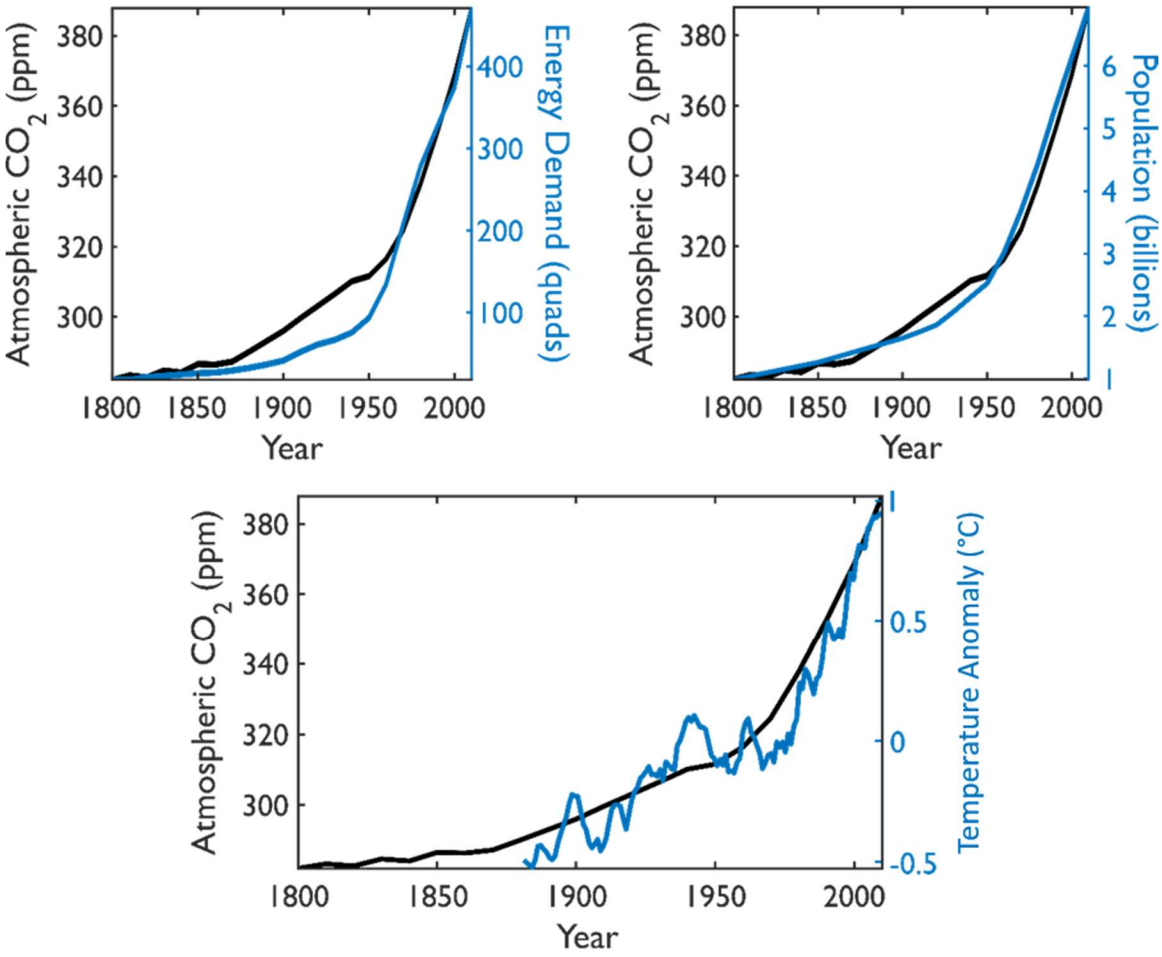

Figure 1.1: Atmospheric CO_2 trends[3] (Top Left) Correlation with global energy demand[5] (Top Right) Correlation with global population[6] (Bottom) Global land temperature anomaly using a five year running average and a 1901 to 2000 baseline[7]

capture atmospheric greenhouse gases must be developed and implemented without delay.

1.2.3 Solar Energy and Photovoltaics

Efforts are being made to develop technologies that harness sources of energy that do not emit carbon dioxide. Solar energy is one example and is a promising alternative energy source. The sun delivers energy to the Earth's surface at an average rate of ~120,000 TW. The sun is capable of supplying ample energy as this rate is more than 6000 times faster than the current rate of global energy consumption (~19 TW). Currently, silicon solar cells are the primary means of converting solar energy to electric power, but the total installed capacity only amounts to ~0.32 TW.[8]

Solar power is currently severely limited by its intermittent nature and dependence on being connected to the grid. At the moment, there are two technologies that have potential for reducing the negative impacts of these limitations: batteries and hydrogen fuel cells. The energy collected from the sun by solar cells can be stored in batteries to save for later and be used in automobiles and stationary systems. Batteries are not a perfect solution because they tend to discharge over time and, for vehicles, require long times to fully charge. Hydrogen fuel cells, however, can use a tank to store the hydrogen, which experiences minimal loss over time, and when used in vehicles, have refueling times similar to internal combustion vehicles. A major shortcoming of this technology is that most hydrogen produced today comes from natural gas. A hydrogen production method that is not dependent on fossil fuels must be developed for hydrogen fuel cells to approach carbon neutrality.

1.3 Harnessing the Sun for Solar Fuels

Finding a sustainable way to produce hydrogen is a major research goal at the moment, and the fundamental issues associated with this problem are the focus of this dissertation. In this section, photovoltaic-electrolyzers (PVE) and photocatalysts are explained as potential technologies for solar hydrogen production.

1.3.1 Photovoltaic-Electrolyzers

A PVE device combines a solar cell and a water electrolysis cell to produce hydrogen. A solar cell absorbs light, generating a potential difference across the device. In a water electrolysis cell, water is converted into hydrogen and oxygen gases by applying a potential difference across the electrodes in the cell. If the solar cell is connected to the electrolysis cell and provides enough potential to split the water, hydrogen can be produced using sunlight. Unfortunately, this method of hydrogen production is severely hindered by the same high balance of system costs associated with building PV systems and limitations by water electrolysis.

1.3.2 Photocatalysts

A photocatalyst is a material that absorbs solar energy and uses it to drive reactions at a stable rate over time. To avoid the issues that plague PVE systems, a goal of current photocatalysis research is to identify ways to perform the light absorption and water splitting processes on a single device or suspension of particles in water. The development of this technology is intended to improve upon the PVE system by significantly reducing balance of system costs.[9] The work discussed in this dissertation focuses on the understanding the fundamental principles of photocatalysts in order to provide insights for developing efficient systems.

1.4 Dissertation Scope and Organization

The adverse side effects of fossil fuel consumption can be potentially mitigated by developing a means to harness renewable and carbon neutral energy sources. The sun provides more than enough energy to easily meet all of mankind's demands. This dissertation investigates the processes involved with the generation of hydrogen fuels from sunlight, which will be especially useful in mobile and remote (off-grid) applications. The development of efficient, affordable, and stable photocatalysts that can split water is essential for this technology to be practical. The primary focus of this dissertation is to identify the key parameters that govern the individual processes in these complex photocatalytic systems and to tune these parameters to improve the performance of photocatalysts. A combination of modeling and experimental efforts are presented with this goal in mind.

After this introductory chapter, Chapter 2 discusses the physics and chemistry involved with photocatalytic systems. The properties of semiconductors, metals, and interactions between different materials are discussed and the water splitting reaction is introduced. Chapter 3 gives an overview of the experimental and computational methods involved with this research. Chapter 4 gives an in-depth explanation of the models developed to identify the governing parameters of photoelectrochemical systems. Chapter 5 discusses a case study involving silicon photocathodes and platinum nanoparticle co-catalysts. The goal of this work was to develop strategies for optimally incorporating semiconductors and metal co-catalysts to maximize their photoelectrochemical efficiency. Chapter 6 explains the importance of understanding the interfaces that are formed on the reactive face of the semiconductor photoelectrode. Experimental and computational

efforts discuss strategies for improving the interfaces to maximize efficiency. Chapter 7 concludes this dissertation, discussing the main points of this work and presents logical experimental ideas for future work using the materials involved in this research.

1.5 References

(1) U.S. Energy Information Administration. *International Energy Outlook 2016*; Conti, J., Ed.; EIA, 2016; Vol. 0484(2016).

(2) World Energy Council. *World Energy Resources: 2013 Survey*; 2013.

(3) The Keeling Curve https://scripps.ucsd.edu/programs/keelingcurve/ (accessed Dec 21, 2016).

(4) Walsh, J.; Wuebbles, D. *2014 National Climate Assessment*; 2014.

(5) ExxonMobil. *2013 The Outlook for Energy: A View to 2040*; 2012.

(6) Roser, M.; Ortiz-Ospina, E. World Population Growth https://ourworldindata.org/world-population-growth/ (accessed Dec 21, 2016).

(7) Climate at a Glance: Global Time Series http://www.ncdc.noaa.gov/cag/ (accessed Dec 21, 2016).

(8) Munsell, M. GTM Research: Global Solar PV Installations Grew 34% in 2015 https://www.greentechmedia.com/articles/read/gtm-research-global-solar-pv-installations-grew-34-in-2015.

(9) Sun, K.; Shen, S.; Liang, Y.; Burrows, P. E.; Mao, S. S.; Wang, D. *Chem. Rev.* **2014**.

CHAPTER 2

Semiconductors and Metals for Photocatalysis

2.1 Summary

The concepts involved in photocatalysis are presented in this chapter. This dissertation investigates the photocatalytic production of hydrogen through the splitting of water and specifically focuses on the performance of silicon-based photocathodes for performing the hydrogen evolution reaction. The interaction of metal nanoparticles with the silicon system and their effects as co-catalysts and optically active materials are explained in detail. The processes that lead to inefficiencies and the interactions of semiconductors and other materials are discussed.

2.2 Background

2.2.1 Semiconductors

In the most general sense, semiconductors (SC) are materials that have electric conductivities intermediate to metals and insulators. The conductivity of a material is dependent on the ability of valence electrons to be excited to higher energy states and can be characterized by its electronic band structure. In metals, the valence band (VB), which is the highest energy band that is occupied by electrons at absolute zero temperature, is partially filled. At room temperature, electrons are easily excited to higher energies within the VB, resulting in high conductivity. In SCs and insulators, the VB is completely filled at 0 K and the next available energy band above the VB is known as the conduction band

(CB). There is a gap in energy between these two bands where no states exist that is known as the band gap. In an insulator, the band gap is so large that the excitation of an electron from the VB to CB is very improbable at room temperature, resulting in very low conductivity. In a SC, the band gap is smaller, making the thermal excitation of electrons to the CB at room temperature more probable. In the field of photocatalysis, photons that have energies larger than this band gap are used to excite electrons in a SC. This excitation causes the VB to have holes, which is the lack of an electron. When this occurs, the electrons in the CB have an elevated potential to drive reduction reactions, and the holes in the VB have the potential to drive oxidation reactions.

SCs for device applications are typically doped with impurity atoms, which changes the equilibrium concentrations of electrons and holes. If a SC is doped with atoms that have more valence electrons than the SC atoms, the dopant donates extra electrons to the SC, making the SC n-type. If the dopant atom has fewer valence electrons than the SC atoms, the dopant is an electron acceptor and the SC is p-type. In a p-type SC at equilibrium, there are far more holes than electrons, which makes holes the majority charge carrier. The opposite is true for n-type.

2.2.2 Photocatalytic Water Splitting

The goal of water splitting is to convert water into hydrogen and oxygen gases. This is accomplished through the combination of two half reactions: the hydrogen and oxygen evolution reactions (HER and OER). The HER, OER, and the net water splitting reaction are shown in Equations 2.1, 2.2, and 2.3, respectively, for acidic conditions.

2.1 $$4\mathrm{H}^+ + 4e^- \rightarrow 2\mathrm{H}_2$$

2.2 $$2\mathrm{H}_2\mathrm{O} + 4\mathrm{h}^+ \rightarrow 4\mathrm{H}^+ + \mathrm{O}_2$$

2.3 $$2H_2O + 4e^- + 4h^+ \rightarrow 2H_2 + O_2$$

For the HER, protons are reduced by electrons to form hydrogen. This reaction has an equilibrium potential of 0 V vs. the reversible hydrogen electrode (RHE). For the OER, water is oxidized by holes, or the lack of an electron in a valence state, to produce protons and oxygen. OER has an equilibrium potential of 1.23 V vs. RHE. Together, this means that the net water splitting process requires a thermodynamic minimum potential of 1.23 V to occur.

In an ideal water splitting photocatalyst (depicted in Figure 2.1), photons are absorbed by the semiconductor particle to generate the energetic electrons and holes required to drive the HER and OER. However, there are certain conditions that must be met for this to be possible. The first is that the VB of the SC must have a more positive potential than the OER equilibrium potential. Similarly, the CB must have a more negative potential than the HER equilibrium potential. This essentially requires the charge carriers to have enough energy to drive the reactions. This also means that the band gap of the SC must be at least 1.23 eV. Therefore, the incoming photons must have at least that energy, which corresponds to a wavelength of light shorter than 1010 nm. Figure 2.2 illustrates these points. In CdSe and TiO_2, the bands are positioned appropriately and, therefore, satisfy the thermodynamic requirements as a single-particle is less positive than the OER potential.

There are other requirements for these systems to work in addition to the thermodynamics. The excited charge carriers must also: (1) be able to travel to the surface of the particle and (2) have enough energy to overcome the potential barriers of the half-

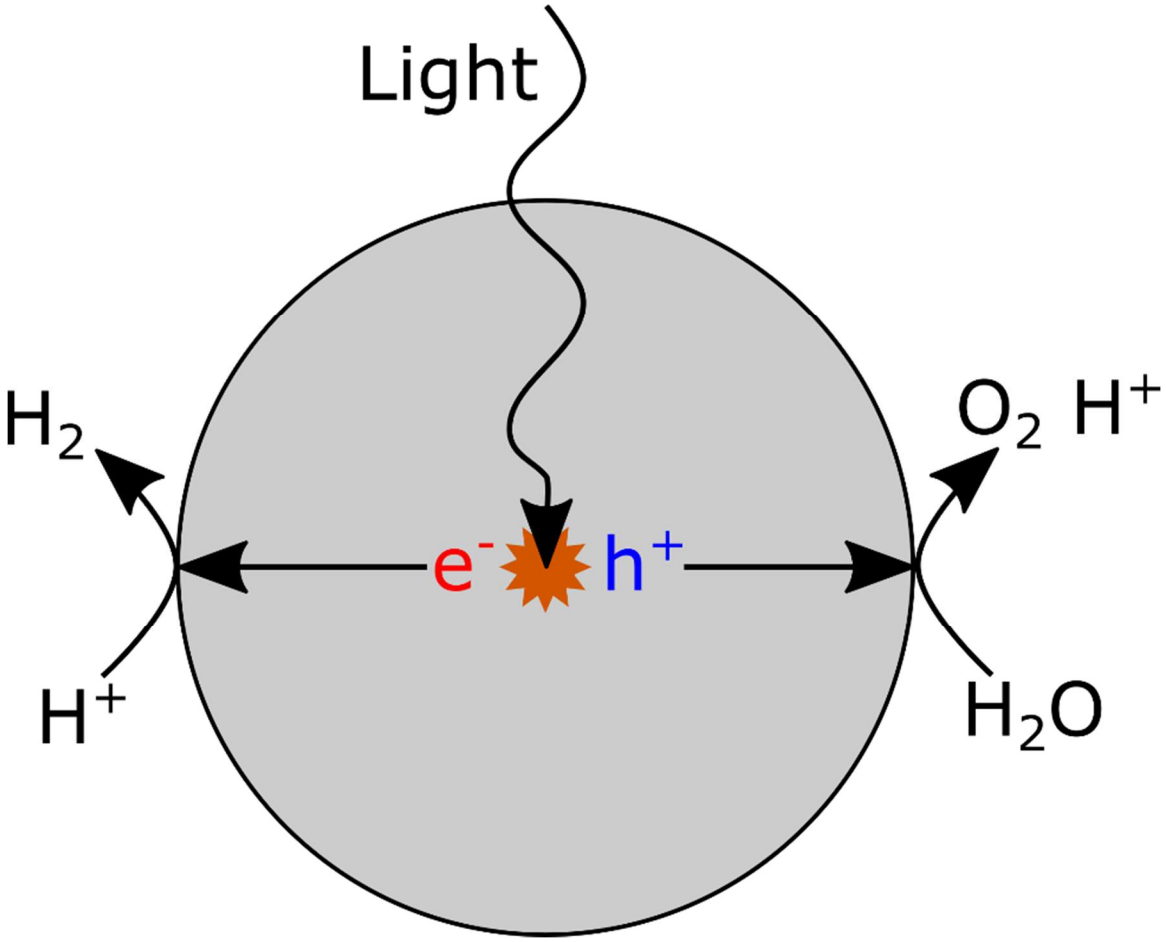

Figure 2.1: Schematic of an idealized photocatalyst. A photon is absorbed in the particle, forming electrons and holes. The electrons drive the HER and the holes drive the OER. This particle is not drawn to scale, but it would realistically have a diameter that is smaller than the wavelengths of incoming light.

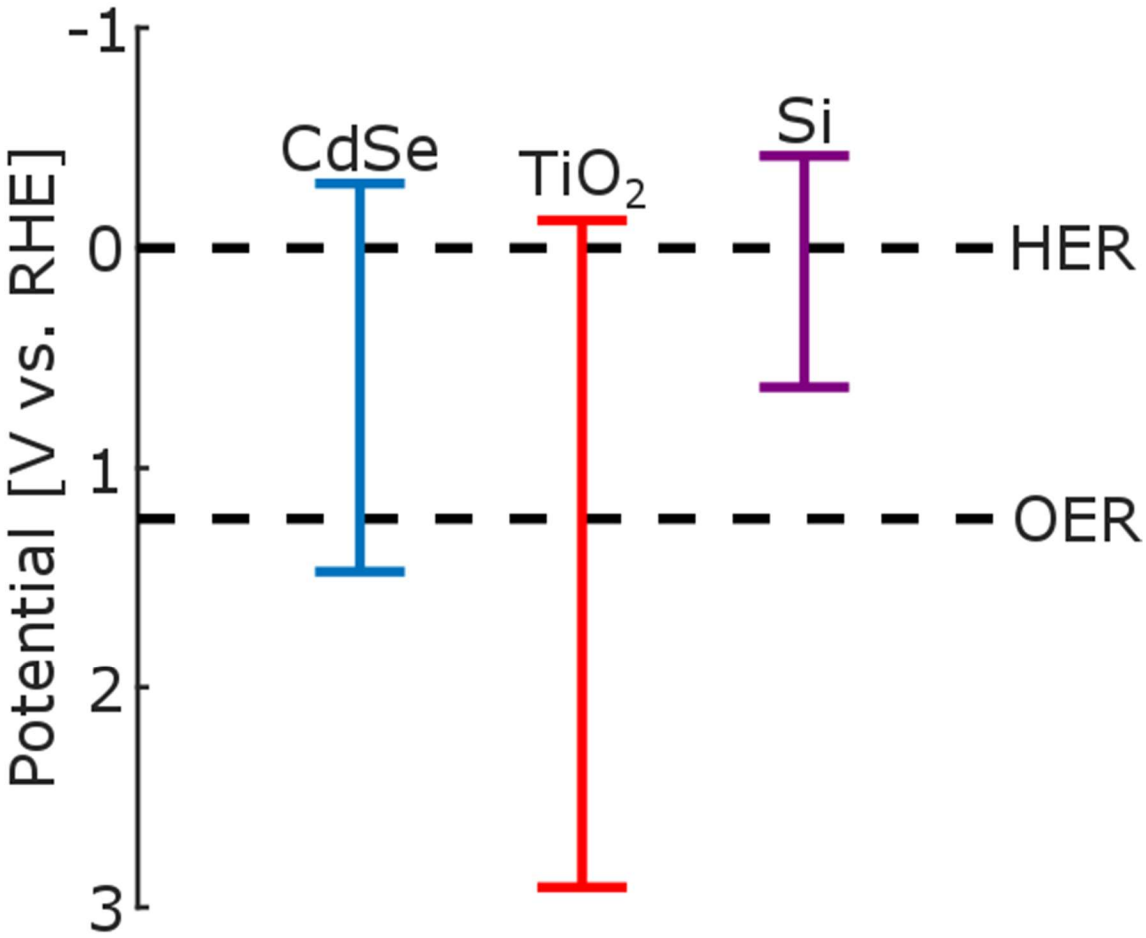

Figure 2.2: Band positions of three different semiconductors relative to the equilibrium potentials of the HER and OER.[1,2] The VB edges are located at the positive ends of the lines and the CB edges are at the negative ends of the lines.

reactions. This first requirement exists because these charge carriers remain excited for only a short time; when an electron and a hole interact with each other, the electron relaxes back to the VB. The net result is that the energy of the absorbed photon is converted to thermal energy that heats the material can also emit a photon of lower energy. The rate of recombination strongly depends on the type of SC and there are different mechanisms for recombination to occur. The second requirement exists because there are activation barriers that must be overcome to drive these electrochemical reactions, just as for thermochemical reactions. For these reasons, none of the SCs in Figure 2.2 can perform water splitting with only light as the energy input.

2.2.3 Limitations and Sources of Inefficiency

The CdSe and TiO_2 band positions (Figure 2.2) are favorable from a thermodynamic perspective, but are unable to split water due to losses related to the lifetime and energy of the charge carriers and inefficiency in the conversion of photons into charge carriers. These problems hinder all photocatalytic processes. The following subsections will discuss each of these issues.

2.2.4 Bulk Recombination

The loss of charge carriers through recombination is a major source of inefficiency in photocatalytic systems. The rate of recombination greatly depends on the SC properties and can occur in the bulk of the SC through radiative, trap-assisted, and Auger mechanisms.[3] Radiative recombination occurs when a CB electron directly relaxes back to the VB and emits a photon with an energy similar to the band gap. Trap-assisted recombination is caused by the existence of impurities that cause defect states at energies near the middle of the gap. This can occur when an electron relaxes to this defect state

and a hole increases its energy to meet it at the defect level (or vice-versa). Auger recombination occurs when a CB electron accepts the energy released by a separate electron-hole recombination and later dissipates the extra energy as heat.

Figure 2.3 shows the band structures of two classes of semiconductors. The difference between these two classes is whether or not the VB maximum lines up with the CB minimum in momentum space. Direct band gap SCs require no change in momentum space for a transition to occur. Indirect band gap SCs, in contrast, require an interaction with phonons to change momentum and facilitate transitions. These differences dictate the dominant recombination mechanism for a particular semiconductor. For a direct band gap SC, radiative recombination is highly probable, but very unlikely for indirect SCs. Trap-assisted recombination is the dominant mechanism in indirect band gap SCs. Since Auger recombination depends on multiple carriers interacting, it is not typically a dominant recombination route except in very highly doped semiconductors or when the charge carrier generation rate is very high. The relative effects of these recombination pathways can be described by the lifetime of a charge carrier (hole or electron) when confronted with these different mechanisms. The overall lifetime (τ_{bulk}) can be quantified with Equation 2.4.

2.4 $$1/\tau_{bulk} = 1/\tau_{direct} + 1/\tau_{Auger} + 1/\tau_{trap}$$

This overall lifetime can then be converted to a diffusion length (r) via Equation 2.5, where *D* is the diffusion coefficient for a given charge carrier (hole or electron) in a particular material.

2.5 $$r = \sqrt{D\tau_{bulk}}$$

For an indirect band gap SC like p-type Si, the minority charge carrier (electron) diffusion

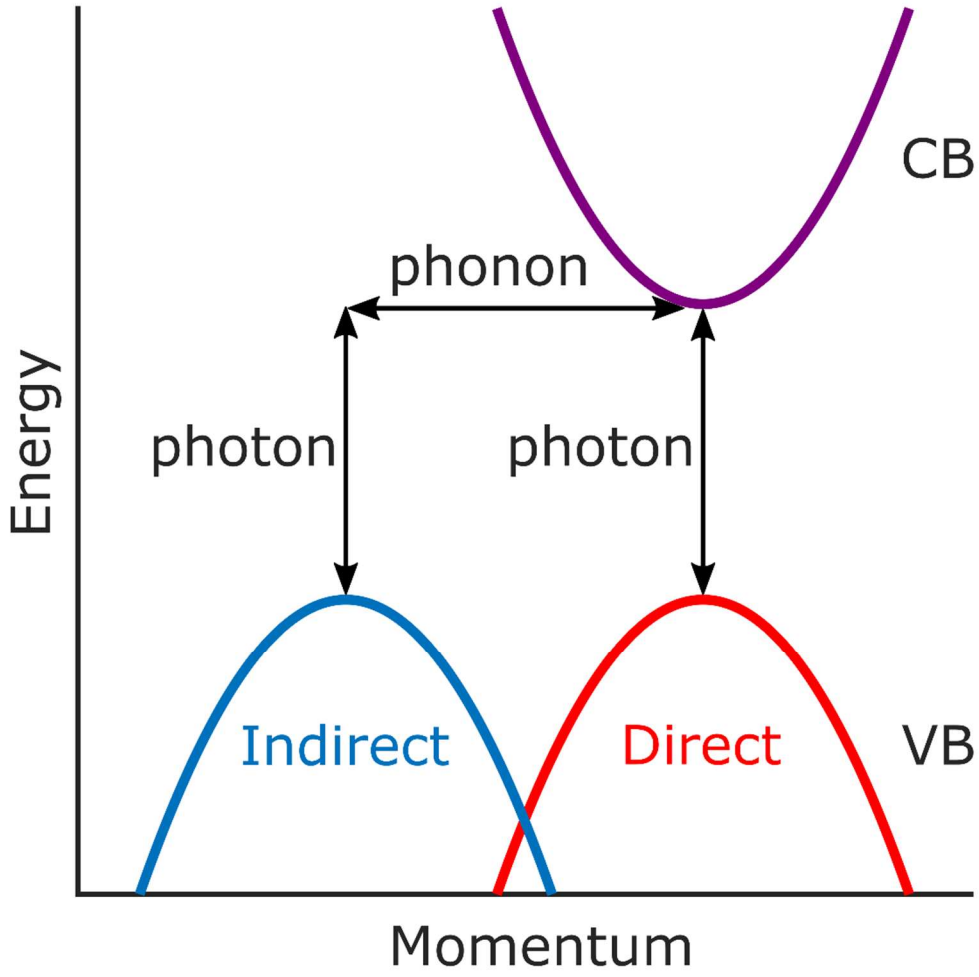

Figure 2.3: Band diagrams for direct and indirect semiconductors. The band gaps of both SCs are equal, but the indirect band gap SC requires an additional phonon transition to experience charge excitation or recombination.

length is between 100 and 400 μm for typical dopant concentration ranges.[3] TiO_2, which has different phases that can coexist (e.g. anatase and rutile) and have different types of band gaps, generally has a much shorter minority charge carrier (hole) diffusion length than Si. The diffusion length is typically cited between 10 nm and 10 μm,[4,5] and this uncertainty comes from the multi-phase and particle size effects associated with TiO_2.

2.2.5 Photon Absorption by Semiconductors

The absorption of photons is clearly a requirement for performing photocatalytic reactions. The ability to absorb light is dictated by the dielectric function (complex permittivity) of a material (ε), which is directly related to the complex refractive index ($\underline{n}$) through Equation 2.6. The real component of the dielectric function (ε_1) dictates the polarizability of the material and the imaginary component (ε_2) dictates the how energy is dissipated in the material.[6] The real component of the complex refractive index is the refractive index (n) and specifies how light is refracted once it enters a material. The imaginary component ($\varkappa$) is the extinction coefficient, which describes how light is attenuated (absorbed) in a material. These properties are wavelength (λ) dependent.

2.6
$$\epsilon(\lambda) = \epsilon_1(\lambda) + i\epsilon_2(\lambda) = \underline{n}(\lambda)^2 = \big(n(\lambda) + i\kappa(\lambda)\big)^2$$
$$\epsilon_1 = n^2 - \kappa^2 \text{ and } \epsilon_2 = 2n\kappa$$

The absorption of light in a material at a specific location is proportional to the product of the electric field intensity at that location and the ε_2 of the material. However, before light can be absorbed in a material, it must first enter the material. The reflection of photons from the material's surface is the physical process that prevents the light from entering the material. The Fresnel equation can be used to calculate the reflectivity of a material (*R*), which depends on its refractive index and extinction coefficient (n_2 and $\varkappa_2$),

the refractive index of the material containing the incident light (n_1), and the angle of illumination (θ_i). Equation 2.7 shows a special form of this equation for normal incidence ($\theta_i = 0°$)

2.7 $$R = [(n_2 - n_1)^2 + \kappa_2^2]/[(n_2 + n_1)^2 + \kappa_2^2]$$

In this dissertation, the material surrounding the absorbing material is either air ($n_1 = 1$) or water ($n_1 = 1.33$). The reflectance values plotted in the top of Figure 2.4 are based on this equation. For Si, there is greater than 30% reflectance of light over the entire 300 to 800 nm range. The consequence of this is that a large fraction of incident photons do not have the opportunity to be absorbed. The reflectance is much lower for GaN because the difference between its refractive index and air's is smaller than for Si.

The light that is not reflected has an opportunity to be absorbed based on the material's absorption coefficient (α), described in Equation 2.8.

2.8 $$\alpha(\lambda) = 4\pi\kappa(\lambda)/\lambda$$

If the absorption coefficient at a given wavelength is large, it is a good absorber of light at that wavelength. Otherwise, the light can pass through the material, which is transmission. The bottom of Figure 2.4 shows the absorption coefficients for Si and α-GaN. The band gaps of Si and α-GaN are 1.12 eV and 3.4 eV, respectively. Based on these band gaps, they should be able to absorb light up to 1107 nm and 365 nm, respectively. In the figure, the threshold of absorption for α-GaN is about 360 nm, which is in good agreement with the band gap. For Si, the same type of threshold appears to be at 400 nm. The main difference between these two SCs is that α-GaN has a direct band gap and Si has an indirect gap. As mentioned in the bulk recombination discussion (Subsection 2.2.4), the probability of a transition is hindered by the required change in momentum space for an indirect SC. As a

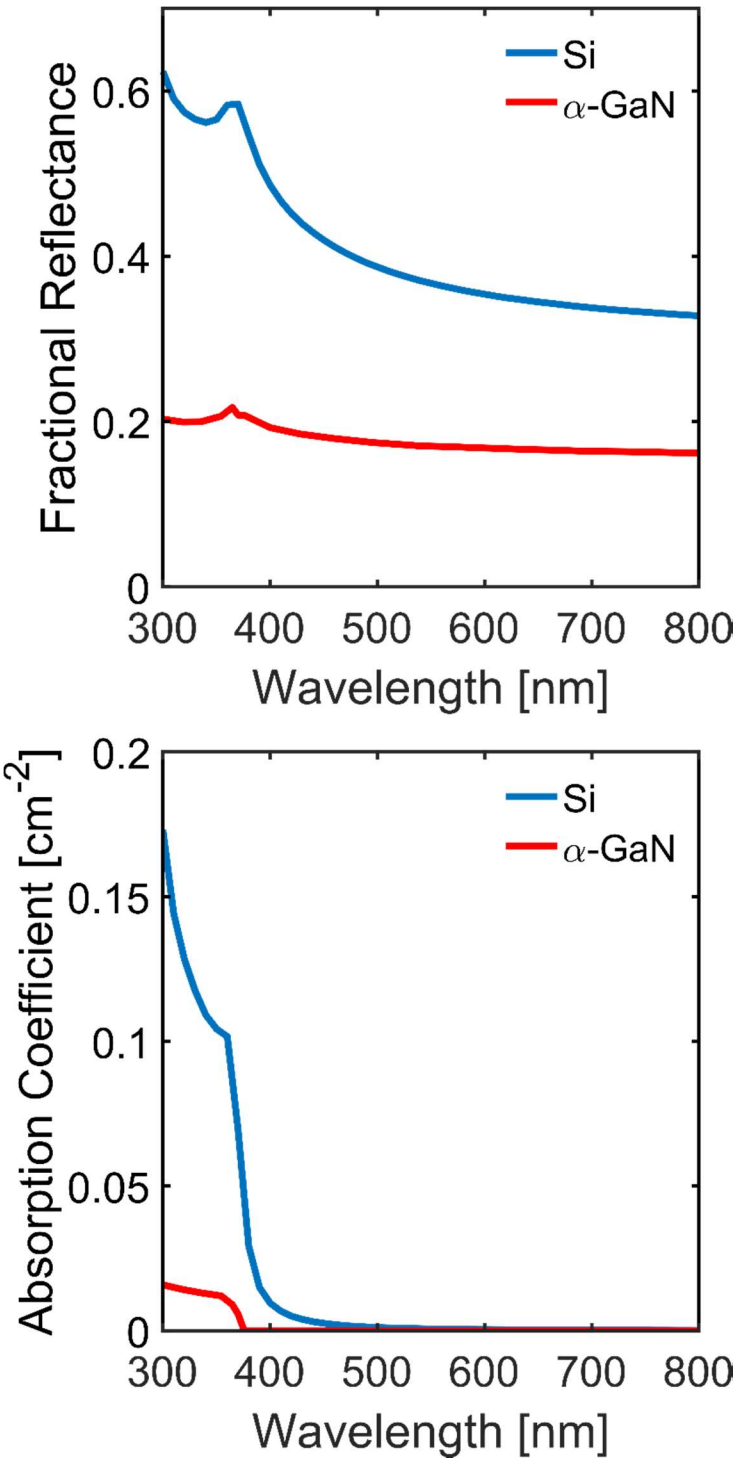

Figure 2.4: Semiconductor optical properties (Top) Fractional reflectance of Si and α-GaN calculated at normal incidence. (Bottom) Measured absorption coefficients for Si and α-GaN.[8,9]

result, Si must be thick to absorb the wavelengths between 400 and 1107 nm.

Another source of loss in these systems occurs when an electron is excited by a photon that has an energy that is significantly larger than the band gap energy. Initially, the electron exists at an energy above the CB that is equal to the difference between the photon energy and band gap energy. Almost instantaneously, the electron relaxes down the CB, dissipating the extra energy as heat. In the case of Si, half of the energy from a 2.24 eV (553 nm) photon is immediately lost through this mechanism. In the solar cell community, this loss results in the concept known as the Shockley-Queisser limit, which states that a single junction silicon solar cell can, at most, achieve a 32% solar conversion efficiency.[7]

2.2.6 Reaction Rates

Once the charge carriers arrive at the reactive surface of the photocatalyst particle, they must have enough energy to overcome the activation barrier for the reaction. This concept is defined in electrochemistry as overpotential. Overpotential is the amount of potential needed in excess of the equilibrium potential to drive an electrochemical reaction at a certain rate. To explain how serious this problem is for the water splitting half reactions, it is helpful to consider a hypothetical electrolyzer that uses the most active HER and OER electrocatalysts, Pt and RuO_2, respectively. For the HER, Pt can achieve a rate of 0.1 mA/cm^2 at an overpotential of 0.067 V. For the OER, RuO_2 requires 0.24 V of overpotential to achieve the same rate.[2] In this near-ideal case, 0.31 V of overpotential, or 1.54 V total, must be applied across the Pt and RuO_2 electrodes to achieve a water splitting current of 0.1 mA/cm^2, which produces only 1.9 μmol of H_2 per hour per cm^2.

The SCs that have been routinely studied as photocatalysts the HER and the OER (e.g., Si, TiO_2, Fe_2O_3, $BiVO_4$, etc.)[2,10–13] have surfaces that are unable to match the

aforementioned inherent rates as photocatalyst materials. For example, at a given potential, Si can only achieve a hydrogen production rate that is about 1 million times slower than Pt, based on the differences in their exchange currents (explained in Chapter 4.). As a result, co-catalysts must be added to these SC photocatalyst particles to achieve reasonable reaction rates. In this dissertation, these co-catalysts are metals, but they can also be metal oxides, hydroxides, and sulfides[12] and exist in various forms like films, particles, and molecular clusters.

2.3 Photoelectrochemistry

As discussed in the previous section, there are many sources of loss in photocatalytic devices that prevent them from being practical. These interacting processes make this a complex system, so it is important to break the problem down into smaller parts. For example, it is important to develop more active OER catalysts because even the best existing catalysts require high overpotentials. Others are trying to improve the light harvesting efficiency of these devices. These aspects of the photocatalyst cannot be adequately investigated without removing the effects of the other sources of loss. Photoelectrochemistry is used to gain fundamental insights about these individual mechanisms.

2.3.1 Fujishima and Honda (Two-Electrode)

The founder of this field is generally considered to be A. E. Becquerel, whom discovered the photovoltaic effect in 1839,[14] but Fujishima and Honda are responsible for demonstrating the potential value of the field.[15] In 1972 they published their work using a two electrode cell where TiO_2 was the photoanode and Pt as the cathode. In this work,

they applied a potential across the two electrodes and saw a significant increase in the resulting current when UV light was shined onto the TiO_2.

This method represents a way to separate a complete photocatalytic water splitting particle into a device where the HER and OER half reactions are performed on separate surfaces. The added control over the energy of the charge carriers through varying the applied potential across the electrodes enhances the ability to identify which loss mechanisms are dominant. Unfortunately, in this two electrode approach, the losses associated the resistance of the electrolyte between the two electrodes and the inefficiencies of the Pt cathode are combined with the losses associated with the photoanode. The next subsection discusses the use of a three-electrode cell to remove these added effects.

2.3.2 Three-Electrode Photoelectrochemical Cell

In a three-electrode cell, there is an additional electrode used called a reference electrode and the potential is applied by a potentiostat instead of a simple DC power supply. This reference electrode is ideally unchanged by the operating conditions of the measurements and serves as a means of identifying the potential applied to only the working electrode and ignore the overpotential losses associated with the electrode performing the other half reaction (counter electrode). Simultaneously, the potentiostat measures the current that passes from the working to counter electrode. This system is also able to compensate for losses due to the resistivity of the electrolyte. The specifics of these measurements for this dissertation are discussed in Chapter 3, but the main point here is that this is a good way to gain fundamental insights for the various mechanisms relevant to photocatalytic water splitting.

2.4 Properties of Metals

2.4.1 Catalytic Activity

A major reason for the inclusion of metal on the surface of a photoelectrochemical (PEC) electrode is to provide a reactive surface to drive the desired reaction with minimized overpotential. Pt is the most active metal surface for the HER, in part because of it its ability to bind hydrogen with an almost optimal free energy, not too strongly like Ni and not too weakly like Au.[16,17] Based on the metric of exchange current, which quantifies the rates of the forward and reverse reactions (HER and hydrogen oxidation) at equilibrium, Pt can support HER rates about 100 times faster than Ni and Au. Metal catalysts are often constructed as nanoparticles rather than films to achieve high surface areas when loaded onto a support material to provide a high number of reactive sites.

In addition to being able to drive reactions, a catalyst must survive the reaction conditions over a long time. This can be especially problematic in the acid and base electrolytes used for PEC. The thermodynamic stability of metals under these harsh conditions and at different potentials can be used to give an idea of how stable a catalyst material can be. This information is usually presented in Pourbaix (pH-potential) diagrams that are based on the reduction and oxidation reactions in which a metal can participate. Diagrams for some metals of interest are shown in Figure 2.5. Based on these diagrams, Pt should be stable under the conditions required for the HER (Potentials negative of 0.7 V vs. RHE and pH 0 to 2). In contrast, Ni cannot be used in these conditions at all, and Ag is potentially susceptible to dissolution. The specific aim of the work is this dissertation is not to make a better HER catalyst. Instead, good catalyst is used in this work to simply improve the onset potential of the reaction and to have a stable environment to be able to

gain fundamental insights about the other important processes involved with PEC. Pt is an obvious choice for this goal.

2.4.2 Optical Activity

Bulk metals are generally optically active, appearing shiny in visible light, which is a consequence of having free electrons, and they also absorb light through interband transitions (d-band to sp-band) just like semiconductors (VB to CB). On the nanoscale as very thin films or nanoparticles, metals can also experience intraband transitions that are caused by the free electrons and result in very frequent absorption and scattering events. The intraband transitions can occur when incident light has a frequency that matches the frequency at which free electrons oscillate about the nanoscale.

The dielectric functions of Ag, Au, and Pt are shown in the top left panel of Figure 2.6. These metals have very unique dielectric functions relative to each other and, consequently, have very different optical properties. The imaginary component of the dielectric function dictates the probability of interband transitions. Pt has a large imaginary component that increases significantly with wavelength. Au and Ag have similar imaginary components at low wavelengths, but become small at 600 nm (Au) and 350 nm (Ag). This means that Au and Ag will have interband transitions below 600 nm and 350 nm, respectively.

The effect of the shape of the real component of the dielectric function for the metal nanoparticle and the dielectric environment can be estimated using a quasi-static approximation when the particle radius is much smaller than the wavelength.[6,21] The scattering and absorption cross-sections of spherical particles can be calculated by Equations 2.9 and 2.10, respectively.

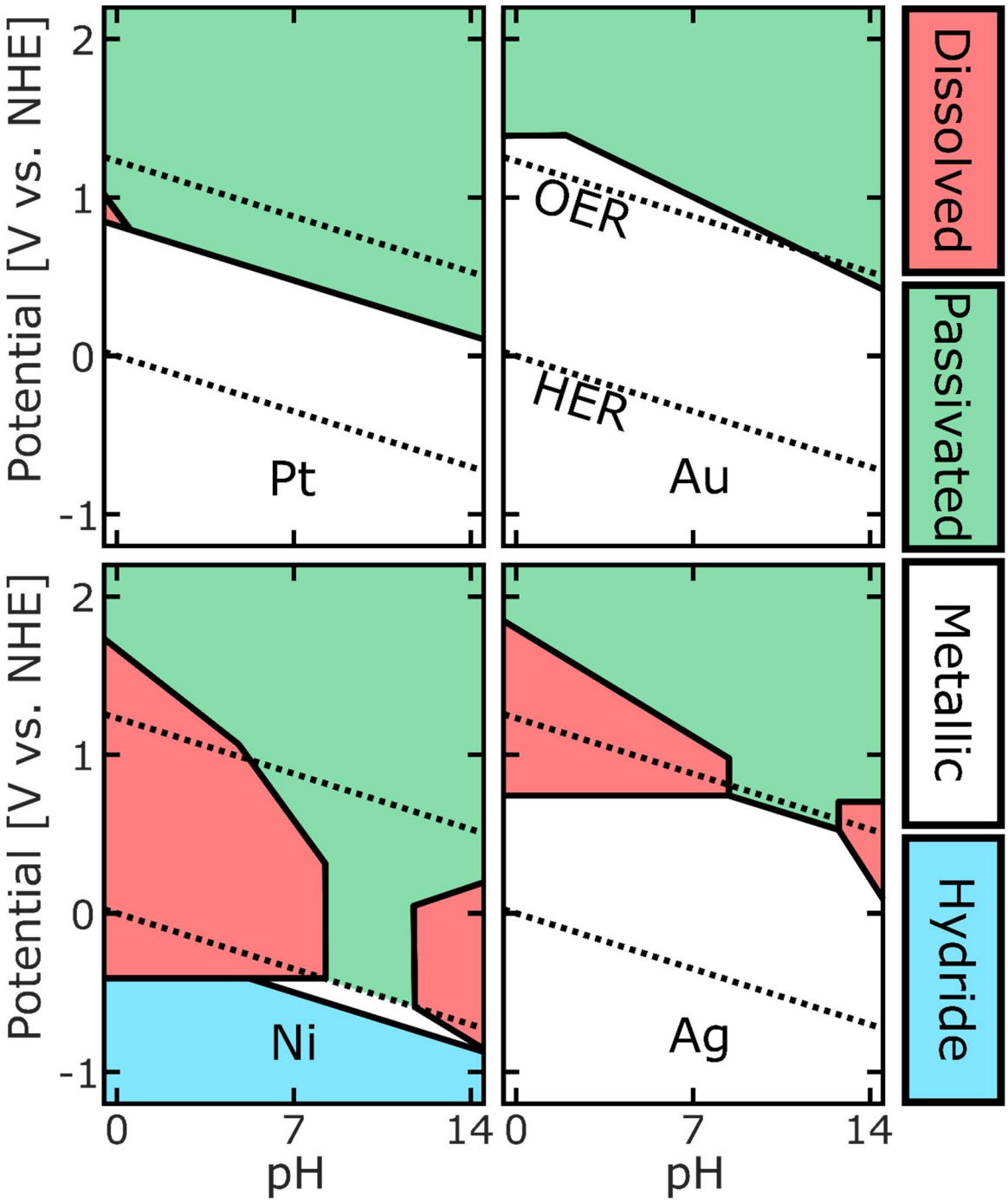

Figure 2.5: Pourbaix diagrams for Pt, Au, Ni, and Ag.[18–20]

2.9 $$C_s = \frac{8\pi}{3}\left(\frac{2\pi}{\lambda}\right)^4 r^6 \left|\frac{\varepsilon-\varepsilon_m}{\varepsilon+2\varepsilon_m}\right|^2$$

2.10 $$C_a = \frac{8\pi^2}{\lambda} r^3 Im\left[\frac{\varepsilon-\varepsilon_m}{\varepsilon+2\varepsilon_m}\right]$$

In these equations, C_s is the scattering cross-section, C_a is the absorption cross-section, *r* is the particle radius, λ is the wavelength, ε is the complex dielectric function of the metal, and ε_m is the dielectric constant for the non-absorbing environment. Additionally, the occurrence of LSPR at a given wavelength can be determined through the Fröhlich condition shown in Equation 2.11, which says the real component of the metal dielectric function must be equal to twice the negative of the dielectric constant of the surrounding environment for resonance to occur. This approximation is only valid for a dipole resonance, as higher energy (quadrupole and octupole) resonances are not identified.

2.11 $$Re[\varepsilon(\lambda)] = -2\varepsilon_m$$

The Ag, Au, and Pt panels in Figure 2.6 show the calculated cross-sections for a 50 nm diameter sphere for each metal in different dielectric environments. For Ag in air, there is a large absorption peak and a slightly smaller scattering peak at 350 nm. In a dielectric of 4, the peak red-shifts to 470 nm and the ratio of absorption to scattering is nearly 1:1. The inset of the Ag panel shows that the Fröhlich condition is met at ≈ 350 and 470 nm for ε_m = 1 and 4, respectively. Therefore, the strong absorption and scattering by Ag is caused by LSPR. For Au, the scattering is weak and the absorption is broad and somewhat weak when the environment has a dielectric of one. In a dielectric of 4, the peaks red-shifts and grow much larger. The inset shows that LSPR should occur at 500 and almost 600 nm for the two environments, respectively. For Au in air, the interband absorption wavelengths overlap with the LSPR wavelength, which dampens the effect of the LSPR.

In the higher dielectric, the LSPR is shifted to a non-overlapping wavelength, allowing the resonance to occur. The Pt panel shows a minimal LSPR effect. For Pt, interband transitions can occur at all wavelengths between 200 and 800 nm, which prevents intense LSPR in the visible range. A small LSPR effect can be observed at the UV wavelengths.

An example of the effects of particle size and shape can be seen in the top left panel of Figure 2.7. These extinction data were collected experimentally from solutions of colloidal Ag nanoparticles using UV-Vis spectroscopy (Chapter 3). In this figure, the Ag nanospheres (~40 nm diameter) shows a single resonance peak near 420 nm. The two cube samples show a large peak (dipole) and small, higher-energy peaks due to higher order (quadrupole and octupole) resonances. As the side length of the cube is increased from ~80 nm to ~130 nm, the peak resonance wavelength shifts from 470 nm to 525 nm. This occurs because the oscillation frequency of the free electrons decreases as the particle size increases.

The top right panel of Figure 2.7 shows a computational result from COMSOL that shows the electric field enhancement profile in the same plane as the incoming electric field oscillations around an 80 nm Ag nanosphere in air at its LSPR wavelength (382 nm). COMSOL solves Maxwell's equations for a specified incident light intensity and wavelength over a system with specific optical properties using a finite element mesh method. At regions very near the Ag surface, the field intensity ($|E|^2$) is enhanced relative to the background field intensity ($|E_0|^2$) by about 2 orders of magnitude. At distances just 20 nm away from the surface, the enhancement is only by a factor of 10. In general, at 60 nm from the particle surface, there is almost no enhancement of the electric field. Additionally, at the region directly beneath the particle, there is a patch of very low electric

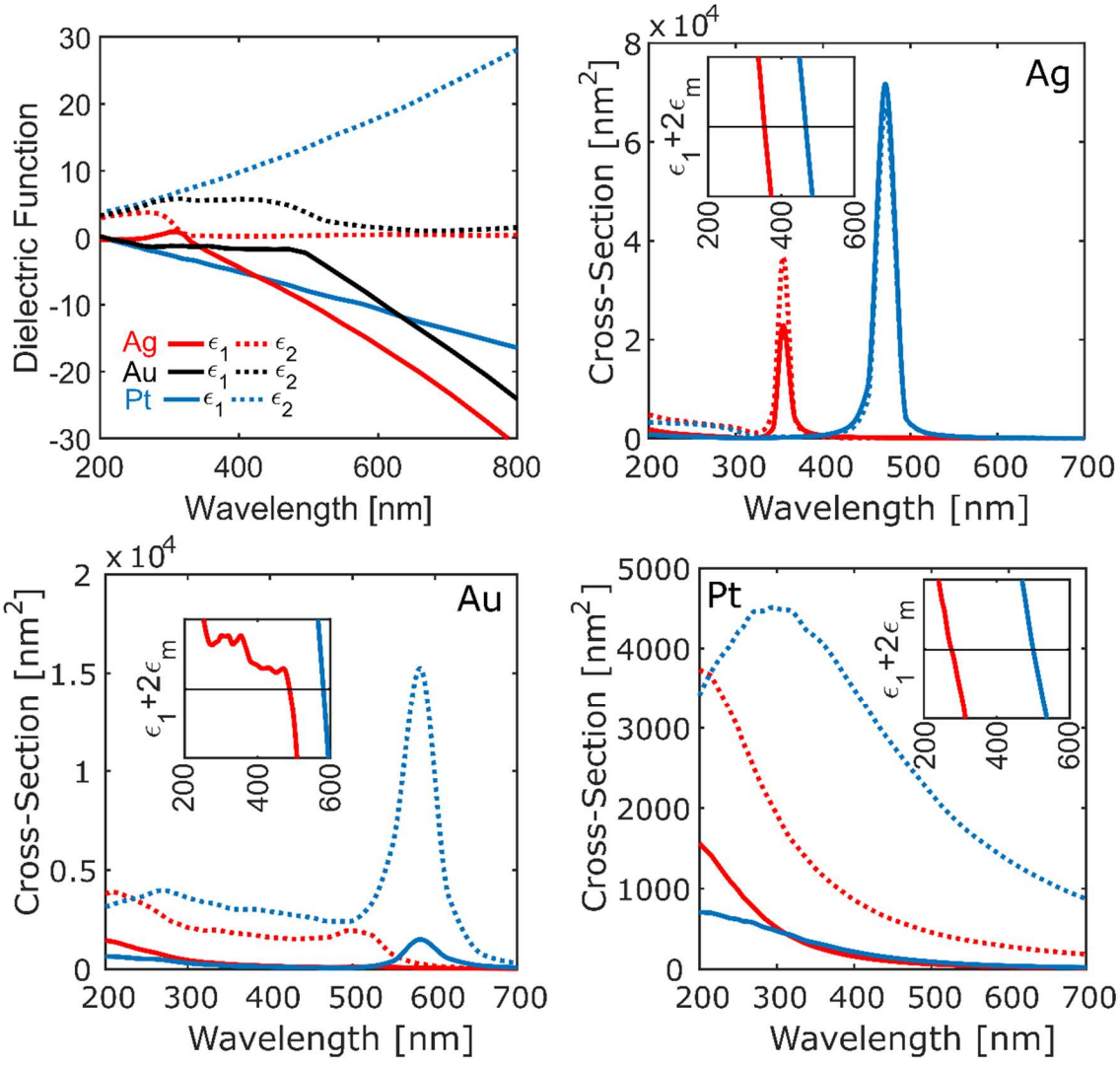

Figure 2.6: Optical properties of metals (Top Left) The real (ε_1) and imaginary (ε_2) components of the dielectric functions of Ag, Au, and Pt. (Ag, Au, and Pt plots) Absorption and scattering cross-sections for 50 nm diameter nanospheres calculated using the quasi-static approximation. Scattering is shown as solid curves and absorption is shown as dashed curves. The red plots are for a surrounding dielectric constant of 1 (air) and the blue plots have a surrounding dielectric constant of 4. (Insets) Plots identifying the wavelengths at which the Fröhlich condition ($\varepsilon_1 + 2\varepsilon_m = 0$) is met based on the different environments ($\varepsilon_m = 1$ or 4). The condition is met where the plots cross the thin horizontal line, which corresponds to zero.

field intensity because the Ag is blocking the electromagnetic radiation from reaching that location. This electric field enhancement is clearly limited to the near-field.

2.4.3 Enhancement of SC absorption with LSPR

LSPR has found an application in the field of PEC as a means of improving the photocurrent generated by a SC. The bottom panel in Figure 2.7 depicts the strategy used by Ingram and Linic to increase the light-limited reaction rate of the OER on a nitrogen-doped titania (N-TiO_2) photoanode.[22] N-TiO_2 suffers from very short charge carrier diffusion lengths relative to the depth at which photons are absorbed. This causes recombination in the bulk of the SC to be a limiting factor in its efficiency. In their work, Ag nanocubes were mixed with N-TiO_2 particles and made into photoanodes. Two control electrode were used: bare N-TiO_2 and N-TiO_2 mixed with Au nanospheres. The enhancement of the light-limited photocurrent was determined to be due to the enhancement of the electric fields near the particle surface, which significantly hindered the bulk recombination process. The Ag nanocubes were able to generate these strong electric fields at wavelengths that the N-TiO_2 could absorb. The Au nanospheres could only generate strong electric fields at wavelengths that are above the absorption threshold for the N-TiO2, which resulted in no enhancement for the Au/N-TiO_2 system. A discussion of the suitability of this strategy for other SC PEC systems is presented in Chapter 4.

2.5 Interfaces and Charge Transport

The control of the energy of charge carriers through the potential applied to a PEC device is not without its own complexity. This section discusses the impact of forming interfaces with different materials while controlling the applied potential and their effects

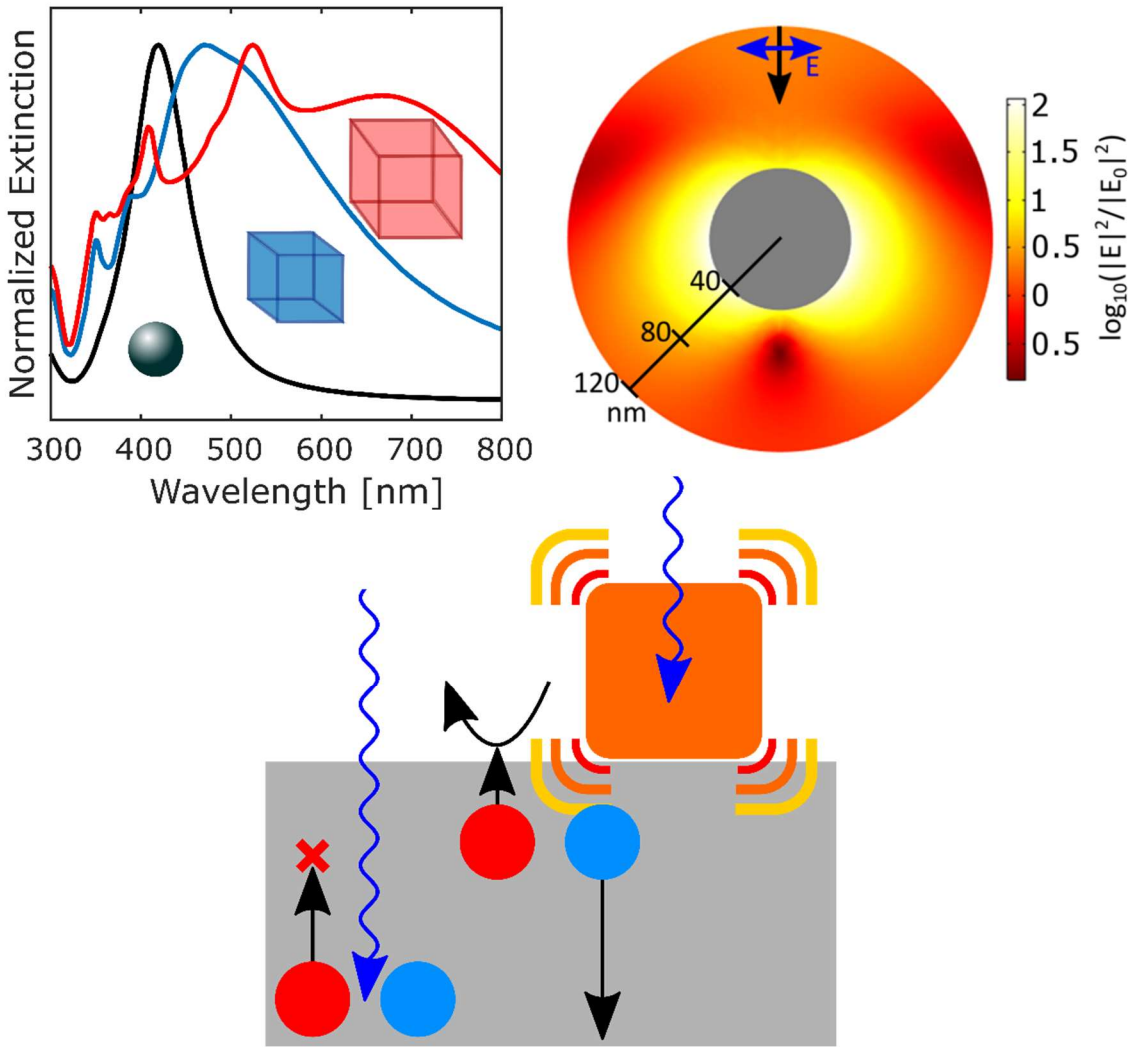

Figure 2.7: Optical properties and applications of plasmonic metal nanoparticles. (Top Left) Experimental normalized extinction (absorption + scattering) spectra for a solutions of 40 nm Ag nanospheres, 80 nm (side length) Ag nanocubes, and 130 nm Ag nanocubes.[23] (Top Right) Calculated (COMSOL) electric field intensity enhancement in the E-polarization plane for an 80 nm Ag nanosphere in air. (Bottom) Schematic describing the work by Ingram and Linic.[22] The LSPR from the Ag nanocube causes the excitation of charge carriers in N-TiO_2 to occur closer to the reactive surface to reduce recombination losses.

on the transport of charge within a SC electrode and across various boundaries. This discussion is framed exclusively from the perspective of p-type Si as the photoelectrode and is based on the assumption that the Schottky barrier model is applicable to this system by ignoring the effects of interfacial surface states. Si does tend to have a significant surface state effect, which controls the interface energetics instead of the materials located at the interface.[24,25]

2.5.1 Isolated Semiconductor

An isolated SC has a VB and CB that have constant energy throughout the entire SC. In between these bands is a Fermi level, which represents the electrochemical potential of the charge carriers in the SC. In an intrinsic (undoped) SC, the Fermi level is located near the mid-gap energy. This is because the number of electrons in the CB is equal to the number of holes in the VB of an intrinsic SC. For a p-type SC, there are more holes in the VB than electrons in the CB, making its Fermi level (E_F) closer to the VB energy. In general, the amount of doping dictates how close the Fermi level is to a given band energy. This system is depicted in Figure 2.8a.

2.5.2 Semiconductor/Electrolyte Interfaces

When the SC is put into contact with an electrolyte that contains a redox pair that exists at a specific equilibrium energy, charge carriers must move accordingly to re-establish equilibrium. In the case of p-type Si contacting an acid with dissolved H_2, the redox potential is 0 V vs. RHE and the CB and VB energies are roughly -0.45 and 0.67 V vs. RHE, respectively. In this kind of Si with an acceptor concentration of 10^{16} atoms/cm^3 due to boron doping, the Fermi level rests near 0.5 V vs. RHE (-0.17 V relative to the VB). Therefore, the Fermi level is at a positive potential relative to the electrolyte redox

potential. Figure 2.8b depicts this situation and shows that holes transfer to the electrolyte. In general, electrons tend to move in the direction of positive potential (decreasing energy) and holes move in the direction of negative potential (increasing energy). In this case the holes are the majority charge carrier and are responsible for equilibrating the electrochemical potential at the interface. This results in an upward bending of the VB and CB and the equilibration of the SC Fermi level to the electrolyte potential (Figure 2.8c).[1] The electric field that exists with this band bending pushes the electrons to the interface and the holes toward the bulk of the SC. Upon illumination, the number of CB electrons changes significantly, separating the Fermi level of the electrons (E_{FE}) from the hole Fermi level (E_{FH}) and pushing the system away from equilibrium (Figure 2.8d). These separate Fermi levels are called quasi-Fermi levels and are a result of separate equilibrium conditions existing in the VB and CB. The difference in potential between these two Fermi levels is called the photovoltage (E_{ph}) and is a result of the energy gained from the absorption of photons. A new steady-state is established in Figure 2.8e, with the electron quasi-Fermi level equilibrated with the electrolyte potential instead of the hole quasi-Fermi level, resulting in bands that have less upward band banding than in the dark.

The bent bands in this SC/electrolyte junction help separate charge carriers from each other near the interface. This region is called the space-charge layer, and at equilibrium, this band bending is dependent on the difference in energy (or potential) between the isolated SC Fermi level and the electrolyte potential. The band bending can

[1] In Si, a high density of surface states may exist at the Si/electrolyte interface, depending on the electrolyte. These states are due to dangling Si bonds that result from the termination of the Si crystal. In this situation, it is common for the surface states to control the interfacial band bending instead of the electrolyte. This concept is called Fermi level pinning and simply means that the barrier height is dependent on the energy of the surface states instead of the material with which the Si interfaces.

be increased by applying a negative potential to the back-side (away from the interface) of the SC, increasing the energy of the majority charge carriers. When this occurs, the rate of transfer of electrons to the electrolyte can increase, with this rate eventually being limited by the rate at which electrons can travel to the interface, which is dependent on the photon absorption and recombination rates.

For these devices to generate photocurrent, the electrons must cross the interface into the electrolyte and the holes must be swept away from the interface. The left part of Figure 2.9 shows potential routes for the charge carriers to take that do not result in currents that are useful for driving the HER. The recombination mechanisms that occur in the bulk of the SC, which were discussed in Subsection 2.2.4, occur away from the interface and are strongly dependent on the type of band gap (indirect vs. direct). This rate of bulk recombination is an inherent property of the SC and cannot be easily tuned. Recombination can occur at surface states, which are often defects that exist due to the termination of the SC surface, leaving dangling bonds. The rate of surface recombination can be reduced by passivating the surface.[26] In Si solar cells, this has been done by thermally growing an oxide on the surface or by coating it with SiN. Similar approaches for Si photoelectrodes have used TiO_2 films and methyl termination.[27,28] Recombination can also occur in the electrolyte when holes tunnel through or surmount the energy barrier formed by the bent VB and consume the electrons driven into the electrolyte from the CB. The rate of holes surmounting this barrier is directly related to the barrier height at the interface, which is defined as the difference in energy between the VB minimum and the electrolyte energy level. For a given SC, the amount of band bending at equilibrium depends directly on the barrier height.

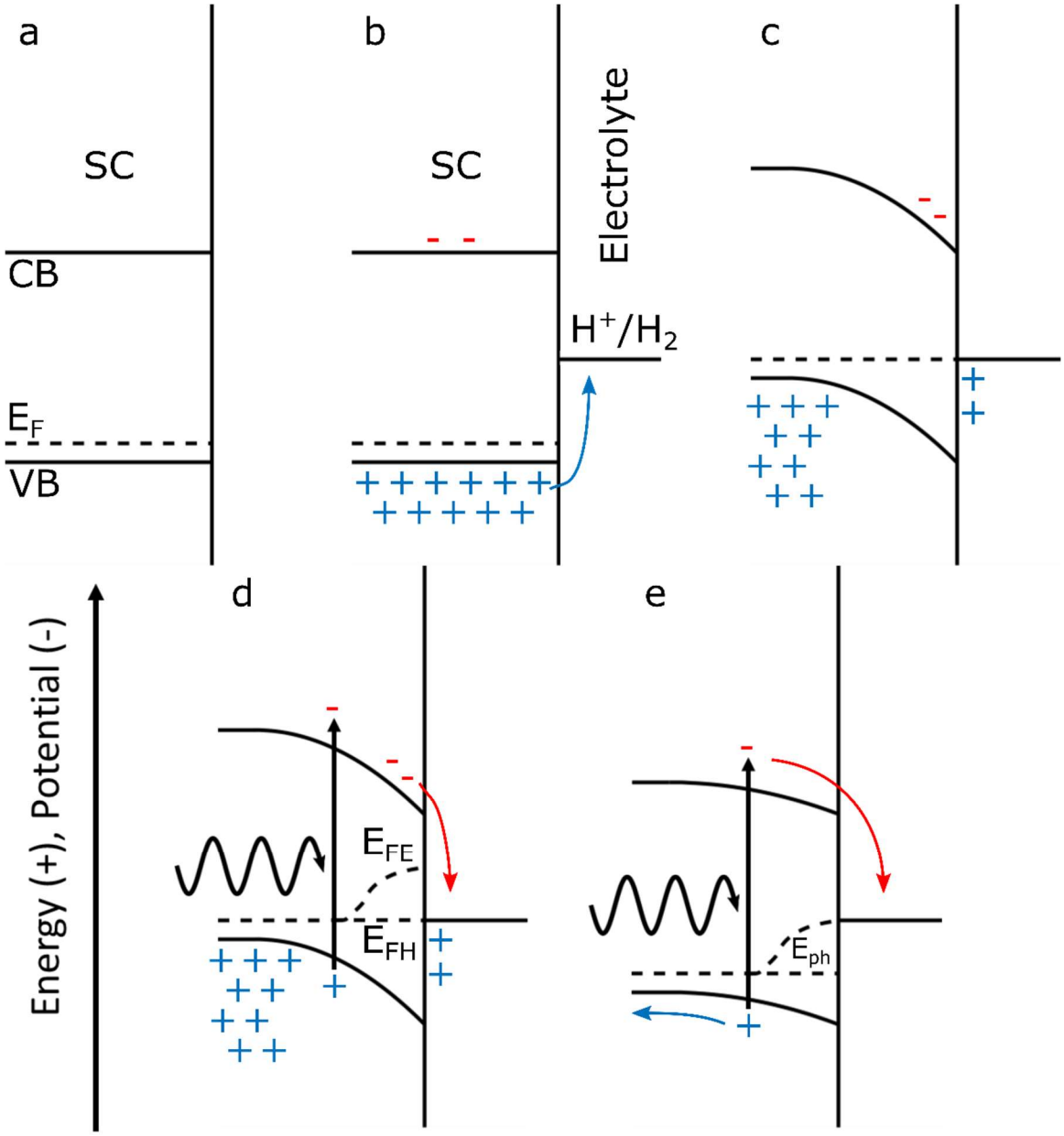

Figure 2.8: Band diagrams for a p-type SC. The lateral dimensions represent the distance from the SC surface. (a) Isolated SC. (b) SC in contact with an electrolyte at the HER redox potential before equilibrium in dark. (c) SC equilibrated with electrolyte in dark. (d) Illuminated SC with an increased electron (minority charge carrier) concentration out of equilibrium. (e) Illuminated SC at equilibrium with the electrolyte.

The amount of band bending is responsible for determining whether charge carriers recombine or are used to drive current. The amount of band bending can be altered by changing the potential of the majority charge carriers (holes). The right part of Figure 2.9 demonstrates this effect. When a negative potential is applied to a contact on the back of the SC, the change in the majority Fermi level shifts the bands upward. This results in increased band bending, which prohibits the flow of holes over the barrier. Additionally, the minority (electron) Fermi level is shifted above the potential of the solution, providing overpotential to possibly drive current. In photoelectrochemistry, the onset of current upon changing the potential of the majority charge carriers is useful for identifying how effectively charge carriers are used to drive reactions. At a high enough potential, the photocurrent (current in light less current in dark) becomes independent on the applied potential and is an indicator of the maximum rate at which charge carriers can be generated and traverse the interface.

2.5.3 Semiconductor/Metal Film Interfaces

The SC/metal film system is the origin of the term "Schottky Diode" and, assuming there are negligible surface state effects, has a barrier height that is equivalent to the SC/Electrolyte barrier height, with a slight difference. In the case of the metal film, its energy is defined by its work function, which is the amount of energy required to eject and electron from a solid surface to vacuum. The SC Fermi level equilibrates to this energy and forms a barrier. For isolated p-type Si in the dark, the CB energy is 4.05 eV below vacuum, which is equivalent to its electron affinity.[29] This means the VB energy is 5.17 eV below vacuum and the Fermi level is at 5 eV (based on the assumptions in Subsection 2.5.2). Therefore, for the SC/metal junction to have a barrier to the flow of holes into the

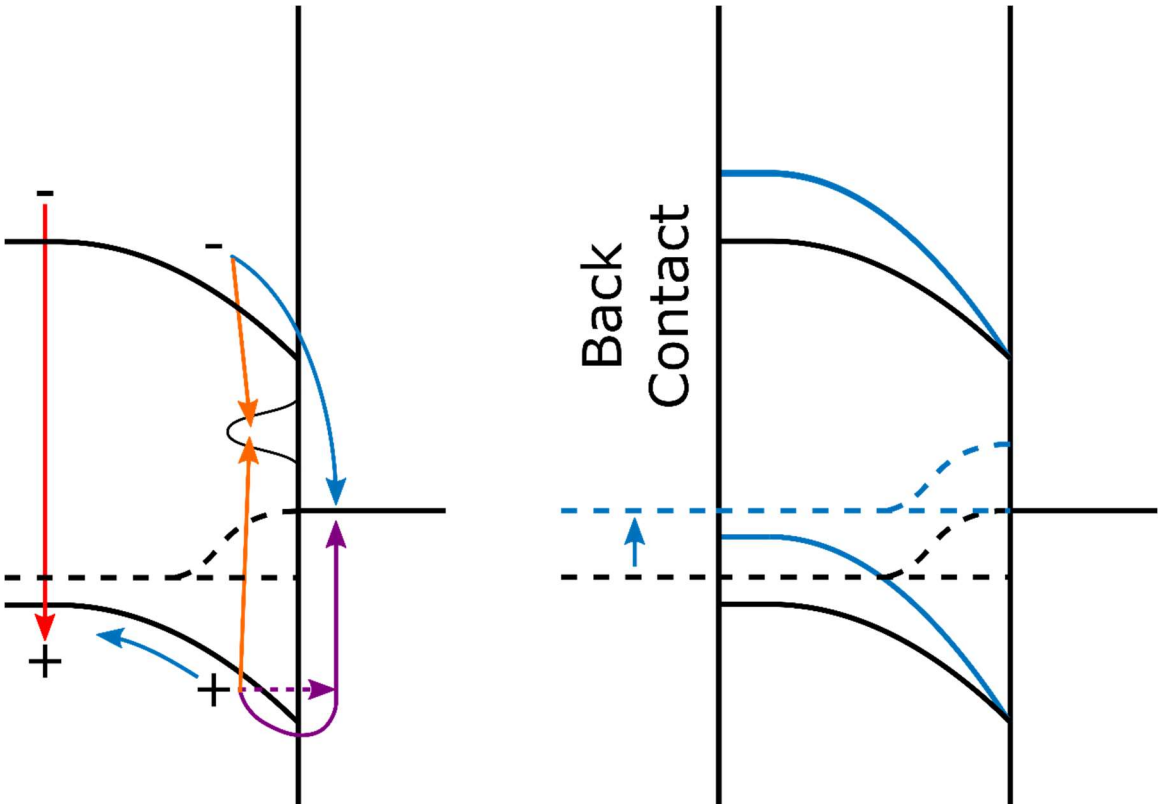

Figure 2.9: Paths for charge carriers in a semiconductor device and effect of controlling potential (Left) Possible routes for electrons and holes. The path that generates photocurrent is shown in blue. The bulk recombination processes are depicted in red. Surface-state induced recombination is shown in orange. The paths in purple result in recombination in the electrolyte. The solid purple line depicts thermionic emission of the hole over the barrier, and the dashed purple line represents the tunneling of holes through the barrier. (Right) The equilibrium band structure is shown in black. A negative potential can be applied at the back contact to raise the potential of the majority charge carriers and induce increased band bending to drive current.

metal, the work function of the metal must be less than 5 eV. If the metal has a work function greater than 5 eV, the holes have no barrier to flow into the metal. This is known as an ohmic contact. Pt is used frequently in this research and has a work function of 5.12 to 5.93 eV.[30] Pt films will form contacts to p-type Si that facilitate recombination. This is also true for Au (5.10-5.47 eV), but Ti (4.10-4.33 eV) and Ag (4.26-4.74 eV) form Schottky barriers with Si.[31] The barrier height of these Si/Pt interfaces can be improved by including a layer of Ti in between them.[32]

2.5.4 Semiconductor/Metal Nanoparticle Interfaces

In general, it is not efficient to use metal films to serve as catalysts for the HER. Since metals are highly reflective and absorb light efficiently, these films can significantly reduce the conversion of photons into charge carriers. For the OER, the use of films is often necessary to protect the SC surface from oxidation/dissolution. In addition to causing a loss of external quantum efficiency (EQE, rate of useful charge carrier generation divided by the rate of photon impingement), the use of high work function metal films, as described above, results in high recombination rates.

Using metal nanoparticles instead of films as a reactive surface can help alleviate this issue. In this situation, there is a mixed barrier because both SC/electrolyte and SC/metal interfaces exist. In the limit of a full metal film coverage, the barrier height is dictated by the SC/metal interface. In the limit of a full SC/electrolyte interface, the barrier height is dictated by the SC/liquid interface. In between these two limits, there is an effective barrier height that is between these two limiting cases and depends on the size of the metal contact area relative to the electrolyte contact area. The data shown in Figure 2.10 are from a calculation for the VB shapes based on different interface compositions.

The Si/electrolyte interface shows a barrier height of 0.67 V while the Si/Pt film interface has no barrier height. With the Pt nanoparticle interface, however, a small barrier height of 0.25 V is established. Since the VB potential in the bulk of the SC is -0.18 V, the actual potential that the VB holes must overcome is 0.49 V and 0.07 V for Si/electrolyte and Si/Pt + electrolyte, respectively. Clearly, when working with low barrier height or ohmic contacts, reducing the contact area can significantly improve the effective barrier height, reducing the rate of recombination. This is discussed in more detail in Chapter 6.

2.5.5 Semiconductor/Insulator/Metal Interfaces

Another strategy for reducing the movement of holes across the electrolyte is to put a thin insulating layer in between the SC and metal contact. This allows the build-up of charge at the interface and results in the tunneling of electrons through the insulator to the metal, while the undesired flow of holes in this direction is restricted. These layers also passivate the Si surface, significantly reducing the surface recombination rate.[32] This has been a well-documented approach for solar cells, but has recently found a use in photoelectrochemistry because it can be used to form a protection layer on SCs that were previously avoided due to stability issues in aqueous electrolytes.

2.5.6 Semiconductor/Semiconductor Interfaces

In general, when using Si and Pt to form a photoelectrode for the HER, the maximum barrier height that can be achieved is dependent on the electrolyte equilibrium potential, which is fixed at 0 V vs. RHE for this reaction. It is desirable to maximize the barrier height to reduce recombination rates. One way to do this is to make a buried junction in the SC, similar to the Si/metal film junction but use another SC instead of the metal film. In its simplest form, this means doping the top layer of the p-type Si with

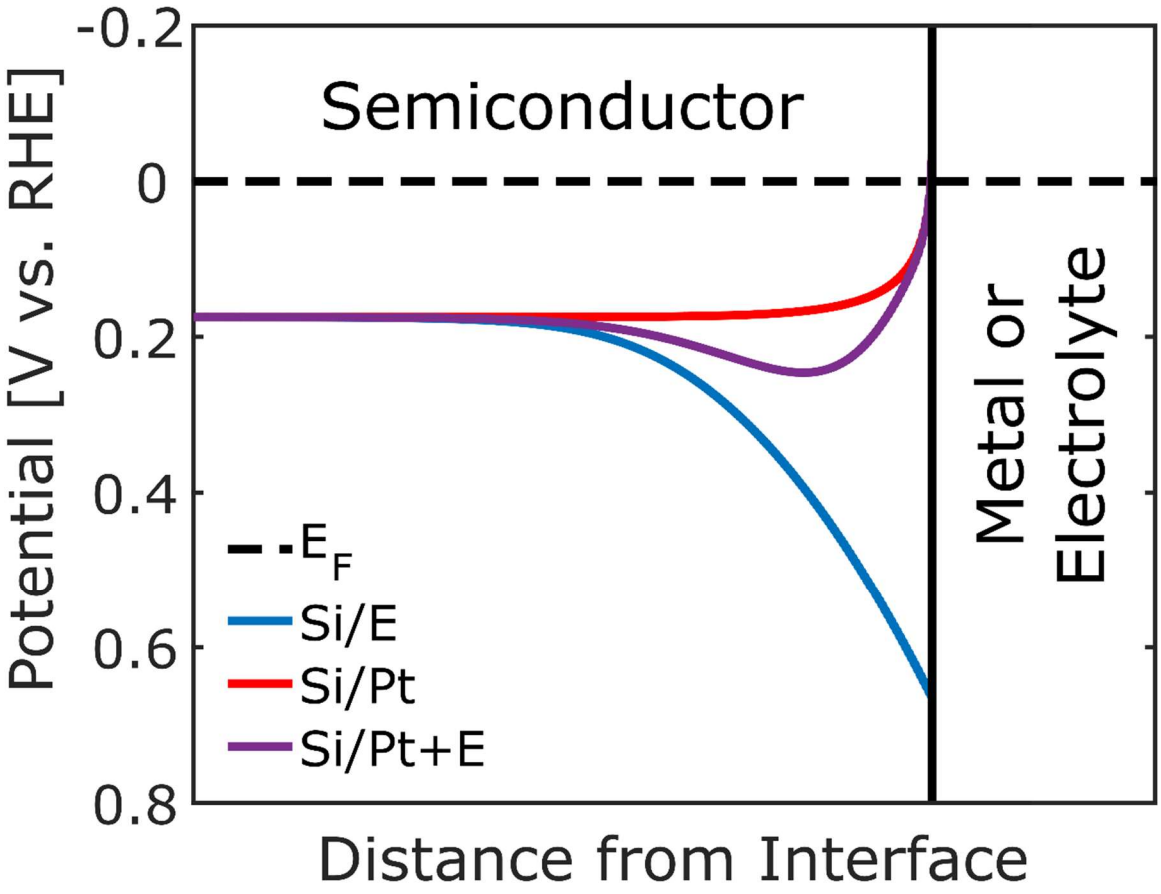

Figure 2.10: Effect of mixed (Si/metal/electrolyte) interfaces. The VBs for Si/Pt (film), Si/Electrolyte, and Si/Pt + Electrolyte interfaces are shown. The mixed interface has a 150 nm diameter Pt contact in the center of a 1200 nm diameter Si surface held at the HER equilibrium potential. This data was calculated using COMSOL (See Chapters 3 and 6).

phosphorus to make a thin n-type layer. This is a p-n junction and is routinely used in silicon solar cells. As mentioned earlier, the Fermi level of an isolated SC depends on its doping concentration. For a p-type SC, the Fermi level is near the VB. For an n-type SC, the Fermi level is near the CB. Figure 2.11 shows the resulting band structures for this type of interface. Since the p and n components of the Si equilibrate with each other, the amount of band bending is set without any influence by the electrolyte. This strategy effectively decouples the barrier height from the electrolyte potential, allowing for significantly improved barrier heights and improved charge utilization. A product of using this strategy is explained in Chapter 6.

2.6 Conclusion

This chapter explained the photocatalytic water splitting process for the purpose of making hydrogen from sunlight and water. Photoelectrochemistry was introduced as a means of breaking down the system into more manageable components to enable the investigation and optimization of specific mechanisms. The physics of semiconductors and the materials with which they form composite devices were discussed in detail, identifying sources of loss in these devices. The following chapters will expand on this knowledge and show its application towards developing more efficient photoelectrochemical devices.

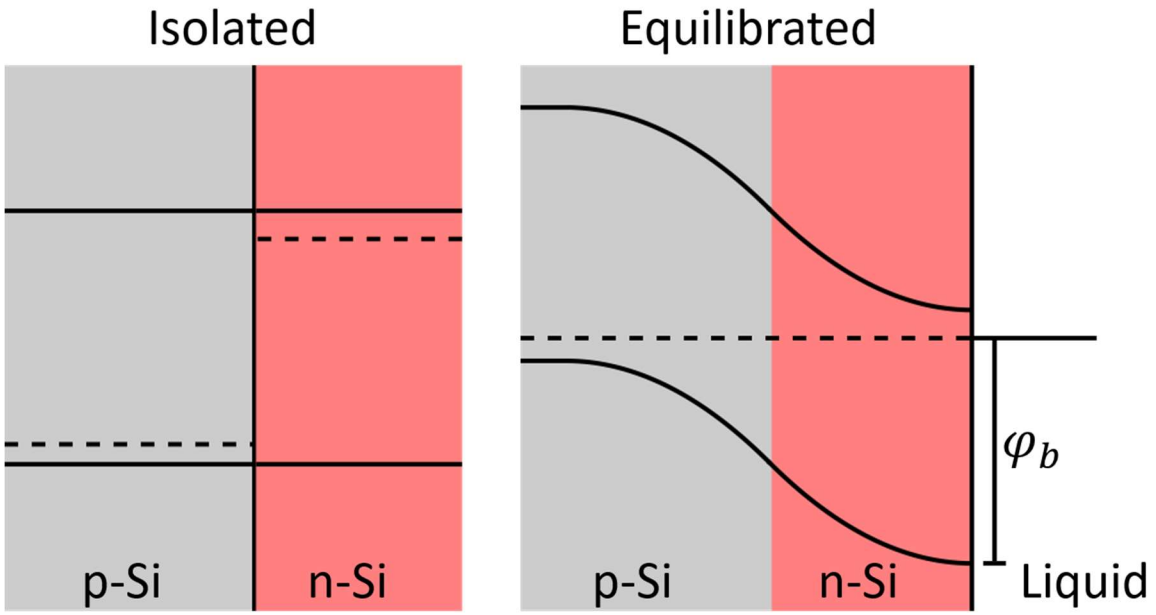

Figure 2.11: Increased barrier heights with p-n junctions. (Left) P-type and n-type Si bands assuming they are isolated from each other. (Right) The equilibrated p-n Si/electrolyte system. The barrier height is no longer tied to the electrolyte potential. Instead, the barrier height is the difference between the VB minimum and the Fermi level of the n-type Si in isolation.

2.7 References

(1) Nozik, A. Physical Chemistry of Semiconductor-Liquid Interfaces. *J. Phys. Chem.* **1996**, *3654* (95), 13061–13078.

(2) Walter, M.; Warren, E.; McKone, J. R.; Boettcher, S. W.; Mi, Q.; Santori, E. A.; Lewis, N. S. Solar Water Splitting Cells. *Chem. Rev.* **2010**, *110* (11), 6446–6473.

(3) Tyagi, M. S.; Van Overstraeten, R. Minority Carrier Recombination in Heavily-Doped Silicon. *Solid. State. Electron.* **1983**, *26* (6), 577–597.

(4) Salvador, P. Hole Diffusion Length in N-TiO2 Single Crystals and Sintered Electrodes: Photoelectrochemical Determination and Comparative Analysis. *J. Appl. Phys.* **1984**, *55* (8), 2977.

(5) Leng, W. H.; Barnes, P. R. F.; Juozapavicius, M.; O'Regan, B. C.; Durrant, J. R. Electron Diffusion Length in Mesoporous Nanocrystalline TiO_2 Photoelectrodes during Water Oxidation. *J. Phys. Chem. Lett.* **2010**, *1* (6), 967–972.

(6) Kreibig, U.; Vollmer, M. *Optical Properties of Metal Clusters*; Springer Series in Materials Science; Springer Berlin Heidelberg: Berlin, Heidelberg, 1995; Vol. 118.

(7) Shockley, W.; Queisser, H. J. Detailed Balance Limit of Efficiency of P-N Junction Solar Cells. *J. Appl. Phys.* **1961**, *32* (3), 510.

(8) Green, M. A.; Keevers, M. J. Optical Properties of Intrinsic Silicon at 300 K. *Prog. Photovoltaics Res. Appl.* **1995**, *3* (3), 189–192.

(9) Adachi, S. Optical Constants of Crystalline and Amorphous Semiconductors; Springer US: Boston, MA, 1999.

(10) Kim, T. W.; Choi, K.-S. Nanoporous $BiVO_4$ Photoanodes with Dual-Layer Oxygen Evolution Catalysts for Solar Water Splitting. Science **2014**, 343 (6174), 990–994.

(11) Lin, F.; Boettcher, S. W. Adaptive Semiconductor/electrocatalyst Junctions in Water-Splitting Photoanodes. Nat. Mater. **2014**, 13 (1), 81–86.

(12) Hou, Y.; Abrams, B.; Vesborg, P. Bioinspired Molecular Co-Catalysts Bonded to a Silicon Photocathode for Solar Hydrogen Evolution. Nat. Mater. **2011**, 10 (6), 434–438.

(13) Kay, A.; Cesar, I.; Grätzel, M. New Benchmark for Water Photooxidation by Nanostructured Alpha-Fe_2O_3 Films. JACS **2006**, 128 (49), 15714–15721.

(14) Becquerel. Recherches Sur Les Effets de La Radiation Chimique de La Lumiere Solaire Au Moyen Des Courants Electriques. *Comptes Rendus L´Academie des Sci.* **1839**, *9*.

(15) Fujishima, A.; Honda, K. Electrochemical Photolysis of Water at a Semiconductor Electrode. *Nature* **1972**, *238* (5358), 37–38.

(16) Nørskov, J. K.; Bligaard, T.; Logadottir, A.; Kitchin, J. R.; Chen, J. G.; Pandelov, S.; Stimming, U. Trends in the Exchange Current for Hydrogen Evolution. *J. Electrochem. Soc.* **2005**, *152* (3), J23.

(17) Holton, O. T.; Stevenson, J. W. The Role of Platinum in Proton Exchange Membrane Fuel Cells. *Platin. Met. Rev.* **2013**, *57* (4), 259–271.

(18) Pourbaix, M.; Staehle, R. W. *Lectures on Electrochemical Corrosion*; Springer US: Boston, MA, 1973.

(19) Beverskog, B.; Puigdomenech, I. Revised Pourbaix Diagrams for Nickel at 25–300 °C. *Corros. Sci.* **1997**, *39* (5), 969–980.

(20) Pourbaix, M. J. N.; Van Muylder, J.; de Zoubov, N. Electrochemical Properties of the Platinum Metals. *Platin. Met. Rev.* **1959**, *3* (2).

(21) Maier, S. A. *Plasmonics: Fundamentals and Applications*; Springer, 2007.

(22) Ingram, D. B.; Linic, S. Water Splitting on Composite Plasmonic-Metal/Semiconductor Photoelectrodes: Evidence for Selective Plasmon-Induced Formation of Charge Carriers near the Semiconductor Surface. *J. Am. Chem. Soc.* **2011**, *133* (14), 5202–5205.

(23) Linic, S.; Christopher, P.; Ingram, D. B. Plasmonic-Metal Nanostructures for Efficient Conversion of Solar to Chemical Energy. *Nat. Mater.* **2011**, *10* (12), 911–921.

(24) Bard, A. J.; Bocarsly, A. B.; Fan, F. R. F.; Walton, E. G.; Wrighton, M. S. The Concept of Fermi Level Pinning at Semiconductor/liquid Junctions. Consequences for Energy Conversion Efficiency and Selection of Useful Solution Redox Couples in Solar Devices. *J. Am. Chem. Soc.* **1980**, *102* (11), 3671–3677.

(25) Zhang, Z.; Yates, J. T. Band Bending in Semiconductors: Chemical and Physical Consequences at Surfaces and Interfaces. *Chem. Rev.* **2012**, *112* (10), 5520–5551.

(26) Liu, R.; Zheng, Z.; Spurgeon, J.; Yang, X. Enhanced Photoelectrochemical Water-Splitting Performance of Semiconductors by Surface Passivation Layers. *Energy Environ. Sci.* **2014**, *7* (8), 2504.

(27) Hamann, T. W.; Lewis, N. S. Control of the Stability, Electron-Transfer Kinetics, and pH-Dependent Energetics of Si/H_2O Interfaces through Methyl Termination of Si(111) Surfaces. *J. Phys. Chem. B* **2006**, *110* (45), 22291–22294.

(28) Seger, B.; Pedersen, T. Using TiO_2 as a Conductive Protective Layer for Photocathodic H_2 Evolution. *J. Am. Chem. Soc.* **2013**, *135* (3), 1057–1064.

(29) Lewis, N. S. Chemical Control of Charge Transfer and Recombination at Semiconductor Photoelectrode Surfaces. *Inorg. Chem.* **2005**, *44* (20), 6900–6911.

(30) Musumeci, F.; Pollack, G. H. Influence of Water on the Work Function of Certain Metals. *Chem. Phys. Lett.* **2012**, *536*, 65–67.

(31) Seah, M. P. Work Function. In *Tables of Physical & Chemical Constants*; Kaye & Laby Online, 2005.

(32) Esposito, D. V; Levin, I.; Moffat, T. P.; Talin, A. A. H_2 Evolution at Si-Based Metal-Insulator-Semiconductor Photoelectrodes Enhanced by Inversion Channel Charge Collection and H Spillover. *Nat. Mater.* **2013**, *12* (6), 562–568.

CHAPTER 3

Experimental and Computational Methods

3.1 Summary

The purpose of this chapter is to give an overview of the experimental and computational methods used to complete this dissertation. Application-specific descriptions of these methods are provided in their respective chapters. The first section in this chapter explains the synthesis methods frequently used in this work. In the next section, the optical and electron microscopy techniques are explained. After that, the photoelectrochemical (PEC) characterization strategies for the hydrogen evolution reaction (HER) are discussed. The final two sections discuss the optical calculations and charge transport calculations performed, respectively.

3.2 Synthesis Methods

3.2.1 Silicon Preparation

Silicon wafers, either as-received or after doping (Subsection 3.2.2), were diced into 13 or 28 mm squares using an ADT 7100 dicing saw at the Lurie Nanofabrication Facility (LNF). The 13 mm squares were used as electrode materials, while the 28 mm squares were used for optical characterization. They were soaked in acetone for 10 minutes and then thoroughly rinsed with ultrapure water. To remove any remaining organic impurities, the chips were submerged in piranha solution (3:1 sulfuric acid and hydrogen peroxide by

volume) for three hours. They were then rinsed in ultrapure water and dried under compressed air. Once dry, they were sealed in petri dishes until use to avoid any contamination.

3.2.2 P-N Junctions

P-type Si wafers were transformed into pn-Si wafers through a series of steps at the LNF using a standard deposition and drive-in method. The Si wafers were first cleaned and etched to remove the native oxide layer. A thermal oxide was grown onto the entire Si surface, and photoresist was coated onto the back of the wafer. The wafers were exposed to another etching step, and only the oxide on the front of the wafers was removed because the photoresist on the back side protected the oxide. The photoresist was then removed, resulting in Si wafers with a thermal oxide layer on only the back of the wafers. The wafers were loaded into a furnace and exposed to a $POCl_3$ atmosphere. The temperature in the furnace was held at 975°C for 20 minutes, causing P atoms to diffuse into the front side of the wafers. The wafers were then removed from the furnace and then etched to remove the oxide on the back of the wafers. The junction depth (the depth at which the concentrations of the donor and acceptor atoms is equal) was estimated to be about 500 nm with a peak P atom concentration of 10^{20} atoms/cm^3.

3.2.3 Electroless Deposition of Metal Nanoparticles

Metal nanoparticles were deposited onto Si through an electroless deposition process.[1–3] This deposition strategy was based on the concurrent dissolution of the Si surface and reduction of metal ions/complexes onto the Si surface. For this work, an oxide-free Si chip was submerged in a 10 mL aqueous solution of 1 mM hexachloroplatinic

acid (H_2PtCl_6) and 0.25 M HF for 2 minutes. After this deposition, the Si was thoroughly rinsed with ultrapure water and dried under compressed air.

Equation 3.1 shows that HF dissolves the Si at the surface of the electrode, releasing electrons that have a significant amount of potential to drive reduction reactions.

3.1 $$\mathrm{Si + 6HF \rightarrow SiF_6^{2-} + 6H^+ + 4e^-} \quad (E^0 = -1.20\ \mathrm{V\ vs.\ NHE})$$

These electrons then reduce the Pt complexes that collide into the Si, forming metallic Pt on the surface of the Si, as shown in Equation 3.2.

3.2 $$\mathrm{H_2PtCl_6 + 4e^- \underset{Si}{\rightarrow} Pt + 6Cl^- + 2H^+} \quad (E^0 = 0.73\ \mathrm{V\ vs.\ NHE})$$

This reduction process proceeds because the electrons coming from the Si oxidation have enough energy to reduce the Pt^{4+} ions. This deposition method is applicable with other metal ions/complexes that have positive reduction potentials relative to the normal hydrogen electrode (NHE). For example, this includes Ag^+ (0.80 V vs. NHE), Cu^{2+} (0.34 V vs. NHE), and $AuCl_4^-$ (0.93 V vs. NHE).[4] Ni^{2+} (-0.26 V vs. NHE), however, is not as easily reduced into particles with method because the HER (0 V vs. NHE) competes with the nickel ion reduction.[5]

3.2.4 Selective Etching of Silicon with Pt Nanoparticles

Once Pt nanoparticles were deposited on a Si surface via electroless deposition, they could be embedded into the Si through a selective etching process based on a method used by Tsujino and Matsumura.[6–8] The Si chip laden with Pt nanoparticles was submerged in a 10 mL solution of 2.2 M HF and 0.16 M H_2O_2 for about 45 seconds. The chip was then thoroughly rinsed in ultrapure water and dried under compressed air. In this embedding process, the Pt nanoparticles act as catalysts for dissolving the Si that is directly

in contact with the particles, resulting in the burrowing of the Pt particles into the Si. The H_2O_2 oxidizes at the Pt surface, which allows the injection of energetic holes into the Si at the Si/Pt interface. At this interface, the HF and holes drive the dissolution of Si, causing the formation of pores. The process forms Si with pores typically 100 to 300 nm deep with a Pt nanoparticle at the bottom of each pore for the conditions used in this work.

3.3 Characterization Tools and Methods

This section describes the various tools and experimental techniques that have been used to characterize the materials discussed in this dissertation, specifically optical spectroscopy and electron microscopy techniques. All PEC tools and techniques used are discussed in the following section.

3.3.1 UV-Vis Transmission Spectroscopy

This optical characterization technique measures the rate of photons passing through a solid or liquid sample relative to the rate of photons illuminating the sample as a function of wavelength. The particular device used for this work, a Thermo Scientific Evolution 300 UV-Vis Spectrometer, uses an internal Xe lamp and a monochromator to pass small bands of light from 190 to 1100 nm to the sample. Once the light interacts with the sample, it can be reflected/scattered, absorbed, or transmitted. The transmitted light is collected at a detector. Since only the transmitted light is collected, the other fates of the photons cannot be differentiated from each other with this method. This technique was primarily used to confirm that the Si chips used in this work were optically transparent within a particular range of wavelengths.

3.3.2 Light Sources

Two types of light sources were used in this work. The first is a Dolan-Jenner Fiber-Lite® Model 180 Lamp equipped with a flexible fiber optic light guide. This is a broadband light source that uses a 150 W quartz halogen lamp. The power output from this lamp is coarsely controlled on the unit by a dial on the device. Finer control is achieved by operating this lamp in series with a Variac® variable transformer. Based on measurements using a thermopile detector (see Subsection 3.3.3), the maximum light irradiance (i.e., flux density) possible from this lamp is 800 mW/cm^2. The spectral shape of this output is shown in Figure 3.1.

The second light source is a lamp and monochromator system based on components purchased from the Newport Corporation. A pair of photographs are shown in Figure 3.2 that depict this complex system. The output of a 1000 W Xe lamp is first fed through a water filter. This device has chilled water passing through it and absorbs a large portion of the infrared component of the light. This is necessary to prevent the exposure of sensitive hardware in this system to extreme temperatures. The filtered light is then sent to a Cornerstone 260 monochromator. Diffraction gratings inside the monochromator are set at specific angles relative to the incoming beam of light to spatially separate the beam of light into different wavelengths. This allows the wavelength of light leaving the monochromator to be accurately controlled. The entrance and exit slits on the monochromator were set to maximize the power output at each wavelength, resulting in full width at half maximum bandwidths of no more than 40 nm. A filter wheel is located at the exit of the monochromator to remove any higher diffraction order contributions (e.g., 300 nm light will have a small amount of 600 nm and 900 nm light in it without the

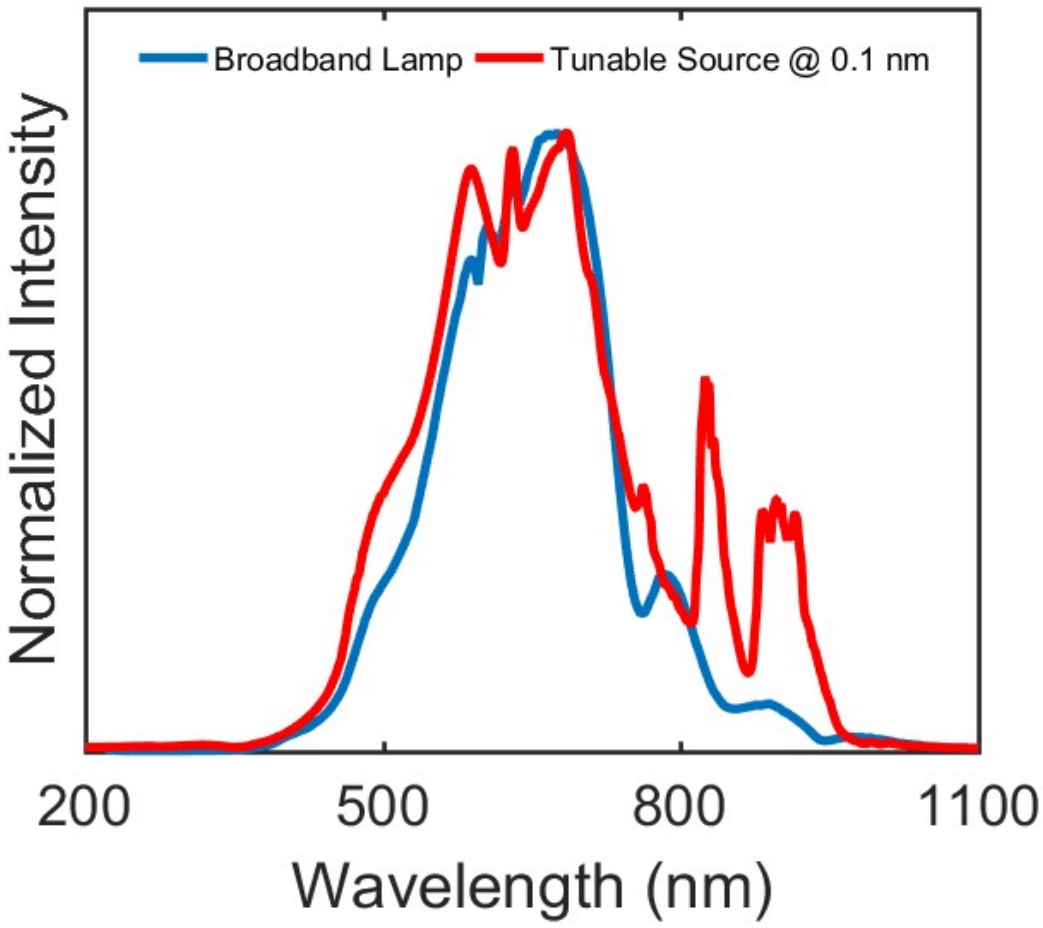

Figure 3.1: Spectral shapes of the broadband light sources. The relative spectral output of the broadband light source at its maximum power setting is shown in blue. The data in red was gathered by setting the tunable light source wavelength to 0.1 nm (This is described in detail below). These spectra were measured using an Avantes AvaSpec-2048-USB2 spectrometer. The spectrum for the broadband lamp red-shifts slightly when lower power settings are used.

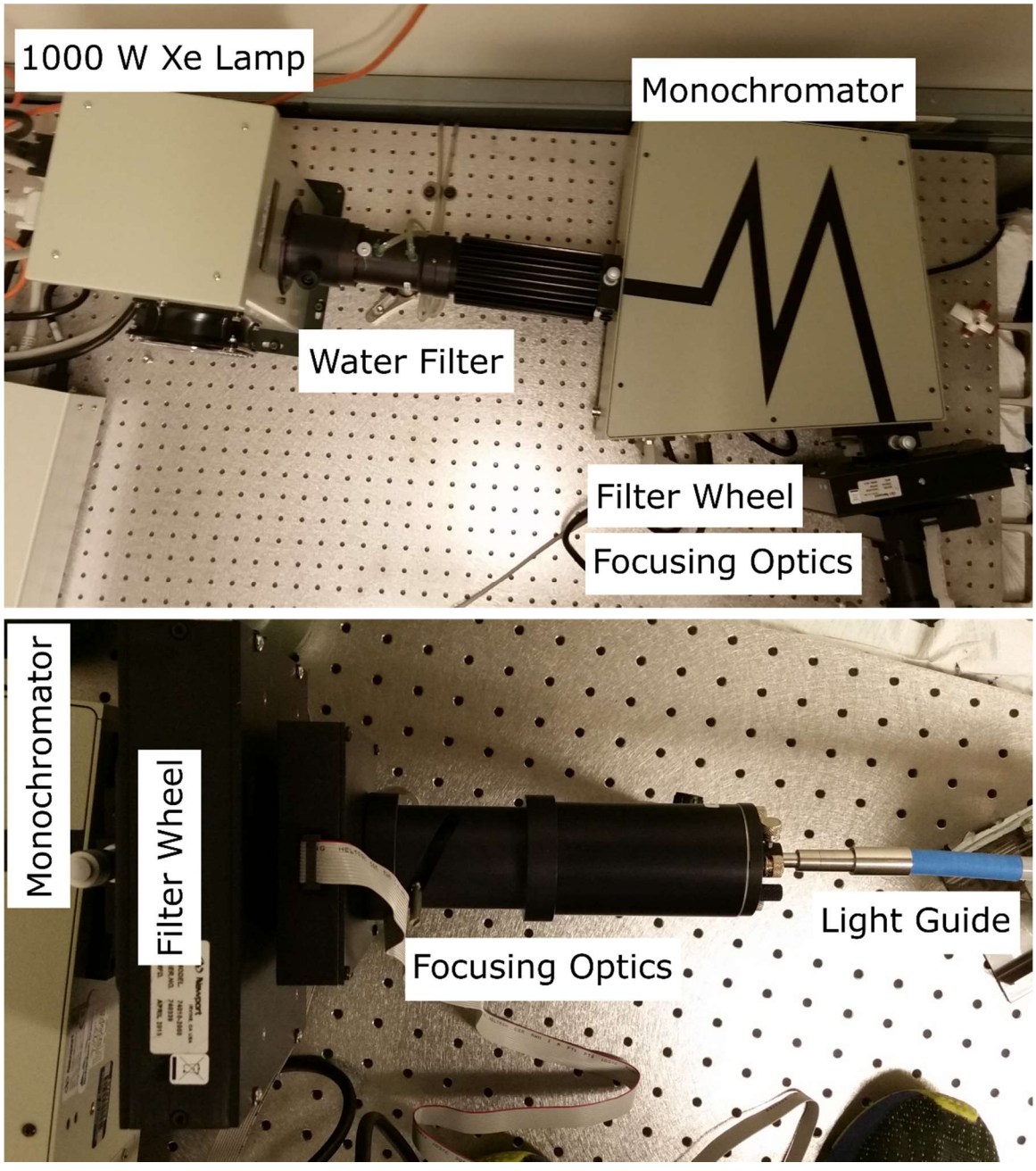

Figure 3.2: Photographs of the tunable light source based on a 1000 W Xe lamp and a Cornerstone 260 monochromator from the Newport Corporation.

filter wheel.). Following the filter wheel, the light is focused by lenses to efficiently direct the light into a light guide. The light guide is flexible and allows the light to be delivered to various experimental tools. There is a shutter at the end of the focusing optics that can be used to block the light. The irradiance of this tunable source at various wavelength settings is shown in Figure 3.3.

The tunable light source can also be configured to output broadband light. When the monochromator is set to output 0.1 nm light (not physically meaningful for this light source), the diffraction grating is set at an angle such that it mimics a mirror. This results in a beam of light with a spectral shape shown in Figure 3.1. The irradiance of this beam exiting the light guide is 25 mW/cm^2, based on a thermopile detector measurement.

3.3.3 Measurement of Light Source Output

In this field, it is absolutely vital to know the overall irradiance and wavelength-specific irradiance of the light sources being used in experiments. Two different types of detectors are used for this purpose: a photodiode and a thermopile detector. In general, the photosensitive material in a detector has a specific response to different wavelengths of light.

In a thermopile detector, incoming photons are absorbed and cause the local temperature to increase. A potential is generated through the thermoelectric effect, and this potential can be measured and be correlated to the incident photon flux. The spectral responsivity of the particular thermopile detector used (Newport 818P-010-12) is relatively flat across the range of wavelengths from 190 nm to 20 μm. As a result, this detector is ideal for measuring the total power output from a broadband light source.

In a photodiode detector, the absorbing material essentially acts like a solar cell;

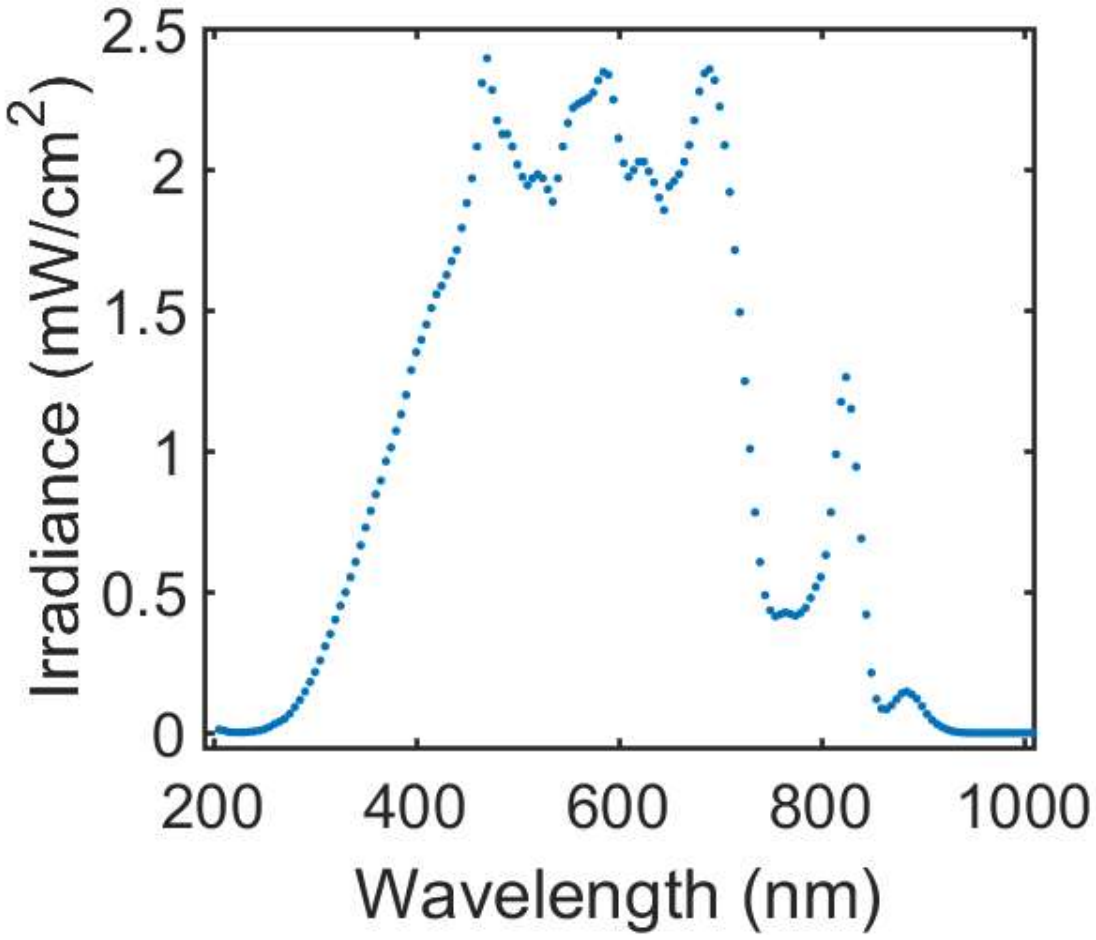

Figure 3.3: Irradiance of the tunable light source at the light guide exit for different wavelength settings from 205-1000 nm with 5 nm between each point. The power output was measured using the photodiode detector and was normalized by the area of the light guide exit (0.20 cm^2).

the absorbed photons are converted into current, which is then correlated to the incoming photon flux. These devices have responsivities that strongly depend on wavelength and are more sensitive than thermopile detectors. This means that photodiode detectors are well-suited for measuring the irradiance of beams of monochromatic light with relatively low photon fluxes, such as the light from the tunable light source described in Subsection 3.3.2. The photodiode detector used in this work (Newport 918D-UV-OD3R) is able to measure irradiance from 200 nm to 1100 nm, and comes with an attenuation filter that can be deactivated to measure the irradiance of very weak beams of light.

3.3.4 Reflectance Spectroscopy

The reflectance of the materials used in this dissertation was measured by shining light from the tunable light source (described in Subsection 3.3.2) onto the material being characterized inside a 6 inch diameter integrating sphere purchased from LabSphere. Unlike with a UV-Vis spectrometer, this device enables the measurement of the reflectance of a surface, independent of the absorptance. An integrating sphere is a hollow sphere with its interior coated by a very reflective material (Spectraflect®). A sketch of a type of integrating sphere used for this dissertation is shown in Figure 3.4. In this particular design, the sample being characterized is mounted in the center of the sphere and can be rotated to measure the reflectance as a function of the illumination angle. Light is sent into the sphere via a small port, and a baffle is positioned so that light cannot bypass the sample and reach the detector. The photodiode detector is used for these measurements, and the attenuation filter is deactivated because the amount of light reaching the detector is very low. Incident light reflects off the sample and can be specularly (i.e. like a mirror) or diffusely reflected. The specular reflectance can be captured by attaching a trap to an

appropriate port on the sphere. When measurements are taken with and without the trap, the specular and diffuse reflectance can be differentiated from each other. In general, the total reflectance was all that was needed in this work, so the trap was not used. The light reflecting off the sample surface then reflects inside the sphere until it is collected by the detector. To determine the absolute reflectance, a reference material (Spectralon®) that is nearly 100% reflective across the visible spectrum is used as a sample in the sphere to define the signal at the detector that corresponds to nearly 100% reflectance. If the sample being characterized transmits no light at the wavelengths of interest, as was the case with the silicon chips used in this work, the absorptance by the sample is equal to one minus the reflectance.

Since the distance from the end of the light guide (with a focusing lens on the end) to the sample in the center of the sphere is about 3 inches, there is a significant broadening of the incident beam of light. As discussed in Subsection 3.2.1, the Si chips used for these measurements are quite large (28 mm squares) compared to the chips used for PEC measurements (13 mm squares). This is done to ensure that all of the incident light illuminates the sample before any other part of the integrating sphere. If this is not accomplished, the measured reflectivity is higher than it should be.

3.4 Characterization at the Nanoscale

The materials and geometric features synthesized in this work are too small to be adequately characterized by optimal microscopy. Therefore, the use of scanning and transmission electron microscopy (SEM and TEM) was heavily relied upon as a means of identifying the results of certain synthesis steps and acting as a feedback loop to troubleshoot synthesis issues. Energy-Dispersive X-Ray Spectroscopy (EDS) was used to

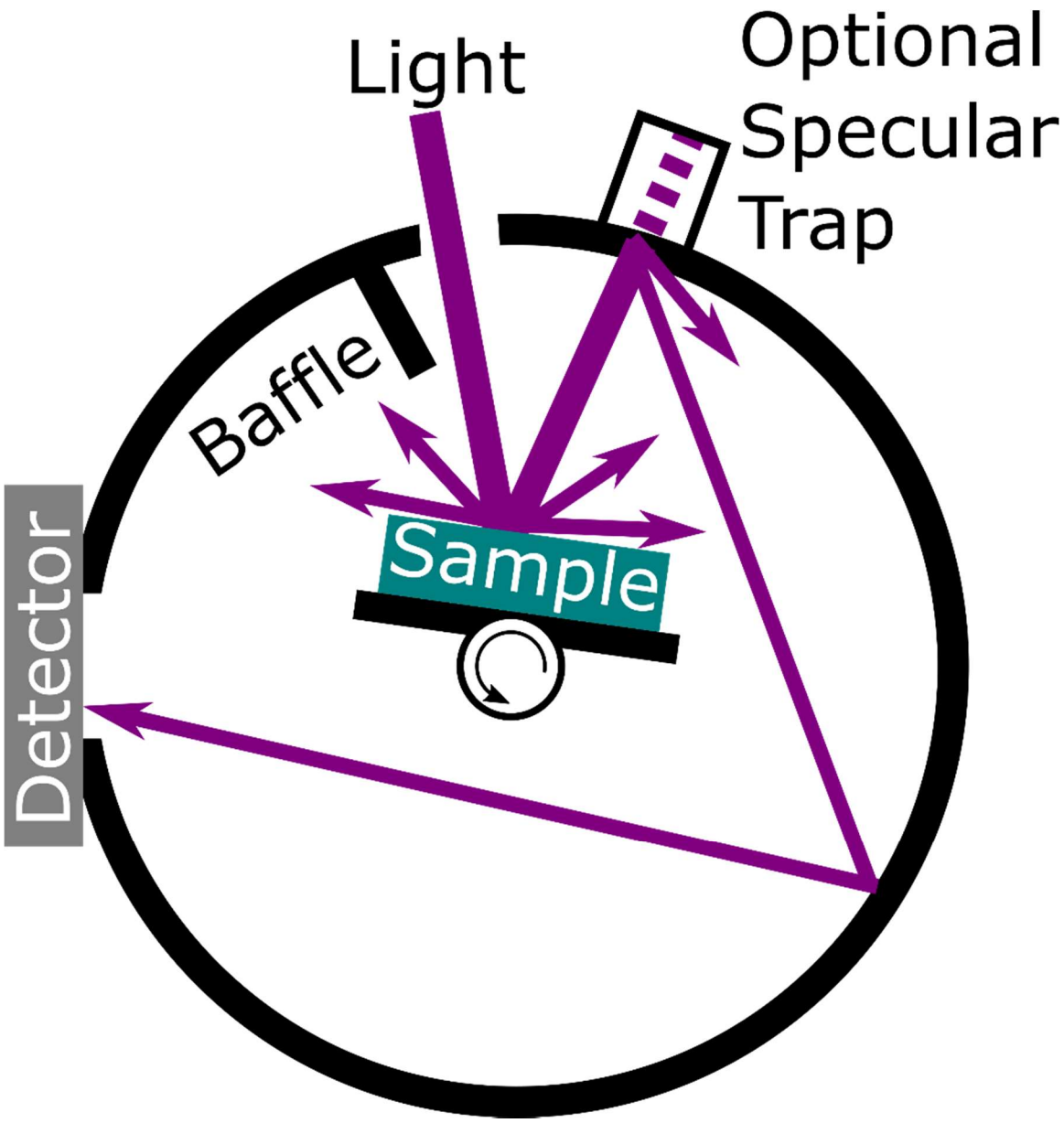

Figure 3.4: Sketch of a cross-section of an integrating sphere for measuring optical properties. Light that reflects off the sample surface is collected at the detector.

qualitatively identify the chemical compositions of regions in a sample.

3.4.1 Electron Microscopy

In SEM, an electron beam with an energy between 0.2 and 30 kV is directed toward the sample surface under high vacuum, and the reflected (secondary) electrons are collected at a detector. The beam sweeps over the surface and generates an image based on the change in the detected signal.

The Philips XL30 FEG SEM at the Michigan Center for Materials Characterization (MC^2) was mostly used for troubleshooting materials synthesis issues because it is not in very high demand due to the fact that it can only achieve a peak resolution of 2 to 5 nm.

For publication-quality imaging, the FEI Nova 200 NanoLab was used due to its superior resolutions between 1.1 and 3.5 nm. Additionally, this equipment has a focused ion beam (FIB) and a Pt gas injector that allows for the preparation of cross-sections of samples. Pt is deposited onto the sample surface to protect it during the FIB milling process. This milling cuts away parts of the sample, providing a line-of-sight for the electrons to image the exposed surface. This process is also used to cut out thin specimens from a sample to be used for TEM.

In TEM, the electron beam is directed onto a sample that is so thin that is can transmit electrons. These transmitted electrons can be collected to generate bright-field images, or scatted electrons can be collected to generate dark-field images. The dark-light contrast seen in both types of images is related to the thickness of the sample and the density of the material at a specific location.

An aberration corrected JEOL 2100F was used at MC² to perform TEM. TEM was performed in this work to generate high resolution cross-sectional images of Si/Pt systems. This is superior to SEM because it can achieve resolutions as low as 0.1 nm.

3.4.2 Energy-Dispersive X-Ray Spectroscopy

EDS was performed with both SEM and TEM and was used specifically to identify the chemical make-up of specific features on the Si/Pt surfaces. In EDS, an electron beam is used to interact with inner shell electrons in atoms, causing the incident electrons and the inner shell electrons to be scattered away from the atom. X-rays are released when outer shell electrons relax to occupy the inner shell vacancy and are collected. The energies of the X-rays correspond to the elemental composition of the irradiated atoms. Differences in the composition over space can then be mapped to depict the existence of specific elements in certain areas.

3.5 Photoelectrochemistry Equipment

3.5.1 Photoelectrochemical Cell and Potentiostat

Since only the HER component of water splitting is studied in this dissertation, and not a complete water splitting device, a three-electrode PEC cell and a potentiostat must be used to adequately characterize the electrode's efficiency. Figure 3.5 provides a diagram of this system. The three-electrode PEC cell consists of a working electrode, reference electrode, a counter electrode, electrolyte, a magnetic stir bar, and a light source that illuminates the working electrode through the cell wall. The PEC cell is based on a 200 ml Pyrex beaker that has notches cut into it to interface with an electrode holder (Subsection 3.5.2 and Figure 3.6).

The working electrode is the material being evaluated for its HER efficiency (the composite Si/metal photoanode). The reference electrode is used to measure the potential at the working electrode and, therefore, is intended to have an electrode potential that does not change over a wide range of operating conditions.[9] For this work, the reference electrode is a mercury/mercurous sulfate electrode (MSE, Hg/Hg_2SO_4 in saturated K_2SO_4) with a potential of 0.65 V vs. NHE. The counter electrode, a Pt wire, is used to preserve the balance of charge in the system (i.e., if the working electrode is driving reduction reactions, the counter electrode must perform oxidations at the same rate.) The electrolyte used is either 1 M or 0.1 M $HClO_4$.

Hydrogen gas is bubbled into the electrolyte, which establishes an electrolyte potential of 0 V vs. the reversible hydrogen electrode (RHE), to promote stable behavior. The presence of hydrogen gas also forces the counter electrode reaction to be hydrogen oxidation (0 V vs. RHE). This is important because it means the counter electrode can operate at potentials that do not risk oxidizing or dissolving the Pt, releasing Pt ions into the electrolyte that would interfere with measurements. The hydrogen also minimizes the dissolved oxygen concentration in the electrolyte, which is vital for evaluating the HER behavior instead of a combined HER/oxygen reduction reaction (ORR) process.

The potentiostat (Gamry Reference 3000) is connected to the three electrodes in the PEC and is responsible for applying potential to the working electrode, as well as measuring the resulting responses. This device can operate in various modes; they are described in Section 3.6. In its most basic configuration, the potentiostat controls the potential applied to the working electrode relative to the reference electrode and measures the current passing from the working to counter electrode.

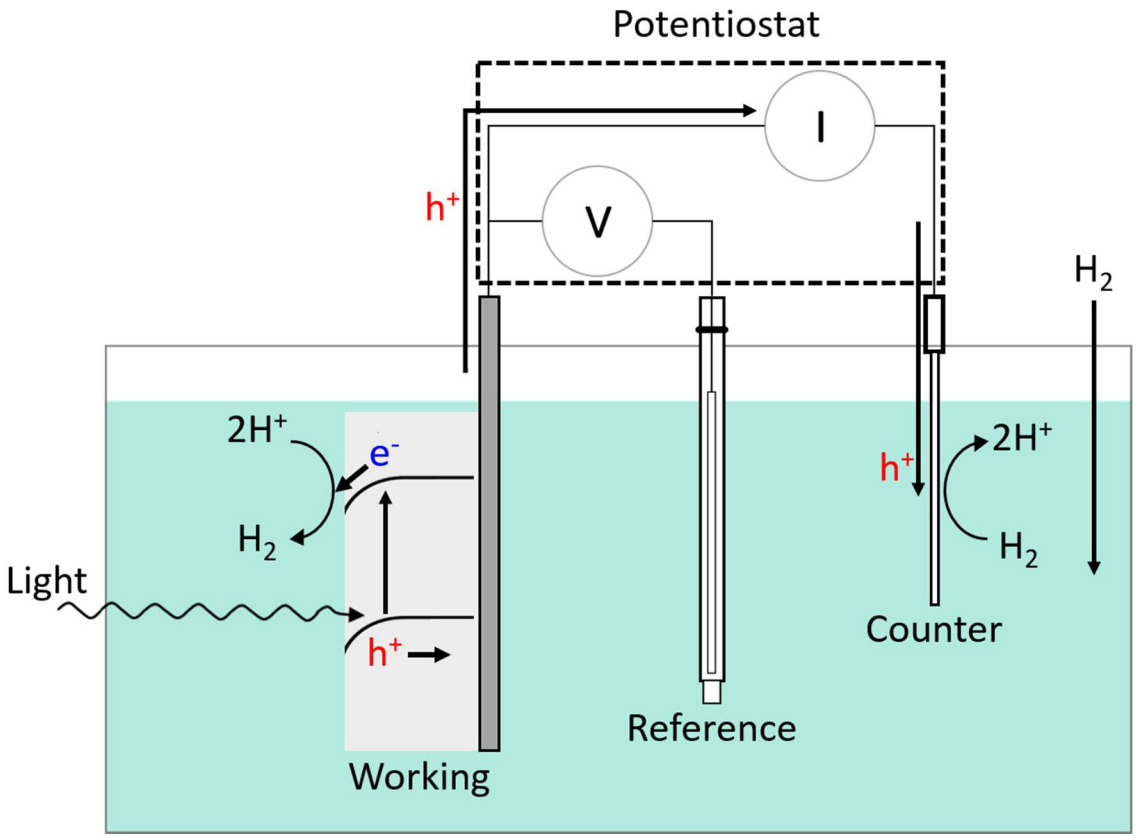

Figure 3.5: Diagram of the setup used to perform PEC characterizations for the HER on the working electrode.

3.5.2 Electrode Construction

To make an electrode, a Si chip is submerged in 10 ml of 0.5 M hydrofluoric acid (HF) for 15 minutes to remove the native oxide layer that spontaneously grows when exposed to air. A gallium-indium eutectic is coated on the back side of the chip immediately after it is scratched with a diamond scribe to quickly make a reliable back contact. Figure 3.6 shows a schematic of a device used to house the Si electrodes for all PEC measurements. It was designed using computer-aided-design software and then 3D printed at the UM3D Lab using VisiJet M3 Black, a polymer produced by 3DSystems. This device is used to ensure that the exposed surface areas of different electrodes are identical by using an O-ring and a faceplate with a 0.25 cm^2 aperture to define the exposed area. The device integrates with PEC cells via interlocking parts to reproducibly position the electrode in the incident beam of light. This keeps the incident photon flux constant for different electrodes.

3.6 Photoelectrochemical Measurements

This section discusses the different types of experiments performed using the PEC cell and potentiostat to evaluate Si/Pt-based HER photocathodes. The guiding principles, the standard operating conditions, and the data analysis methods associated with these methods are described. From this point forward, current will be discussed in the form of current density, which is the current divided by the projected area of the electrode. All measurements are performed in a dark room to prevent ambient light from generating current. Explanations for the various MATLAB scripts used to analyze these data are provided in Appendix A.

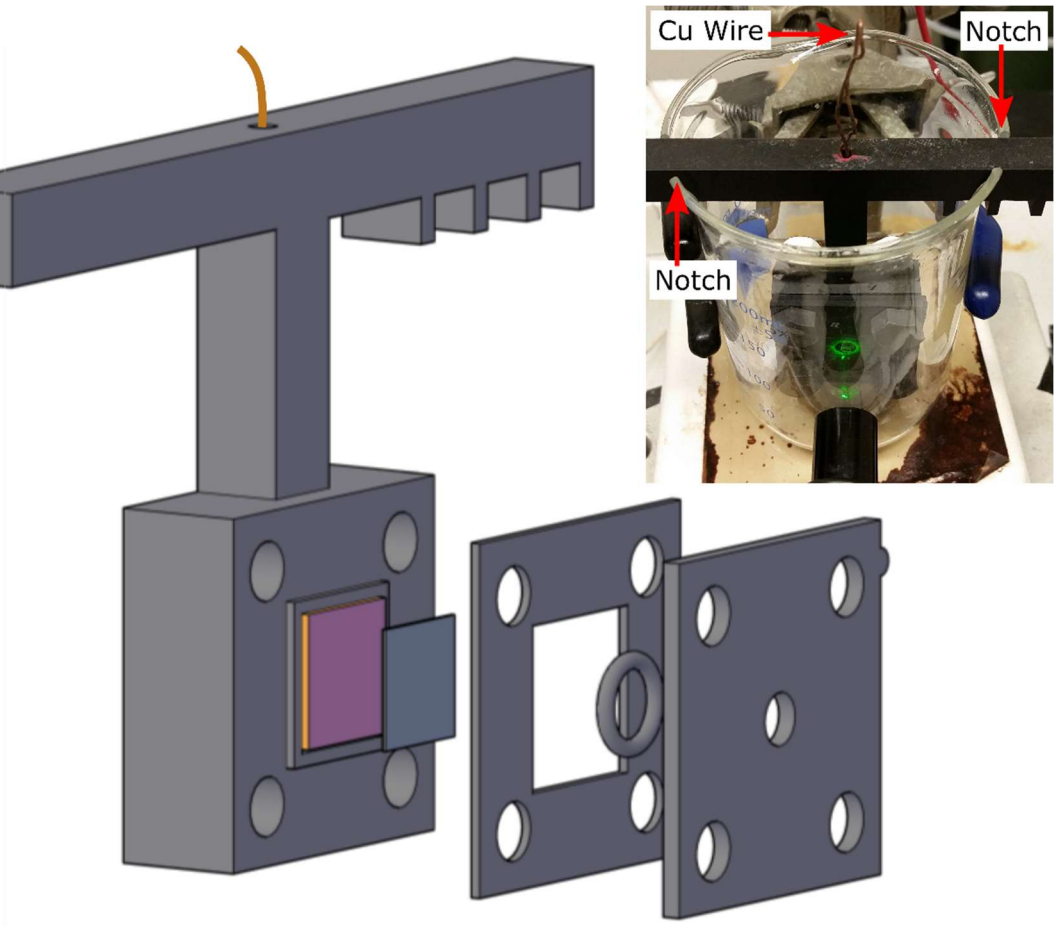

Figure 3.6: 3D printed electrode holder and photoelectrochemical cell (Left) Schematic of the 3D printed electrode holder. Parts from left to right: Main housing with a Cu plate, Si chip, rubber gasket, O-ring, and faceplate. The notches on the T-bar of the main housing enable the holder to be locked into the PEC cell to ensure reproducible photocurrent measurements. The faceplate is fixed to the main housing via plastic nuts and bolts fed through the holes in the corners of the housing, gasket, and faceplate. Inside the main housing, there is a metal spring that contacts the Cu plate and allows the passage of current to a Cu wire that is fed through the shaft of the holder to provide a means of applying potential to the back contact of the Si chip. (Top Right) Photograph of the PEC cell with the electrode holder locked into place by inserting the crossbar into the notches cut into the beaker. With the light guide in a fixed position as well, this ensures that that different electrode samples experience the same photon flux.

3.6.1 Cyclic Voltammetry

Cyclic voltammetry (CV) measures the current that passes through the working electrode while the potential is swept linearly with respect to time from one potential to another and then back to the original potential. This sweeping pattern is repeated over multiple cycles to capture the performance under illuminated and dark conditions. The results of these measurements are presented as current density or photocurrent density vs. potential plots. Photocurrent is the difference in the currents measured under illuminated and dark conditions. In Figure 3.7, the current density in the dark is negligible, which means the photocurrent density is equal to the current density. This is not always true.

One goal of these measurements is to identify the potential at which the working electrode has enough energy to perform the HER. This is known as the onset potential (E_{on}) and quantifies the extent of the kinetic limitations at the electrode surface. The definition of the onset is rather arbitrary and is reported using many different strategies.[10,11] In this work, the rate of photon absorption plays a significant role in the shape of the current-potential curves. Since the rate of absorption changes for different systems, it is important in this work to report the onset potential with a method that avoids bias due to different absorption rates. With this in mind, the half wave potential of these curves is used to report the onset potential. The half wave potential is defined as the potential where the current is equal to half of the photocurrent plus the background current.

Another goal is to identify the light-limited photocurrent density, which occurs when the HER rate is limited by the light-induced charge carrier generation rate instead of the surface reaction rate. This is identified by the region of a photocurrent density vs. potential plot where the photocurrent density is independent of the potential.

These measurements begin with the light shining into the cell and the Si electrode connected to the potentiostat, but not sitting in the electrolyte. The potentiostat is then activated and holds the working electrode at the initial potential, which is usually -1.35 V vs. RHE for p-Si electrodes and -0.85 V vs. RHE for pn-Si electrodes loaded with Pt. The electrode is then loaded into the PEC cell and locked into place. Putting the electrode into the electrolyte under potential control at strongly reducing potentials protects the electrode from premature oxidation. A pipette is then used to clear the Si surface of any bubbles. Great care should be taken to avoid the build-up of bubbles on the electrode surface because it reduces the reactive surface area and interferes with the incoming light.

At this point, the potential is allowed to sweep at a rate of 50 mV/s to 0.3 V vs. RHE for p-Si electrodes and 0.55 V vs. RHE for pn-Si electrodes loaded with Pt. It is important to carefully set this potential limit. The electrode experiences increasingly oxidative conditions as the potential sweeps in the positive direction. In aqueous solutions, the thermodynamic potential for the oxidation of Si is -0.85 V vs. RHE. The potential must be swept far beyond this value, which provides a strong driving force for the Si to oxidize during these measurements, which increases the kinetic limitation. Figure 3.7 shows the effect of this oxidation over a few CV cycles. When metals are used as electrocatalysts on the Si surface to drive the HER, this Si oxidation does not noticeably hinder the reaction rate. With metal on the surface, the positive potential limit must be monitored to prevent the oxidation or dissolution of the metal.[2] This is not usually an issue for Pt, because the potential must be above about 0.9 V vs. RHE to form Pt-oxides.[12]

[2] Ni, a common HER electrocatalyst that was not studied as part of this dissertation work, has a low threshold for oxidation of -0.26 V vs. NHE.[4] In such a system at low pH, a prudent upper limit on the potential would be

The potential is then swept back to the original potential. Depending on the particular experiment, multiple cycles can be performed under illumination to observe the system stability, or the shutter can be closed (or lamp turned off) to perform a dark measurement cycle.

3.6.2 Chronoamperometry and Light-Limited Photocurrent

Typical Chronoamperometry (CA) experiments aim to observe how the current from a working electrode changes over time when the potential is changed by a step function. The CA experiments used in this dissertation instead aim to determine the light-limited photocurrent generated by a working electrode as a function of wavelength. Instead of changing by a step function, the potential is held at the same potential as the initial CV potential (see Subsection 3.6.1). At these strongly reducing conditions, the working electrode current suffers from no kinetic losses. Instead, the current is limited by the rate at which photons can be converted into minority charge carriers that are able to reach the HER reaction site. This is directly related to how efficiently the semiconductor absorbs the incident light.

These measurements are typically performed in sequence with CV measurements. It is important to minimize the down-time between the end of the final CV cycle and the beginning of the CA measurement. During such a down-time, the electrode is resting at its open circuit potential (no current), which allows it to oxidize. By switching quickly from the CV to the CA measurement, the adverse effects of oxidation can be minimized.

Initially, the shutter on the tunable light source is closed while the potential remains

around -0.4 V vs. RHE, which is impractical. Ni HER electrocatalysis can be performed in buffered acids with pH > 4.5 to avoid this issue.

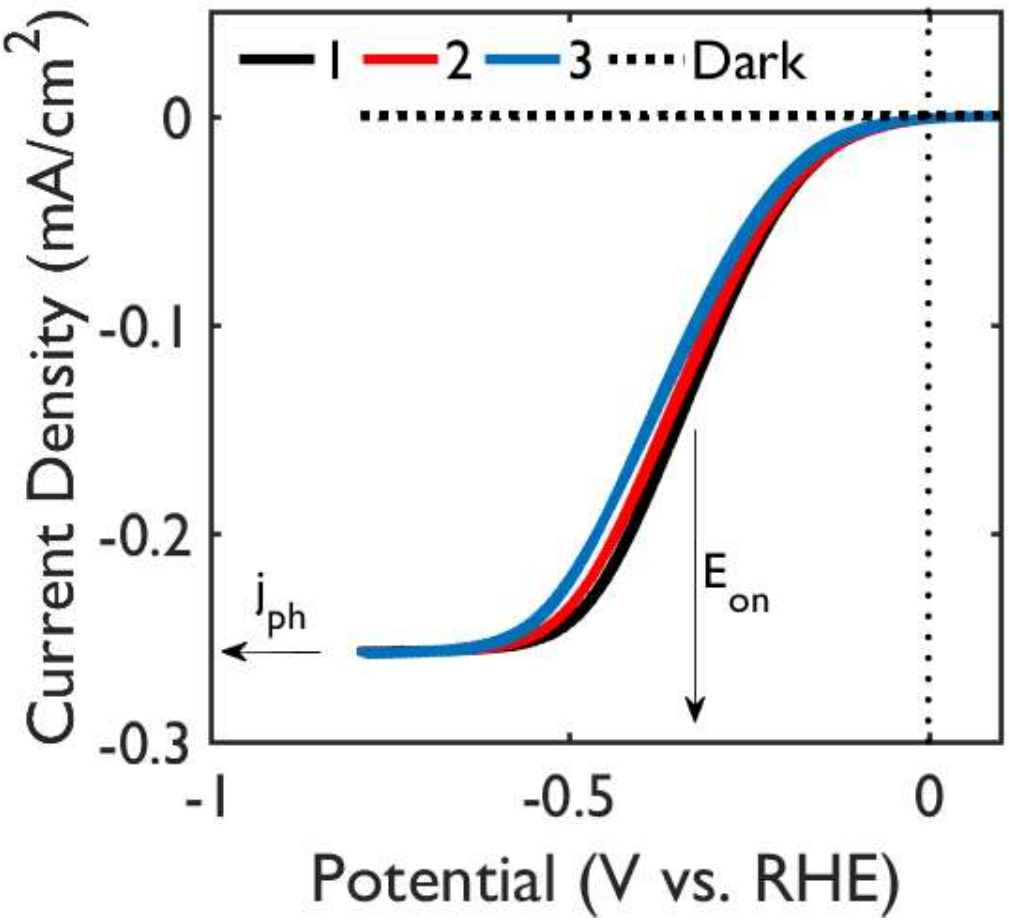

Figure 3.7: Typical CV measurements for an illuminated Si photocathode. Solid curves have numbers that correspond to the CV cycle. The dashed line is the response in the dark. The dotted line at 0 V vs. RHE designates the equilibrium potential for the HER. Since the dark current is negligible, the light-limited photocurrent (j_{ph}) can be directly observed in this plot with no mathematical manipulations. The onset potential (E_{on}) for the first cycle is identified using the half wave potential method. The illuminated curves shift in the negative direction with each subsequent cycle due to the oxidation of the Si surface, which adversely affects the surface reaction rate.

this time, the tunable light source is set to output 300 nm light. The shutter is then opened and the current changes due to the generation of photocurrent. After 10-20 seconds, the shutter is closed again, causing the added current to disappear. This process is repeated at for a given number of wavelengths up to 900 nm. This is more time consuming than measuring the current at various wavelengths and then performing a single dark measurement, but it is a far more trustworthy method because the dark current can change rather significantly over time. By measuring the dark current before and after each wavelength, there is great certainty that the baseline (dark) current is correct for each wavelength. Figure 3.8 shows a small excerpt from this kind of measurement and the corresponding data analysis steps.

CA measurements can also be performed in parallel with an analytical method like gas chromatography (GC) or mass spectrometry (MS) to confirm that the generated current results in only evolved hydrogen. Using an air-tight photoelectrochemical cell with Ar bubbling into the electrolyte instead of H_2, the gaseous products are fed to the GC or MS to quantify the rate of hydrogen production. Si-based HER systems have been shown to use nearly 100% of the generated current for H_2 evolution.[11,13] In these types of systems, the most common observable side reaction is oxygen reduction. Adequate H_2 (or Ar) bubbling in these systems limits the rate of this undesired reaction by minimizing the concentration of O_2 in the electrolyte. In this dissertation, all current is assumed to result in evolved hydrogen.

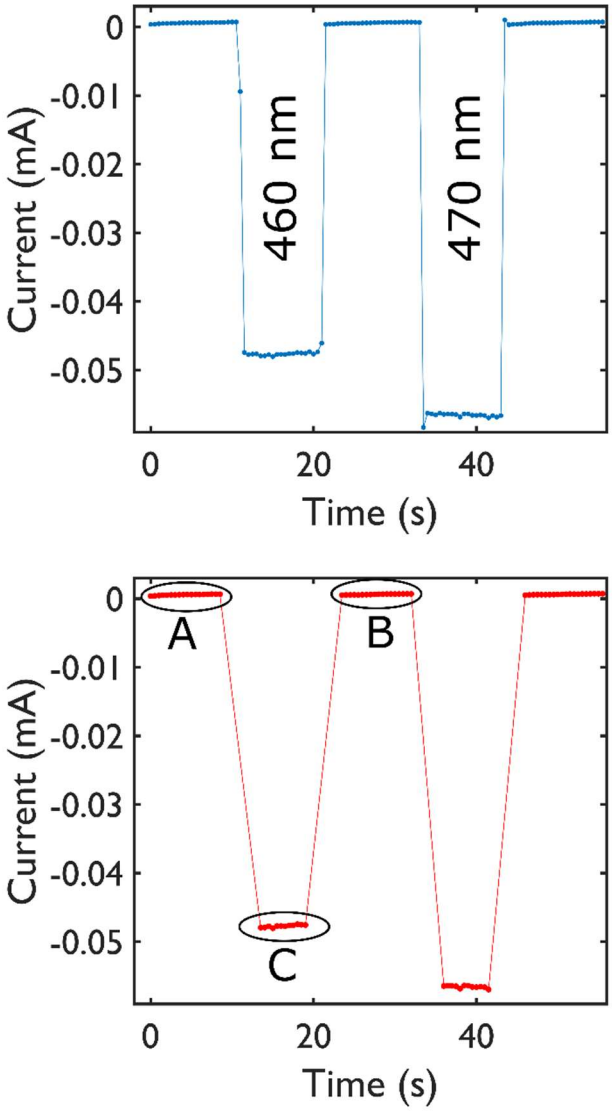

$$Photocurrent = \frac{(A+B)}{2} - C$$

Figure 3.8: Wavelength-dependent photocurrent measurements and calculations (Top) Raw CA data for a Si electrode under 460 and 470 nm light. (Middle) The data points near the transitions from light to dark are removed. *A*, *B*, and *C* designate the dark current before the 460 nm illumination, the dark current after the 460 nm illumination, and the current during 460 nm illumination, respectively. (Bottom) The photocurrent at 460 nm is the difference between the 460 nm current and the average of the before and after dark currents. This is manipulation is done at all wavelengths.

3.7 Optical Calculations

It is useful to use calculations to predict the optical properties of nanostructured materials to identify potentially beneficial geometries and to help explain various experimental results for photoelectrochemical devices. In this dissertation, these calculations were used to predict the absorptance in Si and Pt due to the effects of different geometric configurations. The codes used for these calculations are described in Appendix B. Results for these kinds of calculations are discussed in Chapter 5.

3.7.1 Finite-Difference Time-Domain Method

These optical calculations were primarily performed through the finite-difference time-domain (FDTD) method. This method solves the discretized forms of Maxwell's equations over time in a geometric mesh that is dictated by the system structure, properties, and boundary conditions. The MIT Electromagnetic Equation Propagation (MEEP)[14] software package was used for these calculations, which were performed on an in-house high-performance computing cluster. Two and three dimensional structures were investigated, with the optical properties of the component materials specified through the Drude-Lorentz model (Subsections 3.7.2 and 3.7.3). The components of the simulation space are shown in Figure 3.9.

The Si/Pt/Air system is bounded and overlapped by a perfectly matched layer (PML). The PML exists to prevent any outgoing photon flux from reflecting back into the simulation geometry, which would result in non-physical results. The light source plane extends across the entire cell and propagates electromagnetic waves in both directions. In this work, the source is a Gaussian pulse that changes intensity over time and contains a specified range of frequencies. This approach is efficient because a single calculation can

be used to get information for a range of wavelengths, instead of one wavelength per calculation which is more computationally expensive. The approach used here performs Fourier-transforms on the information collected at the flux monitors to get frequency (i.e., wavelength) information from the time-domain. In some cases, periodic boundary conditions are desired on the side boundaries of the system to look at ordered, periodic structures. This is approach is not used in this work because the experimental structures are not periodic.

Each set of calculations consists of three individual simulations. The first simulation is performed with no absorbing materials in the simulation space; only the non-absorbing background material is specified. This is set through the dielectric constant for the background, which is roughly 1 for air (Water can be used, and its dielectric constant is 1.77.). Since there is no attenuation of the light in the simulation, the flux of the isolated light source is calculated by a flux monitor (Segment *FE* in Figure 3.9). The fluxes at all other monitors are saved and fed to the next simulation which incorporates the absorbing materials (Si and Pt). The background fluxes are then subtracted from the fluxes measured at the same monitors with the absorbing materials present. These fluxes correspond to the transmission, scattering, or reflectance of light off of the different structures. The final simulation calculates the absorptance in each material by calculating the net flux of light into the material.

In this particular use of MEEP, the Si slabs are intended to be optically opaque like the Si wafers used in experiments. It is possible to build a simulation that has a 500 micron thick Si slab, but the computation process would not be feasible. Instead, the transmission

of light through the system is considered to be absorption by the Si slab. This provides an efficient way to model a very thick slab.

Since these are finite-difference calculations, there is a finite spacing between computational points in the system; this is called the mesh size. If the mesh size is too large, the simulation results are generally inaccurate. If the mesh is too fine, the calculation time becomes impractical. The goal is to set a mesh spacing where the accuracy would not significantly improve by making the mesh finer. In most 2D systems, this is usually not an issue, and small (around 0.5 nm) mesh sizes can be used with a calculation time of about 4 hours. For the 3D systems investigated in this work, mesh sizes of 2.5 nm were used, but this caused the simulations to run for about 2 weeks. Because of this, rigorous convergence tests were not feasible, but it is expected that the accuracy achieved is acceptable.

Other factors that influence the computation time include the number of wavelengths being collected, the time step size (Courant factor), and whether the electric field information is being saved. The electric fields are typically only useful when information about the spatial electric field effects is desired, such as when a plasmonic nanoparticle is being simulated.

3.7.2 Drude-Lorentz Model

The only means of incorporating the wavelength-dependent optical properties of materials into MEEP is through fitting their dielectric functions to the Drude-Lorentz (DL) model (Equation 3.3). The first term of the model is the dielectric constant at infinite frequency (ε_∞). The Drude component (second term) of this model has been traditionally used to model the dielectric function of free electrons on a metal, which are responsible

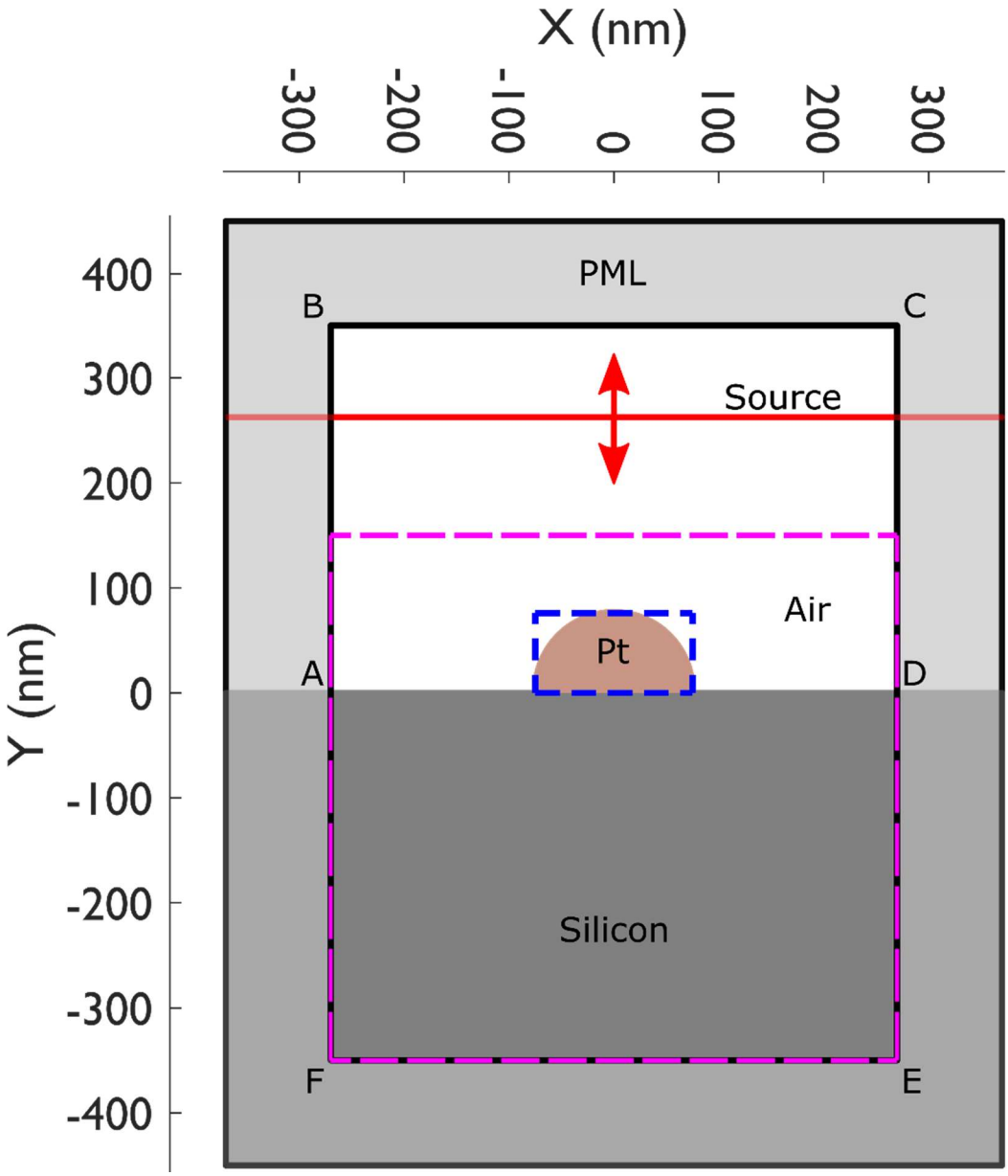

Figure 3.9: Schematic of a MEEP calculation for a slab of Si with a 150 nm diameter Pt hemisphere on the surface. The light source is designated by the red line. The Si slab occupies the entire bottom half of the cell, and overlaps with the PML domain, which is the shaded region outside of the rectangle *BCEF*. The top half of the cell that is not occupied by Pt is defined as air. The flux monitors drawn in blue and magenta are used to calculate the absorptance in the Pt and the total system, respectively. The line segment *ABCD* represents a flux monitor to calculate the system reflectance, and the segment *AFED* represents a flux monitor to calculate the "transmitted" light.

for intraband effects like plasmon resonance. The Lorentz component (third term) is used to determine the dielectric function of bound electrons in metals, which can be excited through interband transitions from the d to sp bands.[15–17] The summations indicate that multiple Drude and Lorentz contributions can be used. The ω_D and ω_L parameters specify the frequency of an electronic transition, the σ_D and σ_L parameters specify the relative strength of the associated transition, and the Γ_D and Γ_L parameters specify the damping rate for the Drude and Lorentz terms, respectively.[15,18] In this application of the model, the physical meanings of the model parameters are irrelevant; the model is used simply to fit data to an equation that MEEP understands.

3.3 $$\epsilon(\omega) = \epsilon_\infty + \sum_n \frac{\sigma_{D_n}\omega_{D_n}^2}{-i\Gamma_{D_n}\omega-\omega^2} + \sum_k \frac{\sigma_{L_k}\omega_{L_k}^2}{\omega_{L_k}^2-i\Gamma_{L_k}\omega-\omega^2}$$

3.7.3 Fitting Optical Data to Drude-Lorentz

Generating an optimum fit is vital for calculations to be physically relevant. While a perfect fit of the optical data is ideal, and could be achieved by using an infinite number of Drude and Lorentz terms, this is not practical and slows down the calculation speed. Therefore, it is important to obtain an adequate fit while minimizing the number of terms used. This was done using a MATLAB code that is discussed in more detail in Appendix B. The results of these fits are shown in Table 3.1. Silicon has a very complicated dielectric function, and the DL model is not well-suited for this material. To generate an adequate representation of Si over the range of desired wavelengths, simulations for Si are split over three different wavelength ranges and the results are merged.

Table 3.1: Drude-Lorentz parameters for silicon, platinum, and silver. The ω and Γ parameters are in units of eV. The σ parameters are unitless.

Si	Wavelengths: 300-350 nm		
k	σ_{L_k}	ω_{L_k}	Γ_{L_k}
1	0.993	3.449	0.297
2	6.359	3.791	1.083
3	4.363	4.285	0.564
ϵ_∞	5.023		

Si	Wavelengths: 350-370 nm		
k	σ_{L_k}	ω_{L_k}	Γ_{L_k}
1	0.856	3.372	0.153
2	0.847	3.462	0.169
3	2.461	3.657	0.214
ϵ_∞	15.367		

Si	Wavelengths: 370-900 nm		
k	σ_{L_k}	ω_{L_k}	Γ_{L_k}
1	1.904	3.397	0.185
2	6.314	3.887	0.027
ϵ_∞	3.675		

Pt	Wavelengths: 207-900 nm					
k	σ_{L_k}	ω_{L_k}	Γ_{L_k}	n	σ_{D_n}	ω_{D_n}	Γ_{D_n}
1	26.503	2.748	9.048	1	2.772	5.418	0.994
2	1.805	10.379	2.643				
ϵ_∞	1.081						

Ag	Wavelengths: 300-900 nm					
k	σ_{L_k}	ω_{L_k}	Γ_{L_k}	n	σ_{D_n}	ω_{D_n}	Γ_{D_n}
1	0.475	4.335	0.279	1	3.632	4.836	0.012
2	0.135	2.190	0.967				
ϵ_∞	3.405						

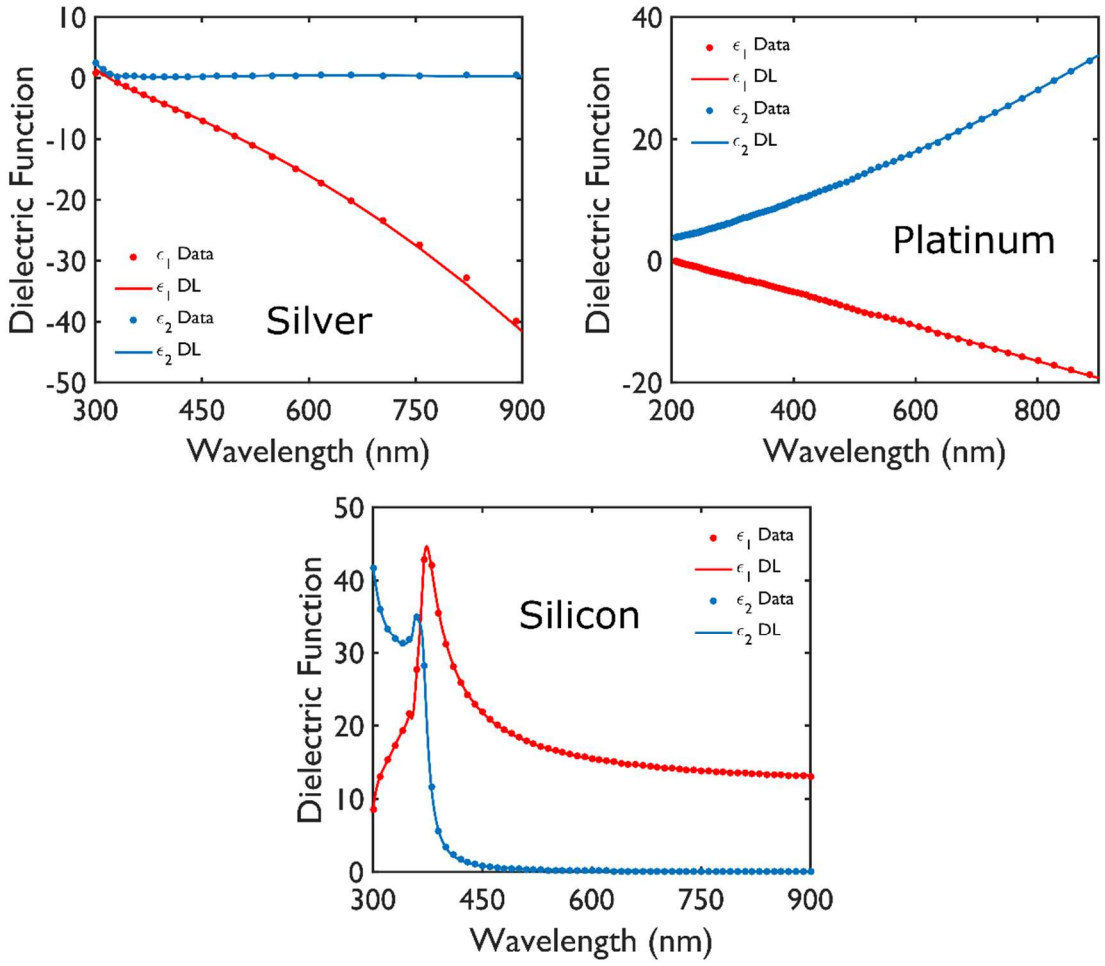

Figure 3.10: Experimental dielectric function data[19,20] for silver, platinum, and silicon and the corresponding DL models based on the parameters in Table 3.1.

3.8 Semiconductor Calculations

A component of this dissertation work is focused on the properties of the interfaces between the semiconductor and metal or electrolyte in a PEC system and how these properties affect the performance. In particular, the aim of this work has been to engineer these interfaces so that high barrier heights are achieved, resulting in high photovoltages and consequently, high charge transfer efficiency. The Semiconductor module in COMSOL was used to explain the roles of several interfacial changes that have been observed experimentally in this work. This work is discussed in Chapter 7.

COMSOL uses the finite element method (FEM) to numerically calculate solutions to partial differential equations that represent physical processes. For semiconductors, COMSOL solves the drift-diffusion, continuity, and Poisson's equations for a given system to determine the local electron and hole concentrations, yielding information about the electric fields, potentials, and band structure. This information can be directly used to identify changes in interfacial barrier heights. A template for these calculations is stored on the Linic Group Wiki.[21]

3.8.1 Simulation Properties

In these calculations, there are several settings and parameters that must be specified. In this work, the system was modeled in a 2D space with axial symmetry. This allowed the calculation of discontinuous or continuous (i.e., particle or film, respectively) contacts to the semiconductor. COMSOL has the material properties for Si built-in, so this was chosen as the semiconductor. These built-in properties include electron and hole lifetimes and mobilities, densities of states, and the band gap. Additionally, the acceptor and donor concentrations must be specified. Finally, the boundary conditions must be set

to provide ohmic, Schottky, or semiconductor-insulator-metal contacts to establish different semiconductor/metal interfaces.

3.8.2 Schottky Barriers

A simple model for SC/metal contacts is a Schottky barrier where the barrier height established at the interface is equal to the difference in energy between the metal work function and the energy of the conduction band (for an n-type SC) or valence band (for a p-type SC). For a p-type SC, contact to a low work function metal forms a high barrier height. If the work function of the metal is high enough to make its Fermi level lower in energy than the SC Fermi energy, an ohmic contact is formed. For the specific case of Si, the electron affinity (energy difference between vacuum and the conduction band) is 4.05 eV. The valance band energy is 5.15 eV, which is the sum of the electron affinity and the band gap (1.12 eV). In the case of Pt, with a work function between 5.12 and 5.93 eV,[22] a Si/Pt film either forms a Schottky contact with a very small barrier height or an ohmic contact. This is not desirable for a PEC device, so COMSOL is used to identify the effects of using particle contacts instead of films, changing the interface geometry through embedding, and including insulation at the interface.

3.8.3 P-N Junctions

PEC devices are well-suited for borrowing the concept of p-n junctions from solar cells. Briefly, a p-type (or n-type) wafer can be doped on the reactive surface with donor (or acceptor) atoms at the SC/electrolyte interface to make a buried junction. This is useful because it removes the dependence of the barrier height in the system on the electrolyte solution potential or the metal work function. In COMSOL, this effect is investigated by introducing different donor atom concentrations and performing similar calculations to

those in the previous section. These calculations were used in particular to relate to experimental pn-Si results to identify more optimal junction depths and doping levels.

3.9 Conclusion

The previous sections in this chapter have described the experimental and computational methods routinely used to complete the work described in the subsequent chapters. The preparation of silicon electrodes and optical samples was described, as well as the PEC and optical characterization methods in which they are used. Finally, the FDTD and FEM methods used to calculate the optical and charge transport properties of these systems were explained. The following chapters will discuss the application of these methods and provide experiment-specific details.

3.10 References

(1) Lombardi, I.; Marchionna, S.; Zangari, G.; Pizzini, S. Effect of Pt Particle Size and Distribution on Photoelectrochemical Hydrogen Evolution by P-Si Photocathodes. *Langmuir* **2007**, *23* (24), 12413–12420.

(2) Brejna, P. R.; Griffiths, P. R. Electroless Deposition of Silver Onto Silicon as a Method of Preparation of Reproducible Surface-Enhanced Raman Spectroscopy Substrates and Tip-Enhanced Raman Spectroscopy Tips. *Appl. Spectrosc.* **2010**, *64* (5), 493–499.

(3) Carraro, C.; Maboudian, R.; Magagnin, L. Metallization and Nanostructuring of Semiconductor Surfaces by Galvanic Displacement Processes. *Surf. Sci. Rep.* **2007**, *62* (12), 499–525.

(4) Bard, A. J.; Faulkner, L. R. *Electrochemical Methods: Fundamentals and Applications*; Wiley, 2001.

(5) Zhang, X. G. *Electrochemistry of Silicon and Its Oxide*; Springer, 2001.

(6) Tsujino, K.; Matsumura, M. Boring Deep Cylindrical Nanoholes in Silicon Using Silver Nanoparticles as a Catalyst. *Adv. Mater.* **2005**, *17* (8), 1045–1047.

(7) Tsujino, K.; Matsumura, M. Morphology of Nanoholes Formed in Silicon by Wet Etching in Solutions Containing HF and H_2O_2 at Different Concentrations Using Silver Nanoparticles as Catalysts. *Electrochim. Acta* **2007**, *53* (1), 28–34.

(8) Huang, Y.; Sun, L.; Xie, K.; Lai, Y.; Liu, B.; Ren, B.; Lin, C. SERS Study of Ag

Nanoparticles Electrodeposited on Patterned TiO_2 Nanotube Films. *J. Raman Spectrosc.* **2011**, *42* (5), 986–991.

(9) Smith, T. J.; Stevenson, K. J. Reference Electrodes. *Polymer (Guildf).* **2007**.

(10) Chen, Y. W.; Prange, J. D.; Dühnen, S.; Park, Y.; Gunji, M.; Chidsey, C. E. D.; McIntyre, P. C. Atomic Layer-Deposited Tunnel Oxide Stabilizes Silicon Photoanodes for Water Oxidation. *Nat. Mater.* **2011**, *10* (7), 539–544.

(11) Jung, J.-Y.; Park, M.-J.; Li, X.; Kim, J.-H.; Wehrspohn, R. B.; Lee, J.-H. High Performance H_2 Evolution Realized in 20 Mm-Thin Silicon Nanostructured Photocathodes. *J. Mater. Chem. A* **2015**, *3* (18), 9456–9460.

(12) *Redox*, 1st ed.; Schüring, J., Schulz, H. D., Fischer, W. R., Böttcher, J., Duijnisveld, W. H. M., Eds.; Springer Berlin Heidelberg: Berlin, Heidelberg, 2000.

(13) Hou, Y.; Abrams, B.; Vesborg, P. Bioinspired Molecular Co-Catalysts Bonded to a Silicon Photocathode for Solar Hydrogen Evolution. *Nat. Mater.* **2011**, *10* (6), 434–438.

(14) Oskooi, A. F.; Roundy, D.; Ibanescu, M.; Bermel, P.; Joannopoulos, J. D.; Johnson, S. G. Meep: A Flexible Free-Software Package for Electromagnetic Simulations by the FDTD Method. *Comput. Phys. Commun.* **2010**, *181* (3), 687–702.

(15) Kreibig, U.; Vollmer, M. *Optical Properties of Metal Clusters*; Springer Series in Materials Science; Springer Berlin Heidelberg: Berlin, Heidelberg, 1995; Vol. 118.

(16) Lei, D. Y.; Fernández-Domínguez, A. I.; Sonnefraud, Y.; Appavoo, K.; Haglund, R. F.; Pendry, J. B.; Maier, S. A. Revealing Plasmonic Gap Modes in Particle-on-Film Systems Using Dark-Field Spectroscopy. *ACS Nano* **2012**, *6* (2), 1380–1386.

(17) Maier, S. A. *Plasmonics: Fundamentals and Applications*; Springer, 2007.

(18) McMahon, J. M.; Schatz, G. C.; Gray, S. K. Plasmonics in the Ultraviolet with the Poor Metals Al, Ga, In, Sn, Tl, Pb, and Bi. *Phys. Chem. Chem. Phys.* **2013**.

(19) Green, M. A.; Keevers, M. J. Optical Properties of Intrinsic Silicon at 300 K. *Prog. Photovoltaics Res. Appl.* **1995**, *3* (3), 189–192.

(20) Lynch, D. W.; Hunter, W. R. Comments on the Optical Constants of Metals and an Introduction to the Data for Several Metals. In *Handbook of Optical Constants of Solids*; Palik, E., Ed.; Academic Press, 1997; pp 275–367.

(21) Hernley, P. Linic Group Wiki: Hernley Dissertation Files http://linicgroup.engin.umich.edu/wiki/doku.php?id=paul_dissertation:start.

(22) Musumeci, F.; Pollack, G. H. Influence of Water on the Work Function of Certain Metals. *Chem. Phys. Lett.* **2012**, *536*, 65–67.

CHAPTER 4

Modeling Photoelectrochemical Processes

4.1 Summary

The development of simple mathematical models to describe complex systems is a beneficial exercise to identify the parameters that are most important for optimizing a process. This chapter describes efforts to identify the key parameters governing photoelectrochemical systems. The Absorption/Recombination model identifies the changes in photocurrent upon incorporating optically active metal nanoparticles into semiconductor photoelectrodes as a result of localized surface plasmon resonance, parasitic absorption, and bulk recombination effects. The Diode/Butler-Volmer model focuses on the relationships of applied potential, photocurrent, SC interface quality, and surface activity with the resulting current/reaction rate. The codes for the Absorption/Recombination model and the Diode/Butler-Volmer model can be found in Appendices C and D, respectively.

4.2 Absorption/Recombination Model

Localized surface plasmon resonance (LSPR) has been used to improve the rate of generation of charge carriers that are able to reach the reactive surface in several PEC systems. Ingram and Linic show that Ag nanocubes can significantly improve the light-limited photocurrent generated by a nitrogen-doped TiO_2 (N-TiO_2) oxygen evolution reaction (OER) photoanode by selectively absorbing photons near the SC/electrolyte

interface instead of deep in the SC. This strategy reduces the rate of bulk recombination, which is a rate limiting process in the bare N-TiO_2 system.[1] Research by Thomann et al. extended this strategy to hematite (Fe_2O_3) with gold nanoparticles.[2] This work focused on investigating how engineering the nanostructure involving a plasmonic nanoparticle and SC can be used to optimize the benefits from LSPR-induced effects. Both of these efforts explored the impact of the LSPR near-field effect on the rate of generation of useful charge carriers for wavelengths of light that have photon absorption depths that are significantly longer than the minority charge carrier diffusion length. Pillai et al. and Temple et al. incorporated Ag nanoparticles on the surface of Si solar cells and demonstrated an enhancement of the photocurrent for wavelengths of light that are poorly absorbed and highly reflected by the solar cells used, respectively.[3,4] The enhancements observed were suggested to be caused by increased forward scattering of light into the Si by the Ag particles, essentially acting as an anti-reflective coating. In all of these efforts, the enhancements have been observed in conditions where the SC is inefficient at transporting charge carriers to the reactive surface or is a poor absorber of photons. Das et al., Matheu et al., and Akimov et al. have determined that incorporating metal nanoparticles on the surface of a solar cell is inherently lossy due to parasitic absorption and that dielectric nanoparticles that are effectively non-absorbing (e.g. SiO_2) can be used to achieve higher photocurrents instead.[5–7]

There remains much to be explained in this field regarding the use of metallic nanoparticles to improve the harvesting of light by SC devices. The common theme is that enhancements stated above are only observed for conditions that are using inefficient systems. A more useful question to answer is whether plasmonic particles can be used to

improve systems that already achieve more practical efficiencies at wavelengths of light, like the UV-visible regime, where a large portion of the useful photons in sunlight exist potentially have enough energy to split water.

To answer this question, we have developed a model that considers the optical properties of a SC, its bulk recombination processes, and the potential effects resulting from the incorporation of different hypothetical metal nanoparticles into the SC. From this model, the absorptance in the SC and the external quantum efficiency (EQE) are calculated, which give direct insight into the potential role of metal nanoparticles. Figure 4.1 provides a sketch of the model system.

4.2.1 Framework of the Model

A planar SC slab with a particular complex refractive index, thickness (L), and minority charge carrier diffusion length (r) is specified. The real component of the complex dielectric is used to calculate the reflectivity (R) of the SC assuming a background refractive index of 1 or 1.33 to represent air or water, respectively, based on the Fresnel equation at normal incidence (Equation 2.7). The absorption coefficient of the SC is calculated at each wavelength using the complex component of the refractive index, the extinction coefficient (Equation 2.8). The inverse of the absorption coefficient is then defined as the photon penetration depth (d[λ]). This parameter is a measure of how well a material absorbs light and is defined as the distance at which the fraction of light absorbed is (1 - 1/e), or about 63.2%. The probability of absorption (A) at a given wavelength (λ) and depth in the SC (x) is defined using a modified form of Beer's Law, as shown in Equation 4.1.

4.1 $$A(\lambda, x) = 1 - \exp[-x/d(\lambda)\,]$$

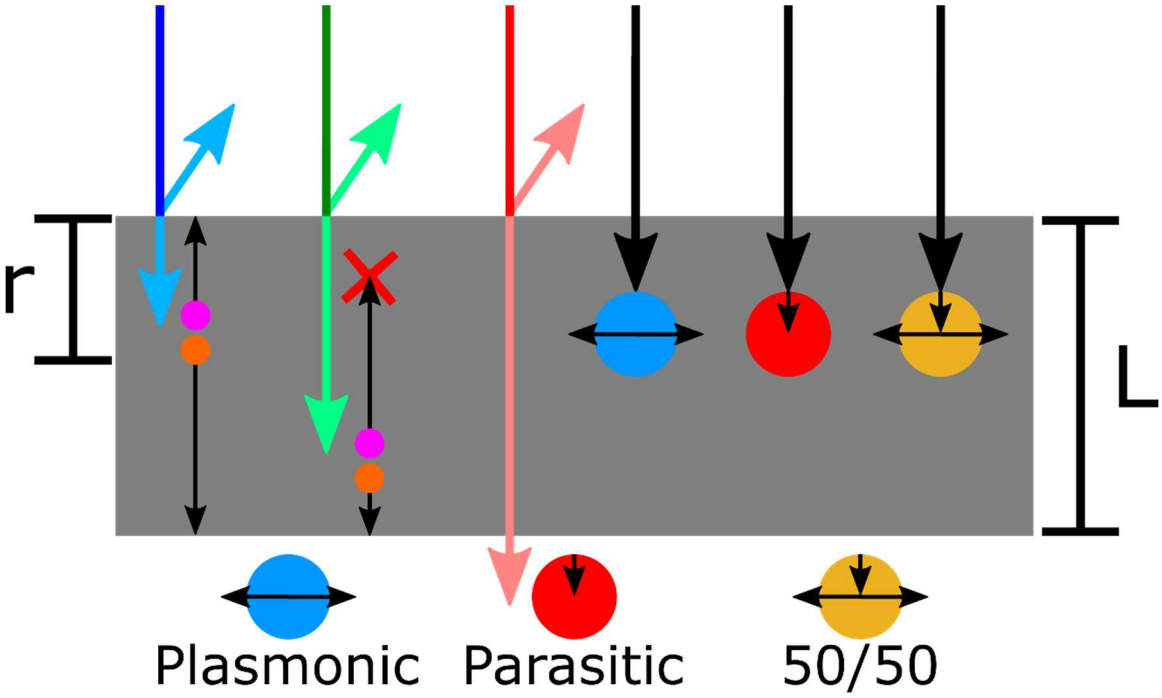

Figure 4.1: Absorption/Recombination model diagram. A SC slab of thickness *L* has a minority charge carrier diffusion length *r* and optical properties that specify how reflective it is and the penetration depths of different wavelengths of light. Three different hypothetical metals are added to the system to observe changes in the absorption in the SC and external quantum efficiency.

The rate of bulk recombination, which was discussed in Chapter 2, can be represented by the minority charge carrier diffusion length, with the probability of bulk recombination (BR) at a given depth in the SC defined by Equation 4.2.

4.2 $$BR(x) = 1 - \exp[-x/r\,]$$

This equation takes the same form as the modified Beer-Lambert equation. The Beer-Lambert equation describes the likelihood of a photon interacting with a material after traveling a certain distance in the material. For this recombination equation, we are interested in knowing the likelihood of a minority charge carrier interacting with a majority charge carrier after traveling a certain distance. Since the same physical concept is being quantified (probability of an object interacting with another object), it should be reasonable to quantify the recombination probability in this way.

The result from Equation 4.1 represents the cumulative probability of absorption between $x = 0$ μm and $x = L$ μm. To identify the incremental probability of absorption at a specific depth, the depth domain is discretized such that there are 32,238 elements to ensure adequate convergence. The depth function (D) is defined by the piecewise function in Equation 4.3.

4.3 $$D(\sigma = \{1, 2, 3, \dots, 32238\}) = \begin{cases} 0\,, & \sigma = 1 \\ \frac{L}{10^7} \cdot e^{[5 \cdot 10^{-4}(\sigma - 1)]}, & 2 \leq \sigma \leq 32237 \\ L\,, & \sigma = 32238 \end{cases}$$

The parameter σ designates the node number, with $\sigma = 1$ located at the illuminated side of the SC ($x = 0$) and $\sigma = 32238$ located at the back of the SC ($x = L$). The absorption probability at each wavelength in each element of the grid defined by the above equation is then calculated using Equation 4.4.

4.4 $$A'\big(\lambda, D(\sigma > 1)\big) = A\big(\lambda, D(\sigma)\big) - A\big(\lambda, D(\sigma - 1)\big)$$

The absorptance by the entire SC slab at given wavelength is equal to the product of the cumulative absorption probability at $x = L$ and the fraction of incident light that is not reflected.

4.5 $$\overline{A}(\lambda, L) = A(\lambda, L)\big(1 - R(\lambda)\big)$$

The charge collection probability at a specific grid element (C') is calculated as the product of the probability of absorption at a specific element and the probability of a charge carrier successfully reaching the front side of the SC. This is shown in Equation 4.6. The method of calculating the incremental absorption probability using backward differences means $C'(\lambda, D(\sigma = 1)) = 0$. The sum of the incremental charge collection probabilities for the entire SC slab is equal to the cumulative charge collection probability for the slab (Equation 4.7).

4.6 $$C'\big(\lambda, D(\sigma)\big) = A'\big(\lambda, D(\sigma)\big)\big[1 - BR\big(D(\sigma)\big)\big]$$

4.7 $$C(\lambda, L) = \sum_{\sigma=1}^{32238} C'\big(\lambda, D(\sigma)\big)$$

Multiplying this cumulative charge collection probability by the fraction of photons not reflected by the SC surface at each wavelength gives the external quantum efficiency (EQE) for this hypothetical system (Equation 4.8).

4.8 $$EQE(\lambda, L) = C(\lambda, L)\big(1 - R(\lambda)\big)$$

The EQE is the rate of reaction of the photo-generated charge carriers at the SC surface (directly related to photocurrent) divided by the rate of photons illuminating the surface. In this model, the expectation is that there are no kinetic limitations or losses due to majority charge carriers crossing into the electrolyte. This model is intended to mimic the behavior of SC photoelectrodes that are operating in the light-limited photocurrent

regime. Because of this, the EQE value could be multiplied by a rate of photon flux to predict the photocurrent density for a particular system.

The effects of three types of hypothetical metal nanoparticles can be incorporated into this calculation. They are named *plasmonic*, *parasitic*, and *50-50*. In the case of the plasmonic particle, the idea is to provide a metal that can interact with the light at a certain depth in the SC and inject all of the energy into the SC at that depth. This is an idealized case because it assumes a plasmonic particle can dissipate all of its energy through the localized field enhancement effect described in Chapter 2, which is not representative of a physical system. In reality, a significant portion of the energy is dissipated by heating the particle through absorption and scattering light away from the particle. The parasitic case represents a metal nanoparticle that dissipates all of the incoming photon energy as heat, which is not useful for improving the SC photocurrent. The 50-50 case takes half of the energy from light and injects it into the SC while the other half is dissipated as heat. This is expected to be more representative of a realistic metal nanoparticle, but it likely provides an overestimate of the metal's ability to give energy to the SC.

To implement these metals, the particle depth (p) is specified. The grid element number that most closely matches this depth is then designated as the particle grid element (σ_p) to be used in the calculation. For the plasmonic particle, the cumulative absorption at that designated depth (and all depths below it) is then set to 1 (Equation 4.9). In the case of the parasitic particle, the cumulative absorption in the SC is unchanged from the previous grid element because the dissipation of the energy as heat by the particle prevented any additional absorption in the SC. This condition is described mathematically in Equation 4.10.

4.9 $$A\left(\lambda, D\left(\sigma \geq \sigma_p\right)\right) = 1$$

4.10 $$A\left(\lambda, D\left(\sigma \geq \sigma_p\right)\right) = A\left(\lambda, D\left(\sigma = \sigma_p - 1\right)\right)$$

For the 50-50 particle, the cumulative absorption in the SC at the particle depth, and beyond, is shown as Equation 4.11 and is set to be the average of the two limiting cases shown above. Figure 4.2 shows how these different particles change the absorption depth and fate of photons in these calculations.

4.11 $$A\left(\lambda, D\left(\sigma \geq \sigma_p\right)\right) = \frac{\left[1 + A\left(\lambda, D\left(\sigma = \sigma_p - 1\right)\right)\right]}{2}$$

For these calculations, the particles are assumed to interact with all light that reaches that depth in the SC slab. This means there is no transmission of light beyond the particle depth in the slab. In a future implementation of this model, a parameter to increase the amount light that passes through the metal to be absorbed deeper in the SC could be added. Additionally, the metals are set to have the aforementioned optical properties at all wavelengths. This isn't necessarily an assumption but rather a data presentation preference to be able to adequately demonstrate the effects of these metals at all wavelengths. The model could be easily changed to use wavelength-dependent optical properties for the metals.

Through these manipulations of the absorption calculations, the intended effects on the absorption are implemented and the rest of the calculations are carried through as described above. This approach makes it possible to see how the absorption in the entire SC slab is changed by the particles and how the absorption of photons at specific depths results in changes in the EQE.

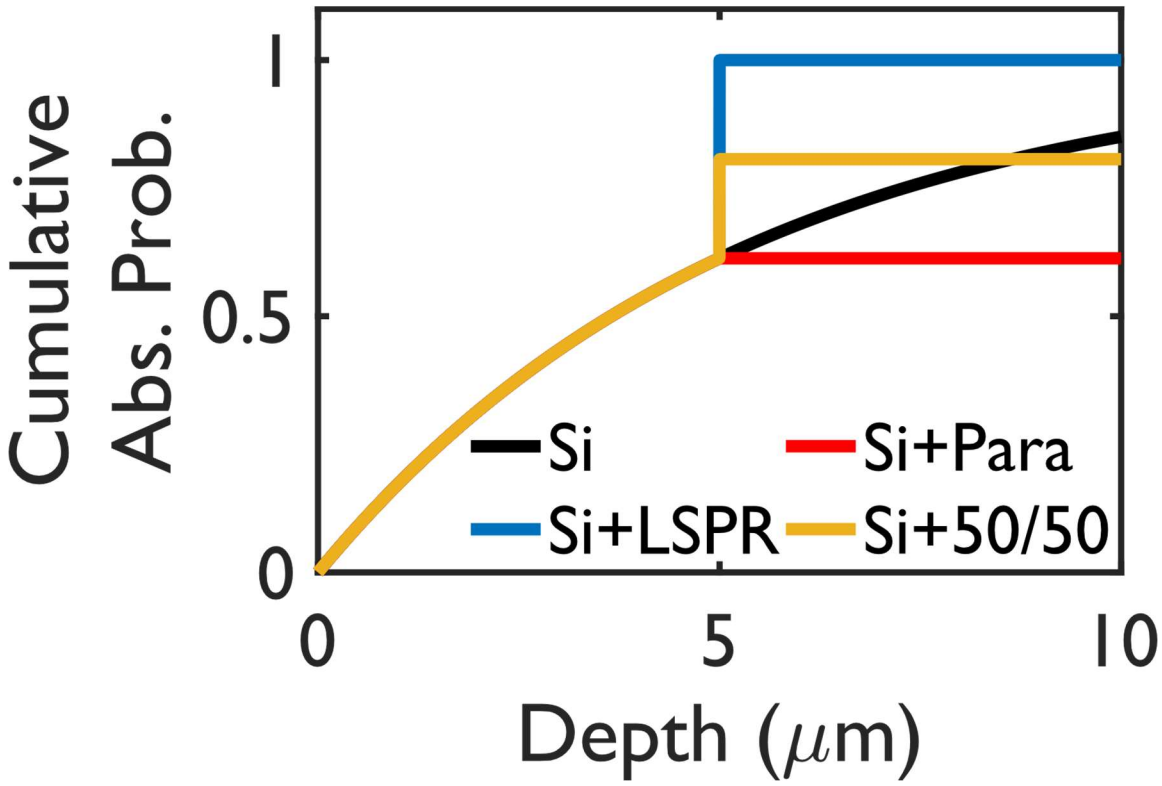

Figure 4.2: Calculated cumulative probability of absorption in the SC under 700 nm illumination for 10 μm thick bare Si and with metals at a depth of 5 μm. At this depth, the plasmonic (LSPR) particle increases the probability to 100%, meaning all remaining photons are absorbed at that point. The parasitic (Para) particle allows no additional absorption beyond the particle depth. The 50/50 particle increases the absorption at this point to the average of the plasmonic and parasitic cases. At a depth of 10 μm, the bare Si has a higher probability of absorption than the 50/50 particle.

4.2.2 Results and Discussion

The purpose of this work is to determine if it is practical to try to use LSPR to enhance the photocurrents for different SC materials. Three different SCs were used for this analysis: rutile TiO_2 (r-TiO_2), Si, and $BiVO_4$. Table 4.1 lists the relevant properties for of these SCs. The optical properties and diffusion lengths for these materials were gathered from various sources.[8–12] TiO_2 has been demonstrated to be able to greatly benefit from the near-field electric field enhancements induced by LSPR on Ag nanoparticles.[1,13] Silicon, due to its indirect band gap, has a much longer charge carrier diffusion length than TiO_2, so bulk recombination is less prominent. $BiVO_4$ is included because it has an intermediate band gap energy and diffusion length, and has also been the focus of recent research that shows it has the potential to be an efficient PEC material.[9,14]

Table 4.1: Properties of the modeled semiconductors

Semiconductor	Band Gap (eV)	Band Gap Type	Diffusion Length
r-TiO_2	3.0	Direct	10 nm
Si	1.12	Indirect	100 μm
$BiVO_4$	2.4	Direct	100 nm

The first set of calculations positioned the metal nanoparticles so that they are one diffusion length away from the front surface and used a slab thickness of 500 μm. Figure 4.3 shows these results for each SC. The wavelength ranges were chosen to only consider parts of the light spectrum that the SC is able to absorb (i.e. sub-band gap wavelengths are ignored). One common theme for all SCs is that at a depth of one diffusion length, the presence of LSPR particles has no effect on improving the absorptance by the SC. This is because the slabs are all sufficiently thick to absorb all the light that is not initially reflected at the surface. The particles with a full parasitic effect (Para) or a 50% parasitic effect

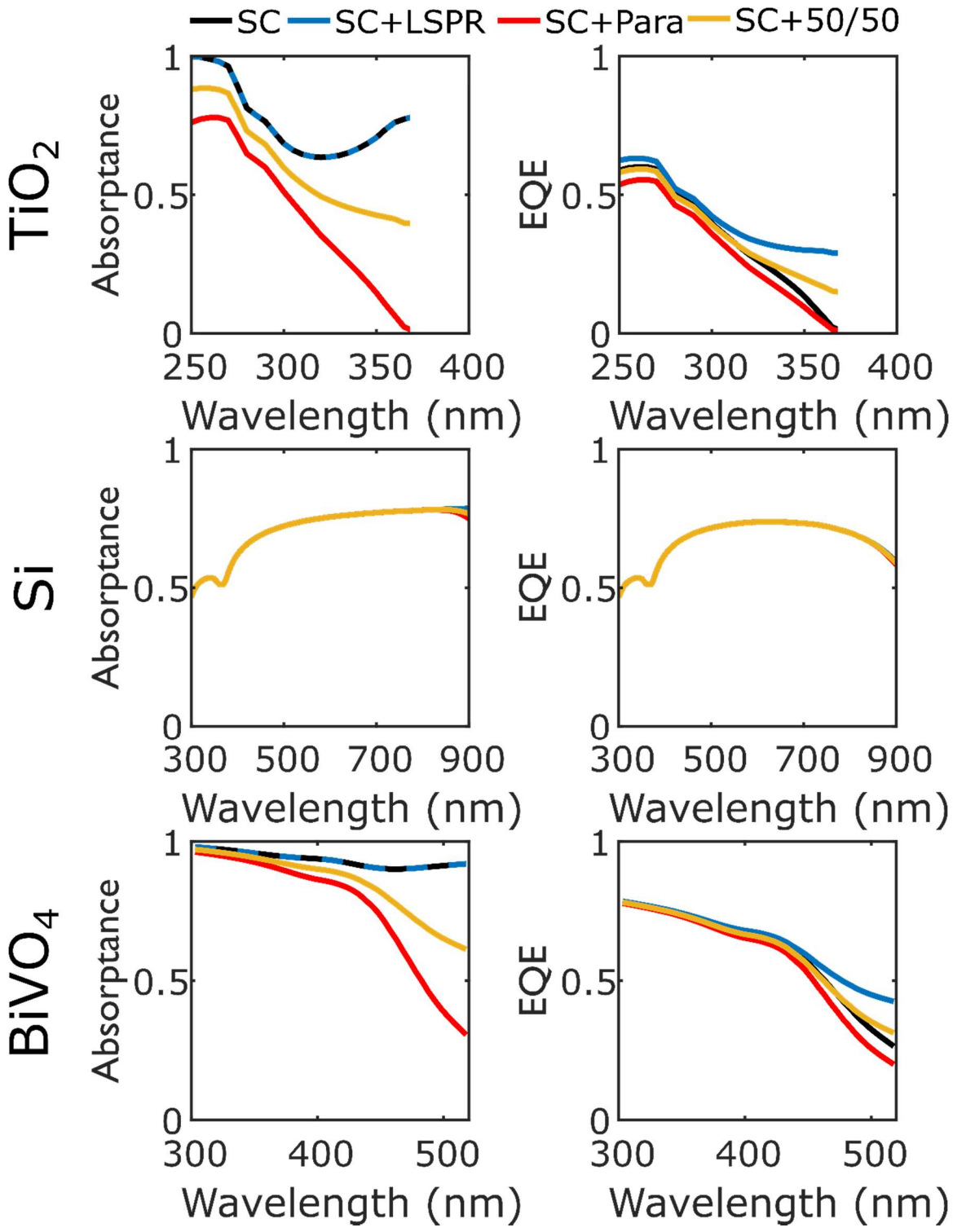

Figure 4.3: Calculated absorptance and efficiency for TiO_2, Si, and $BiVO_4$ in water. The metal particles were placed one diffusion length away from the illuminated surface in each case.

(50/50) only make the absorptance in the entire slab worse than the bare SC. The EQE results are different because the location within the SC where the photon is absorbed is considered in combination with the diffusion length of the SC. In the case of TiO_2 and $BiVO_4$, the short charge carrier diffusion lengths limit the bare SC efficiency, especially at wavelengths approaching the band gap. In general, even the 50/50 particle is able to demonstrate an efficiency enhancement at these wavelengths, overcoming the significant parasitic absorption losses observed in the absorptance plots. The parasitic particle hinders the efficiency at all wavelengths, but only marginally. In Si, there is virtually no effect because most photons between 300 and 900 nm are absorbed within one diffusion length (100 μm) from the surface.

The thickness of the Si and the depth of the metal particles have a strong effect on the efficiency. Calculation results for two Si thicknesses (L = 500 μm and 100 nm). And two particle depths (p =100 nm and 10 nm) are shown as the Si result in Figure 4.3 and all of Figure 4.4. When the slab is as thick as a standard Si wafer (500 μm), the plasmonic particle accomplishes almost nothing at a depth of 100 μm. At a depth of 10 nm, there is a small improvement of the EQE at long wavelengths. This is due to the bulk recombination of charge carriers that are absorbed deep within the Si without the plasmonic particles. The existence of any parasitic effect (Para or 50/50), is extremely detrimental to the absorptance in the Si, directly causing a loss of efficiency.

When the Si is 100 nm thick and the particles are put at a depth of 100 nm, the plasmonic particle is essentially acting as a perfect back reflector. With the parasitic particle, the system is identical to the bare Si slab, because the particle does not interact with any potentially useful light. At a depth of 10 nm, the plasmonic and 50/50 particles

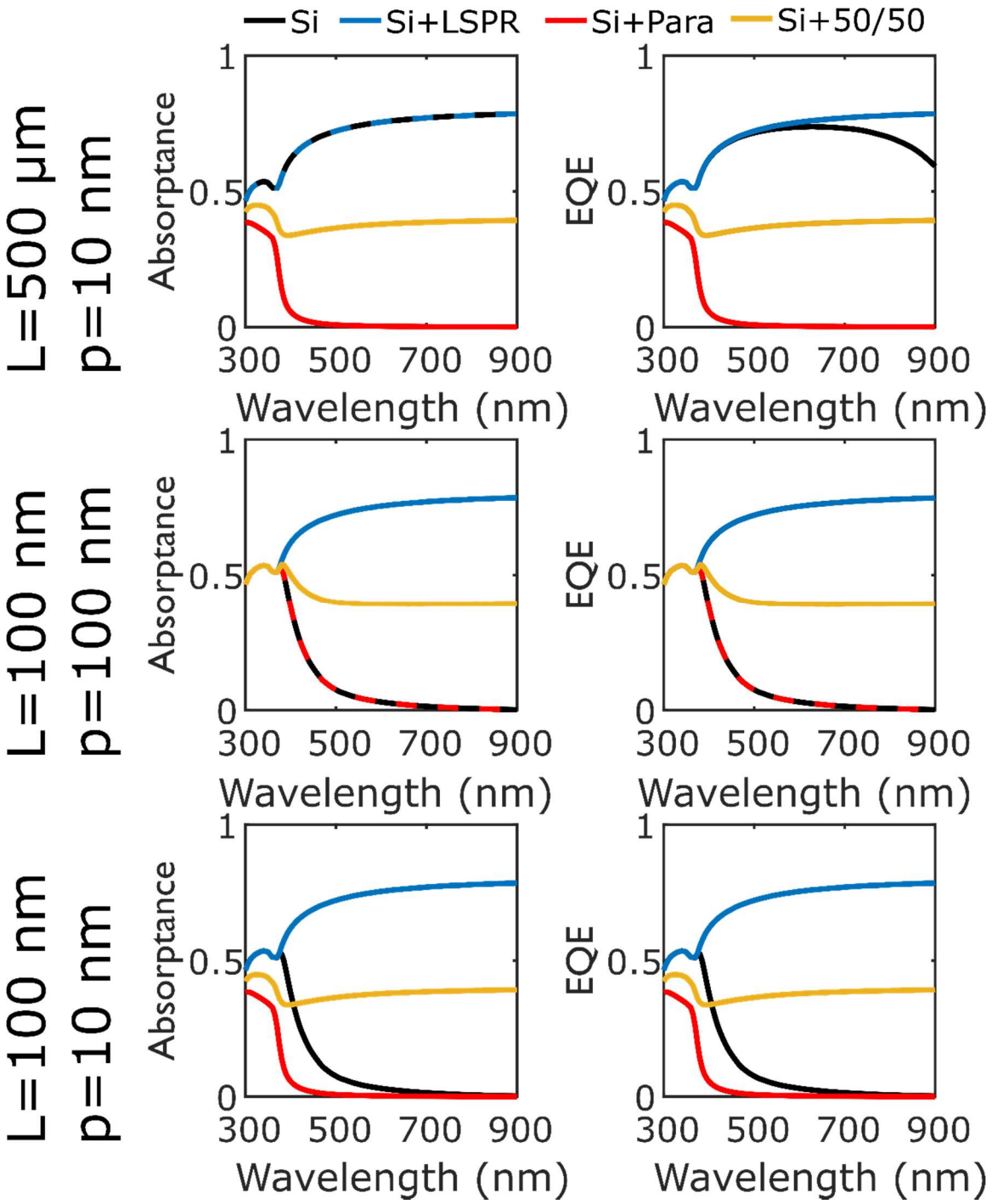

Figure 4.4: Calculated absorptance and efficiency for different Si thicknesses (*L*) and particle depths (*p*). The background material is water.

show strong enhancements for long wavelengths due to the poor optical properties of ultrathin Si at these wavelengths. At short wavelengths, the 50/50 particle is detrimental to the efficiency. The parasitic particle always causes a significant loss.

It is vital to recognize that the hypothetical plasmonic particle used in these calculations is entirely non-physical. There will always be significant parasitic losses because plasmonic particles have large absorption cross-sections. With this is mind, the 50/50 particle should be considered to be a more physical representation of a real plasmonic effect. Using this particle as a guide, the model clearly confirms the hypothesis that LSPR can only be used to improve inefficient systems. When the charge carrier diffusion length is short relative to the photon penetration depth, LSPR can be used to reduce recombination, as with TiO_2 and $BiVO_4$. If bulk recombination is not problematic, but the SC slab is too thin to absorb much light, LSPR can be used to increase the absorptance for poorly absorbed wavelengths, but likely at the expense of causing parasitic absorption at wavelengths that have shorter photon penetration depths. In these very thin systems, a better approach is to focus on making efficient back reflectors instead of embedded nanoparticles because this eliminates any parasitic loss and still has a potential to provide significant enhancements.

The only way to improve a good SC system like thick Si is to address its main shortcoming: reflectance. When the Si slab is in water, its reflectance is reduced relative to air, but still shows a 20% loss due to reflectance, at a minimum. The reflectance of the Si in the model was reduced to 50% and 10% of its original values (Figure 4.5). The associated EQE enhancements are far greater than any observed in the model for 500 μm thick Si using plasmonic particles. The experimental data plotted in the top left panel of Figure 4.5

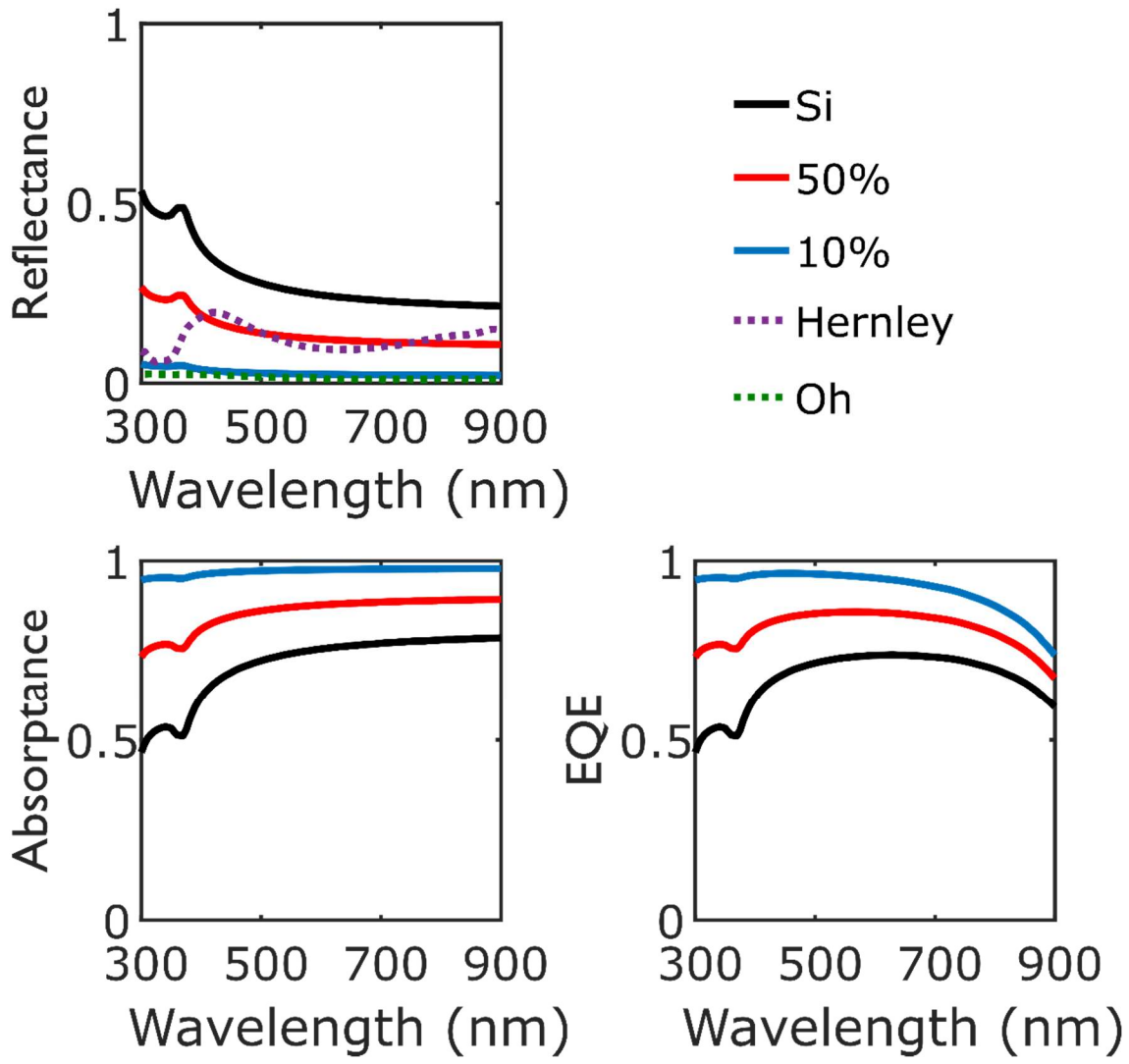

Figure 4.5: Effect of reflectance on Si Absorptance and EQE (Top Left) Calculated reflectance spectra of Si in water (black), Si with only 50% of its original reflectance (red), and Si with 10% of its original reflectance (blue). The dashed curves are from experiments for Pt embedded into Si from Chapter 5 (purple) and Oh's nanoporous black Si surface.[15] (Bottom Left) The calculated absorptance values for the different reflectance settings. (Bottom Right): EQE values for the systems with varied reflectance.

show that it is possible to achieve these kinds of reflectance reductions. Chapter 5 addresses the experimental aspect of addressing this problem while also reducing the parasitic absorption effect associated with incorporating metal co-catalyst particles on the Si surface.

4.3 Diode/Butler-Volmer Model

Chapter 2 explained the various processes involved with PEC on a SC electrode. The concepts of reflection and absorption, charge transport and recombination, and catalysis must be understood and simultaneously optimized to develop more efficient materials. The first step to understanding how all the processes affect the system is to build a conceptually transparent model of a PEC system.

This type of model has developed previously,[16,17] but these previous investigations were mostly concerned only one aspect of a PEC system. In this work, the goal is to determine which parameters need to be manipulated and determine how to alter them to improve each aspect of a PEC device. Additionally, the implementation of particulate co-catalysts instead of films is unique, but not without its own broad assumptions.

4.3.1 Framework

This model is built using a circuit analysis approach in which a photodiode is used to represent the absorption and charge transport processes within the SC, while the Butler-Volmer equation is used to describe the surface reaction rates associated with different catalytic surfaces. These components are connected in series with each other, with the ability to use different catalytic surfaces in parallel with each other. The overall structure of the model is shown in in Equation 4.12. In this equation, the reciprocal of the total system current i is equal to the sum of reciprocal of the diode current i_{Diode} and the

reciprocal of the sum of the kinetic currents for each catalytic surface i_{k_x}, where x designates the catalyst material. This structure is built upon the principle that the total current cannot exceed the current of the slowest system process.

4.12 $$\frac{1}{i} = \frac{1}{i_{Dio}} + \frac{1}{\sum_x i_{k_x}}$$

The diode current is defined using the Shockley diode equation combined with a photocurrent contribution, which is shown in Equation 4.13.

4.13 $$i_{Diode} = A\left[j_o\gamma\left(exp\left[\frac{qE}{nkT}\right] - 1\right) - j_{ph}\right]$$

The first term in this equation regulates the potential-dependent movement of charge across the SC and electrolyte/metal interface. The second term, which contains j_{ph}, specifies the rate at which minority charge carriers are generated and arrive at the space-charge layer of the SC. Therefore, the incident light intensity, optical properties, and bulk recombination rate of the system are contained in this value. In this equation, A is the projected cross-sectional area of the SC, j_o is the reverse bias saturation current density, and γ is the roughness factor for the SC/metal surface. Inside the exponential, q, k, and T are the elemental charge, Boltzmann constant, and temperature, respectively. E is the potential applied to the diode and n is the ideality factor. The ideality factor is usually between a value of 1 and 2. It is set to 1 when bulk recombination is the dominant recombination path and 2 when recombination in the space-charge layer dominates. Since bulk recombination rates in Si are low, this value is set to 2.

The reverse bias saturation current density is a measure of the current density passing through the diode under dark conditions. It is also called the leakage current because it indicates the rate at which the minority charge carriers, which have a very low

concentration in dark, leak across the interface. The rate of leakage is dependent on the characteristics of the interface, which are defined using Equation 4.14.

4.14 $$j_o = A^* T^2 \exp[-q\varphi_B / kT]$$

In this equation, the main parameter of interest is φ_B, which is the barrier height of the interface. The pre-exponential factor A^* is the Richardson constant ($1.2 \cdot 10^5$ mA/K^2/cm^2).

In addition to the potential applied to the photodiode, these devices also convert incident light into additional potential called photovoltage, E_{ph}. The amount of photovoltage generated by a photodiode is assumed to be equal to its open circuit potential, which is the potential of the photodiode when no current passes through it. In this model, the photovoltage is defined by Equation 4.15.

4.15 $$E_{ph} = \frac{nkT}{q} \ln\left(\frac{j_{ph}}{j_o \gamma} + 1\right)$$

To maximize the photovoltage, the reverse bias saturation current density must be small and the photocurrent must be high. This is accomplished by limiting the rate of recombination. The surface roughness must also be small. With high surface areas, the number of minority charge carriers are distributed over a large area, making the concentration of surface charge low, relative to low surface area diodes.

The Butler-Volmer equation is the conventional mathematical framework for modeling the current-potential relationships for metal electrocatalysts. This version of the equation, shown as Equation 4.16, is slightly modified from the original form because it includes the photovoltage supplied to the electrocatalyst in addition to the applied potential.

4.16 $$i_{k_x} = A_x j_{k_x} \left(\exp\left[\frac{\alpha q(E - E_{eq} - E_{ph})}{kT}\right] - \exp\left[\frac{-(1-\alpha) q(E - E_{eq} - E_{ph})}{kT}\right]\right)$$

For a particular catalyst surface x, which is either Si or Pt in this version of the model, the kinetic current is dependent on the surface area of the catalyst A_x and its exchange current density j_{kx}. The exchange current density is the current density of the forward and reverse reactions at the equilibrium potential E_{eq}, where the net current is zero. This is a material-specific property that has a large value for efficient catalytic surfaces. The number of electrons transferred per reaction is z, and α is the charge transfer coefficient. This coefficient is related to the Tafel slope, which specifies how much additional potential needs to be applied to an electrocatalyst to increase the rate of reaction by an order of magnitude. For this analysis, however, α is set to 0.5. The first exponential term in this reaction governs the rate of oxidation reactions at the catalyst surface while the second exponential term is related to the rate of reduction. When the overpotential E-E_{eq} is sufficiently negative, the reduction term dominates, resulting in cathodic (negative) currents.

It must be understood that this model assumes the interface is a buried junction that has a uniform barrier height across the entire device. As mentioned in Chapter 2, this is not the case when the SC surface is covered with metal particles instead of a film. For this reason, the model is not intended to directly predict how certain systems will behave. It is instead aimed at determining how changing certain parameters will affect the performance.

4.3.2 Basic Features

The base case in all aspects of the work in this dissertation is the bare, planar Si electrode. The components of this model that correspond to this base case are shown in Figure 4.6. The area of the Si surface is set to 1 cm^2, and the Si exchange current density

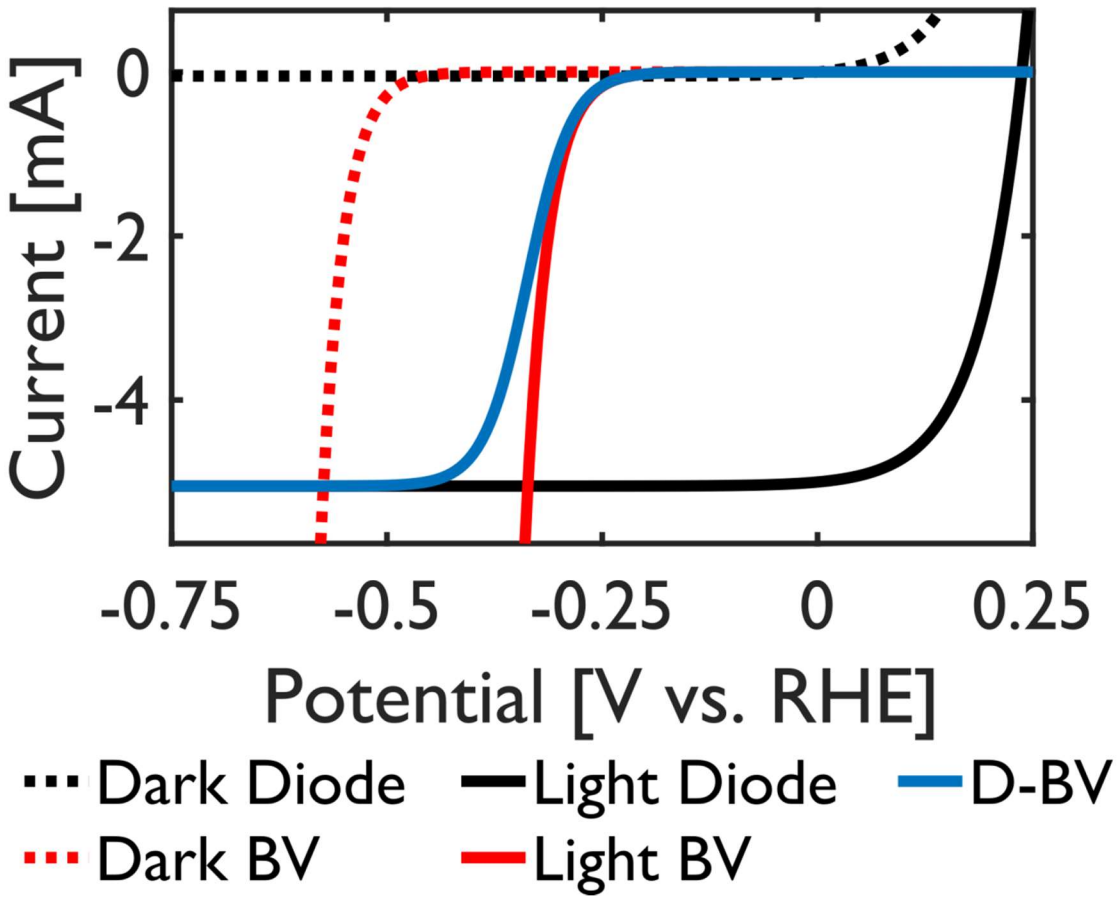

Figure 4.6: Individual diode and Butler-Volmer (BV) components of the model and their resulting series combination (D-BV). The equilibrium potential for the HER is 0 V vs. RHE.

is set to 10^{-9} mA/cm^2, which is at the lower end of the range specified by Zhang (10^{-9} to 10^{-3} mA/cm^2).[18] This value was chosen because it gives a reasonable fit to previous experimental measurements. In this figure, the diode is shown in both dark and light conditions. The lower current limit of the diode is specified by the photocurrent term, and the potential limit on the right is specified by its barrier height. The photovoltage is defined here as the difference in potential between the dark diode and light diode at zero current. The Butler-Volmer (BV) components are also shown in dark and light conditions. There is a positive shift in the onset of potential under illumination. This is caused by the supply of photovoltage from the diode. When the light diode and BV components are considered in series with each other, the diode specifies the lower current limit while the BV curve dictates the onset of current. If the diode has infinite photocurrent, the composite plot would be identical to the BV plot. Alternatively, if the BV component has an infinite exchange current density (i.e., it is a "perfect" catalyst), the composite plot would overlap the diode plot. Therefore, it is clear that improving the catalytic rate and the photocurrent is vital to improving the efficiency of the device.

4.3.3 Surface Reaction Rate

A goal of any catalyst development process is to limit the efficiency losses caused by reactions. In the case of this work, electrocatalytic Pt nanoparticles are added to the Si surface to reduce these losses. The exchange current density of Pt for the HER is generally accepted to be about 1 mA/cm^2, far greater than the value for Si. Experimentally, about 6% of the Si surface is covered with hemispherical Pt nanoparticles (Chapter 5). The base area of a hemisphere is half of its curved surface area. Therefore, there are 0.12 cm^2 of Pt per total electrode area, leaving 0.94 cm^2 of Si surface area. These surface areas and the

corresponding exchange current values are fed to the BV equations. Similarly, the surface roughness changes from 1 to 1.06. The addition of Pt surface area reduces the device's kinetic limitations but slightly reduces the photovoltage generated by the diode (Figure 4.7A). There is a point where the balance between the addition of Pt surface area and the loss of photovoltage generates an optimum onset potential. For Pt surface areas higher than this optimum point, the performance of the electrode is degraded due to a large loss of photovoltage. These results are shown in Figure 4.7B.

4.3.4 Light-Limited Photocurrent

A major focus of this dissertation is to identify how metals and texturing can influence the behavior of the PEC systems. The results from Subsection 4.2.2 are used here as an example. Based on those calculations, the EQE for bare Si under 700 nm light should be 73%. If a 50/50 (plasmonic/parasitic) particle is located 10 nm below the Si surface, the EQE is calculated to be 38% at this wavelength. If the bare Si is texturized so that its reflectance is reduced from its original 22% to 12% at 700 nm, the EQE becomes 84%. The photocurrent term in this model is equal to the product of intensity of the light source (manipulated to be in mA/cm^2 units) and the EQE. The EQEs when the 50/50 particle is included (Si+50/50) and when the reflectance is reduced to 12% (Si-12%) are 52% and 115% of the bare Si EQE, respectively. Therefore, the photocurrents for the Si+50/50 and Si-12% cases are 2.6 and 5.8 mA, respectively, based on the original 5 mA for the bare Si. These effects are shown in Figure 4.8A.

4.3.5 Barrier Height

The final major parameter that governs the performance of a PEC device is the barrier height. In a system where the interface is defined by the Si VB and the HER

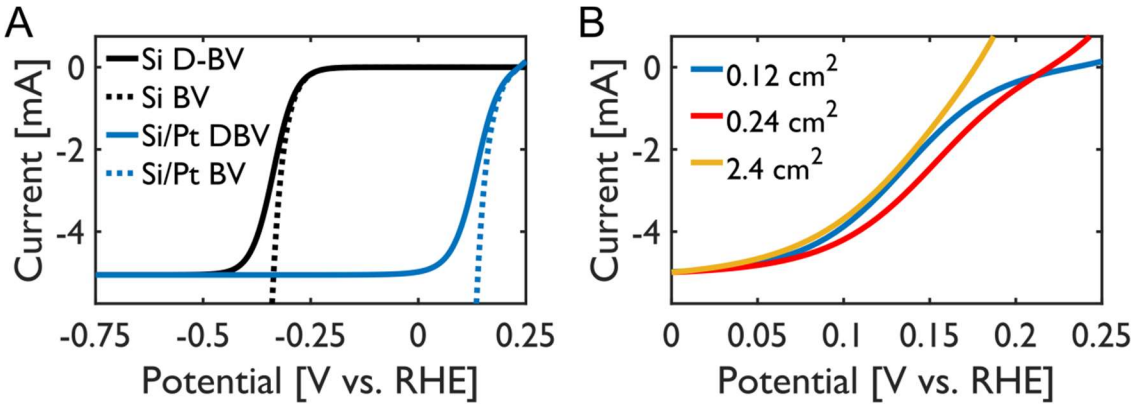

Figure 4.7: Modeled effects of loading catalysts onto a Si photocathode (A) Effect of depositing Pt electrocatalysts on the Si surface. Si results are shown in black, Si/Pt results are shown in blue. The dashed plots show the BV performance for the Si vs. the Pt surface. The solid plots are the calculated diode and Butler-Volmer combinations. (B) Effect of increasing the Pt surface area. The red curve shows near-optimal loading.

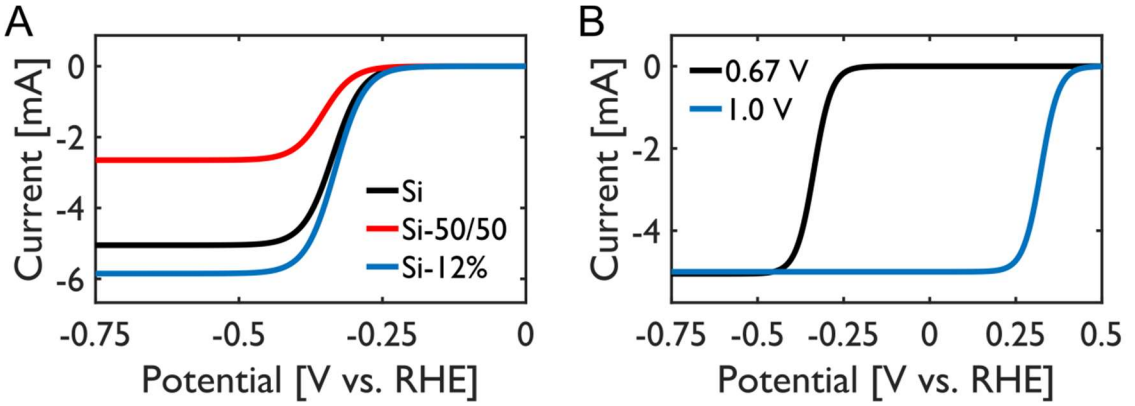

Figure 4.8: Modeled effects of changing the optical properties and barrier heights of a Si photocathode (A) Effect of changing the photocurrent term at 700 nm. The black plot is bare Si, the red is Si with 50/50 particles at a depth of 10 nm into the Si, and the blue is Si that has only 12% reflectance. (B) The effect of changing the barrier height from 0.67 to 1.0 V.

electrolyte Fermi level, the barrier height is around 0.67 V. Technically, the inclusion of Pt nanoparticles on the surface results in "pinched-off" barriers that are lower than the Si/electrolyte barrier height (Chapter 2). This effect is not included in this model. Instead, a p-n junction can be used to decouple the barrier height from the electrolyte (Chapter 2), and a barrier height of 1 V can be reasonably achieved. This greatly enhances the onset potential of the system due to reduced rates of majority charge carriers being emitted into the electrolyte (Figure 4.8B).

4.3.6 Target System

To improve the performance of photoelectrodes, the surface reaction rates, photocurrent, and interface properties must be improved simultaneously. Figure 4.9 shows the net effect of this strategy. The onset potential is shifted far into the positive potential range and the light-limited current is improved noticeably. Achieving this degree of improvement is vital for improving a photoelectrode to the point that it could be used as component of an efficient photocatalyst.

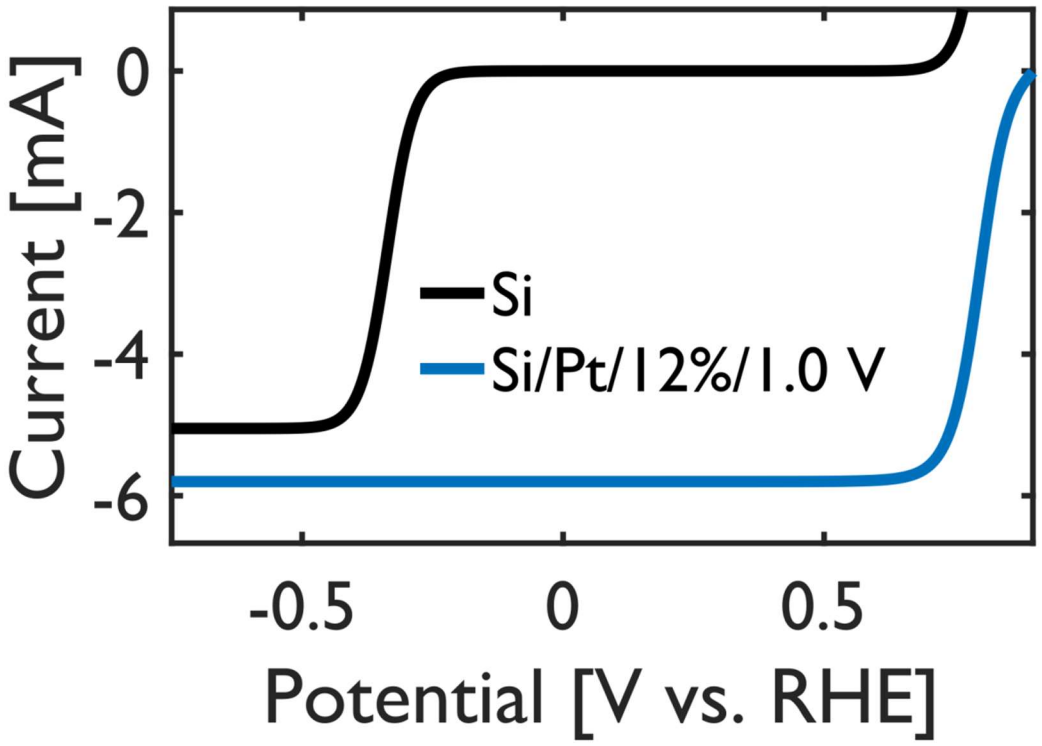

Figure 4.9: Combined catalytic, optical, and barrier height effects from the D/B-V model (Black) Bare, planar Si D-BV curve. The barrier height is 0.67 V and photocurrent is 5 mA. (Blue) Si with 6% of the surface covered with Pt hemispheres. The photocurrent is 5.75 mA because the reflectance is reduced to 12%, and the barrier height is 1.0 V.

4.4 Conclusion

Through this modeling work, the role of metal nanoparticles on the changing the properties of PEC devices is more thoroughly understood. For a good SC like Si that does not suffer from short charge carrier diffusion lengths, metal nanoparticles can only be expected to result in a loss of external quantum efficiency. However, to improve the surface reaction rates, electrocatalysts must be attached to the SC surface. It is important to develop a way to achieve high surface reactivity and high photocurrents simultaneously. In addition to these enhancements, if the barrier height can be improved, the device can become very efficient due to suppressed loss mechanisms. The work in Chapters 5 and 6 explores experimental methods for accomplishing these goals.

4.5 References

(1) Ingram, D. B.; Linic, S. Water Splitting on Composite Plasmonic-Metal/Semiconductor Photoelectrodes: Evidence for Selective Plasmon-Induced Formation of Charge Carriers near the Semiconductor Surface. *J. Am. Chem. Soc.* **2011**, *133* (14), 5202–5205.

(2) Thomann, I.; Pinaud, B. A.; Chen, Z.; Clemens, B. M.; Jaramillo, T. F.; Brongersma, M. L. Plasmon Enhanced Solar-to-Fuel Energy Conversion. *Nano Lett.* **2011**, *11* (8), 3440–3446.

(3) Pillai, S.; Catchpole, K. Surface Plasmon Enhanced Silicon Solar Cells. *J. Appl. Phys.* **2007**, *101* (9), 93105.

(4) Temple, T. L.; Mahanama, G. D. K.; Reehal, H. S.; Bagnall, D. M. Influence of Localized Surface Plasmon Excitation in Silver Nanoparticles on the Performance of Silicon Solar Cells. *Sol. Energy Mater. Sol. Cells* **2009**, *93* (11), 1978–1985.

(5) Das, S.; Kundu, A.; Saha, H.; Datta, S. K. Role of Metal and Dielectric Nanoparticles in the Performance Enhancement of Silicon Solar Cells. *J. Mod. Opt.* **2012**, *59* (14), 1219–1231.

(6) Matheu, P.; Lim, S. H.; Derkacs, D.; McPheeters, C.; Yu, E. T. Metal and Dielectric Nanoparticle Scattering for Improved Optical Absorption in Photovoltaic Devices. *Appl. Phys. Lett.* **2008**, *93* (11), 113108.

(7) Akimov, Y. A.; Koh, W. S.; Ostrikov, K. Enhancement of Optical Absorption in Thin-Film Solar Cells through the Excitation of Higher-Order Nanoparticle Plasmon Modes.

Opt. Express **2009**, *17* (12), 10195.

(8) Green, M. A.; Keevers, M. J. Optical Properties of Intrinsic Silicon at 300 K. *Prog. Photovoltaics Res. Appl.* **1995**, *3* (3), 189–192.

(9) Kim, T. W.; Choi, K.-S. Nanoporous $BiVO_4$ Photoanodes with Dual-Layer Oxygen Evolution Catalysts for Solar Water Splitting. *Science* **2014**, *343* (6174), 990–994.

(10) DeVore, J. R. Refractive Indices of Rutile and Sphalerite. *J. Opt. Soc. Am.* **1951**, *41* (6), 416.

(11) Hoang, S.; Guo, S.; Hahn, N. T.; Bard, A. J.; Mullins, C. B. Visible Light Driven Photoelectrochemical Water Oxidation on Nitrogen-Modified TiO_2 Nanowires. *Nano Lett.* **2012**, *12* (1), 26–32.

(12) Tyagi, M. S.; Van Overstraeten, R. Minority Carrier Recombination in Heavily-Doped Silicon. *Solid. State. Electron.* **1983**, *26* (6), 577–597.

(13) Lai, Y.; Zhuang, H.; Xie, K.; Gong, D. Fabrication of Uniform Ag/TiO_2 Nanotube Array Structures with Enhanced Photoelectrochemical Performance. *New J. Chem.* **2010**, *34* (7), 1335–1340.

(14) Li, Z.; Luo, W.; Zhang, M.; Feng, J.; Zou, Z. Photoelectrochemical Cells for Solar Hydrogen Production: Current State of Promising Photoelectrodes, Methods to Improve Their Properties, and Outlook. *Energy Environ. Sci.* **2013**, *6* (2), 347.

(15) Oh, J.; Deutsch, T. G.; Yuan, H.-C.; Branz, H. M. Nanoporous Black Silicon Photocathode for H2 Production by Photoelectrochemical Water Splitting. *Energy Environ. Sci.* **2011**, *4* (5), 1690.

(16) Huang, Z.; McKone, J. R.; Xiang, C.; Grimm, R. L.; Warren, E. L.; Spurgeon, J. M.; Lewerenz, H.-J.; Brunschwig, B. S.; Lewis, N. S. Comparison between the Measured and Modeled Hydrogen-Evolution Activity of Ni- or Pt-Coated Silicon Photocathodes. *Int. J. Hydrogen Energy* **2014**.

(17) Trotochaud, L.; Mills, T. J.; Boettcher, S. W. An Optocatalytic Model for Semiconductor–Catalyst Water-Splitting Photoelectrodes Based on In Situ Optical Measurements on Operational Catalysts. *J. Phys. Chem. Lett.* **2013**, *4* (6), 931–935.

(18) Zhang, X. G. *Electrochemistry of Silicon and Its Oxide*; Springer, 2001.

CHAPTER 5

Interaction of Metal Nanoparticle Co-Catalysts with Flat Semiconductor Photoelectrodes: The Impact of Pt on the Optical and Catalytic Properties of Si for Hydrogen Evolution

5.1 Summary

The inclusion of metal nanoparticle electrocatalysts on semiconductor photoelectrodes is often used to increase the efficiency of photocatalytic reactions on semiconductors. It is well established that metal electrocatalysts can limit overpotential losses associated with many important photocatalytic reactions, significantly increasing the efficiency of the conversion of solar into chemical energy. On the other hand, the introduction of metal nanoparticles can also impact the light-absorbing properties of semiconductors. We have studied the impact of the introduction of Pt nanoparticles on the optical and catalytic properties of flat Si photoelectrodes for the photoelectrocatalytic evolution of hydrogen. We demonstrate that the deposition of platinum nanoparticles onto planar Si photocathodes results in improved catalytic rates for the hydrogen evolution reaction, but also a diminished light-limited rate of photon to hydrogen conversion. We also show that by embedding Pt nanoparticles into Si, the light-limited rates are significantly improved while preserving the improved catalytic rates. We provide mechanistic insights that allow us to shed light on these experimental findings and discuss design principles to simultaneously improve the kinetic and optical properties of a planar Si photocathode through the judicious introduction of metal nanoparticles.

5.2 Introduction

The conversion of solar energy into chemical energy has recently received significant attention.[1–4] These processes require materials that can efficiently absorb light and convert its energy into energetic charge carriers, which drive electrochemical reduction and oxidation half-reactions. Semiconductors have been demonstrated to be useful light-absorbing materials; however, these materials often have poor electrocatalytic properties, requiring significant overpotentials to drive chemical transformations. To improve the performance of semiconductors, metal electrocatalysts are routinely loaded onto the semiconductor light-absorbers.[5–14] In these composite systems, the role of the metal electrocatalysts is to provide surface sites where the electrocatalytic transformations can take place with lower overpotentials compared to the surface of the semiconductor. To provide a large number of reactive sites, these electrocatalysts are often introduced in the form of nanoparticles.

In addition to being catalytically active, metallic nanoparticles are also optically active, and they can affect the light-absorbing properties of the semiconductor. For example, metal nanoparticles can reflect, scatter and absorb light. The absorption of light by metal nanoparticles induces electronic excitations in the metal where the energy of absorbed photons is parasitically converted into heat, consequently limiting external quantum efficiencies.[15–17] Furthermore, under certain conditions, light-metal interactions result in localized surface plasmon resonance (LSPR), with metal nanoparticles exhibiting increased absorbing and scattering cross-sections as well as strong electric fields in regions near the particle surface. The ability of metallic nanoparticles to scatter light and generate intense electric fields through LSPR has been exploited to enhance the charge carrier

generation rates in some semiconductor light absorbers.[9,18–23] These LSPR-induced enhancements have been demonstrated to be useful mainly in semiconductor systems that suffer from poor photon absorption and/or short charge carrier diffusion lengths.

Semiconductors characterized by efficient light absorption and long charge carrier diffusion lengths, such as mono-crystalline silicon that is hundreds of microns thick, benefit from the inclusion of metallic electrocataysts through a reduction of the overpotentials required to drive reactions. Unfortunately, the addition of metallic electrocatalysts to these systems can lead to poorer optical absorption in the semiconductor, resulting in lower light-limited reaction rates.[5,6,14,16,17,24] In this contribution, we analyze how to overcome the optical absorption losses caused by the introduction of metal nanoparticles without compromising the metal-induced reduction of the overpotential. We investigate this issue via a case study focusing on the impact of the introduction of Pt nanoparticle co-catalysts on the optical and catalytic properties of planar, single-crystal silicon (Si) photocathodes in the photoelectrochemical hydrogen evolution reaction (HER). We note that Si has been demonstrated to have excellent visible light absorption[25] and charge transport[26] properties. Pt is known to be the most active pure metallic HER electrocatalyst.[27] We focus on three different model systems: planar Si without Pt, planar Si with Pt nanoparticles deposited on the surface of Si, and planar Si with Pt nanoparticles embedded into the Si. We demonstrate that the introduction of Pt nanoparticles can induce changes to the optical properties of Si, including significant losses due to direct light absorption by Pt. We show that these losses can be eliminated if Pt nanoparticles are embedded into the semiconductor. Using this model system, we have

developed design principles to simultaneously improve the kinetic and optical properties of a planar Si photocathode by judicious introduction of metal nanoparticles.

5.3 Methods

The silicon used in this work was derived from single-side polished p-type wafers of 100 mm diameter and <100> surface orientation purchased from Silicon Valley Microelectronics, Inc. The material was boron doped, exhibiting 10-20 Ω·cm resistivity. The 525 ± 25 μm thick wafers were diced into 13 mm squares which were used as photocathodes for the HER. Identical wafers were also diced into 28 mm squares for optical measurements. All Si chips were washed in piranha solution (3:1 mixture of concentrated sulfuric acid and 30% hydrogen peroxide) for three hours and then thoroughly rinsed with ultrapure water. Immediately before their use, the Si chips were submerged in 0.5 M hydrofluoric acid (HF) for 15 minutes to remove the native oxide layer present on the Si. Pt nanoparticles were deposited onto the oxide-free silicon surface using an electroless deposition method based on the work by Lombardi.[6] In short, after rinsing in ultrapure water and drying under compressed air, the Si sample was submerged in a 10 mL solution of 0.25 M HF and 1 mM H_2PtCl_6-$6H_2O$ for 2 minutes and then rinsed and dried again. This method produced hemispherical Pt nanoparticles with an average diameter of 150 nm. This process was preferred over the drop-coating of colloidal Pt nanoparticles onto Si because there is no capping agent to inhibit the transfer of electrons from the Si to the Pt. To embed Pt nanoparticles into the silicon chips, we used a method similar to one described by Tsujino.[28,29] The Si chip laden with Pt nanoparticles was submerged in a 10 mL solution of 2.2 M HF and 0.16 M H_2O_2 for about 45 seconds. The chip was then thoroughly rinsed in ultrapure water and dried under compressed air. In this

embedding process, the Pt nanoparticles act as catalysts for dissolving the Si that is directly in contact with the particles, resulting in the burrowing of the Pt particles into the Si. The process forms Si with pores typically 100 to 300 nm deep with a Pt nanoparticle at the bottom of each pore. This approach differs from the conventional strategy of creating surface-roughened Si that is later decorated with Pt nanoparticles. Typically, Ag or Au nanoparticles are used instead of Pt to drive the pore formation.[14,24,30–32] In cases when Pt nanoparticles are to be included, they are added after removing the pore-forming metals through chemical or dry etching.

The optical characterization of the materials was performed using an integrating sphere from LabSphere by measuring the wavelength dependent reflectance and absorptance. The reflectance was measured with a silicon photodiode detector from the Newport Corporation. We note that due to the relatively large thickness of the Si chips, there was no measurable light transmission through the sample. Monochromatic light was provided by a 1000 W Xe lamp and a Cornerstone 260 monochromator. Illumination was performed at near-normal incidence to the front of the samples.

The photoelectrochemical HER activity of the materials was measured using a three-electrode photoelectrochemical cell with a Gamry Reference 3000 potentiostat under monochromatic visible-light illumination using the lamp/monochromator system described above. All measurements were performed in 0.1 M perchloric acid with a Hg/Hg_2SO_4/saturated K_2SO_4 reference electrode and a Pt wire counter electrode. H_2 was bubbled into the cell to establish the equilibrium potential of the H^+/H_2 redox couple. Bubbling H_2 also prevents the dissolution of the Pt counter electrode.[33,34]

An ohmic contact between the working electrode and the rest of the system was made through the back of the silicon photocathodes by lightly scratching it with a diamond scribe to ensure the removal of native oxide. A gallium-indium eutectic mixture (Sigma-Aldrich) was painted onto this surface which was then pressed against a Cu plate. The working electrodes were housed in a casing made of VisiJet M3 Black, a polymer produced by 3DSystems. The casing was made using 3D printing technology allowing for reproducible and consistent incident photon fluxes for all the measurements. The use of the 3D printed device was critical for minimizing variability in the measurements.

Scanning electron microscopy (SEM) was performed using a FEI Nova 200 Nanolab SEM/FIB at an accelerating voltage of 5 kV. The focused ion beam (FIB) was used to generate samples employed in cross-sectional SEM imaging. The FIB cutting procedure was also used to generate electronically transmitting thin slices of the specimens for transmission electron microscopy (TEM). TEM and energy-dispersive X-ray spectroscopy (EDS) were performed with an aberration corrected JEOL 2100F at an accelerating voltage of 200 kV.

5.4 Results and Discussion

The SEM and TEM images in Figure 5.1 show representative Si/Pt samples used in the measurements. Figure 5.1A shows a SEM image of Pt nanoparticles grown on the top of a Si surface. Using ImageJ analysis,[35] we established that the Pt nanoparticles occupy ≈ 6% of the Si surface area and have an average diameter of 150 nm. A particle size distribution plot using data from multiple SEM images is shown in Figure 5.1B. The SEM image in Figure 5.1C shows Pt nanoparticles embedded into a porous Si surface. The inset

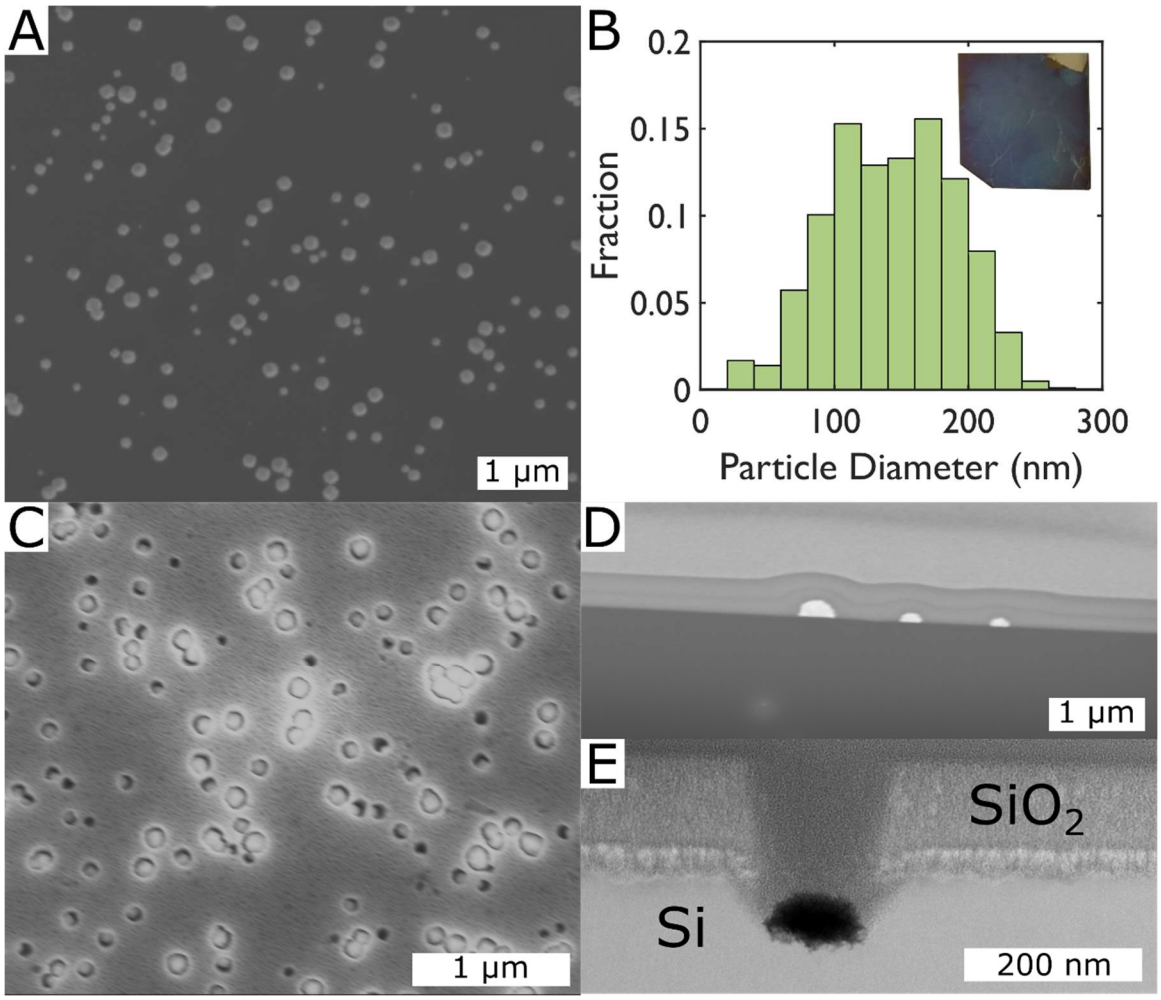

Figure 5.1: Results from electron microscopy analyses. (A) SEM image of Pt nanoparticles deposited onto a planar Si surface. (B) Particle size distribution of deposited Pt nanoparticles from multiple samples. The inset is an optical photograph of the Si surface with embedded Pt. (C) SEM image of Pt nanoparticles embedded into Si. (D) Cross-sectional SEM image of on-surface Pt nanoparticles on Si. (E) Bright field cross-sectional TEM image of an embedded Pt particle.

optical image in Figure 5.1B shows that embedding the Pt nanoparticles changes the macroscopic optical appearance of the Si chip from gray and shiny to dark blue and matte. Cross-sectional SEM and TEM images of representative samples containing the on-surface and embedded Pt nanoparticles are shown in Figure 5.1D and Figure 5.1E, respectively. These images show that the Pt particles are hemispherical, with the flat sides of the hemispheres directly contacting the Si surface. In the case of embedded Pt, the bottoms of the pores are generally the same diameter as their associated Pt nanoparticles with a slight increase in the pore diameter at the top of the pores.

Figure 5.2 shows a dark field cross-sectional TEM image of Pt embedded into Si as well as EDS elemental maps associated with these samples. The elemental mapping of Si, Pt, and O demonstrates that the Pt nanoparticles are not altered by the embedding process. We note that the extra Pt observed across the entire sample is due to the plating of the sample with Pt which was required to create viable samples for TEM imaging. This plating served as a protection layer so the sample would remain intact during the ion milling FIB process used to create thin, electronically transparent specimens conducive for TEM imaging. We also observe elevated levels of oxygen at the surface of the Si material. This is caused by the creation of Si-oxide surface layers that cannot be avoided since the material is exposed to H_2O_2 during the embedding process.

The cyclic voltammetry (CV) data in Figure 5.3A show the relationship between electric potential (i.e., the controlled potential of the Si majority charge carriers) and the photocurrent density (i.e., the reaction rate) generated through photoelectrochemical H_2 evolution under normal incidence 690 nm monochromatic illumination at an intensity of 1.1 mW/cm^2. The photocurrent density was obtained by subtracting the dark current from

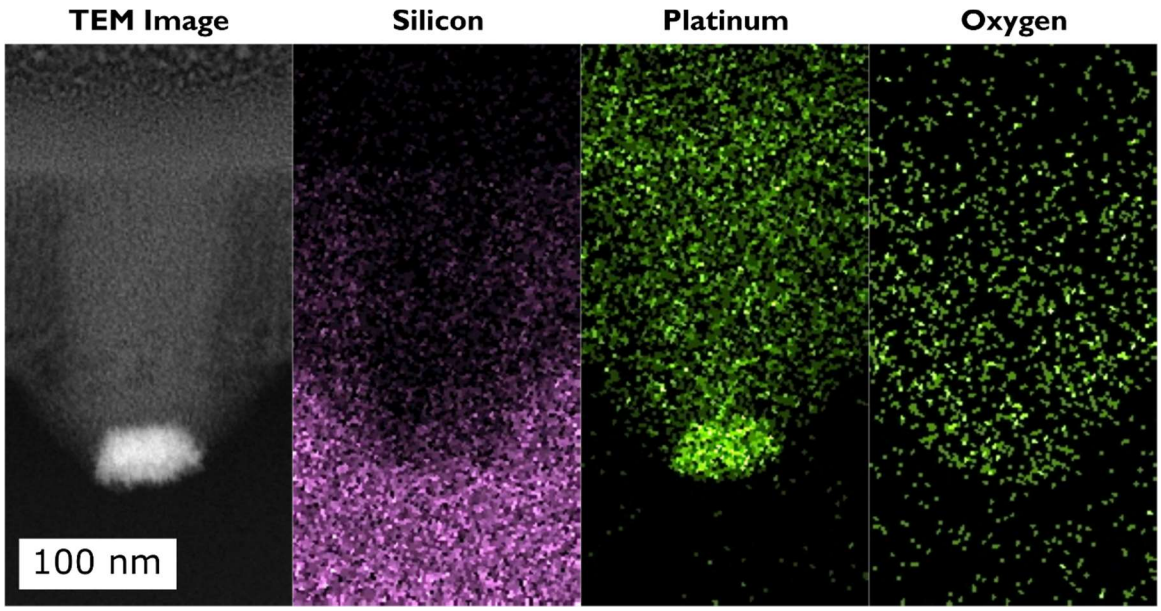

Figure 5.2: Dark field cross-sectional TEM image of an embedded Pt nanoparticle and the corresponding EDS maps for silicon, platinum, and oxygen.

the light-on current and then dividing by the projected surface area of the Si exposed to the light. At this wavelength, the maximum possible light-limited photocurrent was measured to be 0.59 mA/cm^2, using an electrolyte-resistant reference solar cell to account for the attenuation of light intensity from the light source to the sample surface. To obtain the CV data, the potential was swept from -1.8 V to 0.3 V vs. RHE and back to -1.8 V vs. RHE at a rate of 50 mV/s. As expected, the introduction of Pt nanoparticles has significant benefits for the surface reaction rates of the HER as it leads to a reduction in the overpotential required to drive the reaction. For a bare planar silicon electrode, the half-wave potential was -0.35 V vs. RHE. The inclusion of Pt nanoparticles on the surface improves this quantity to 0.07 V vs. RHE. Upon embedding the Pt nanoparticles into the Si electrode, the half-wave potential shifts to 0.13 V vs. RHE. More significantly, the data also show that the light-limited photocurrent densities, measured at strongly reducing (negative) potentials, are enhanced by ≈ 15% and 24% for the system with embedded Pt nanoparticles compared to the bare and surface-bound Pt systems, respectively. The flat Si electrode with embedded Pt nanoparticles is clearly the most effective photon converter under this wavelength of light.

To further probe the performance of these systems, we measured the light-limited photocurrent as a function of wavelength. The data in Figure 5.3B show the steady-state light-limited photocurrents measured at -1.8 V vs. RHE at different wavelengths for various Si/Pt photoelectrodes normalized by the photocurrent for the bare Si electrode. The data show that depositing the Pt nanoparticles onto the Si surface hinders the light-limited photocurrent relative to bare, planar Si at all wavelengths. On the other hand, the

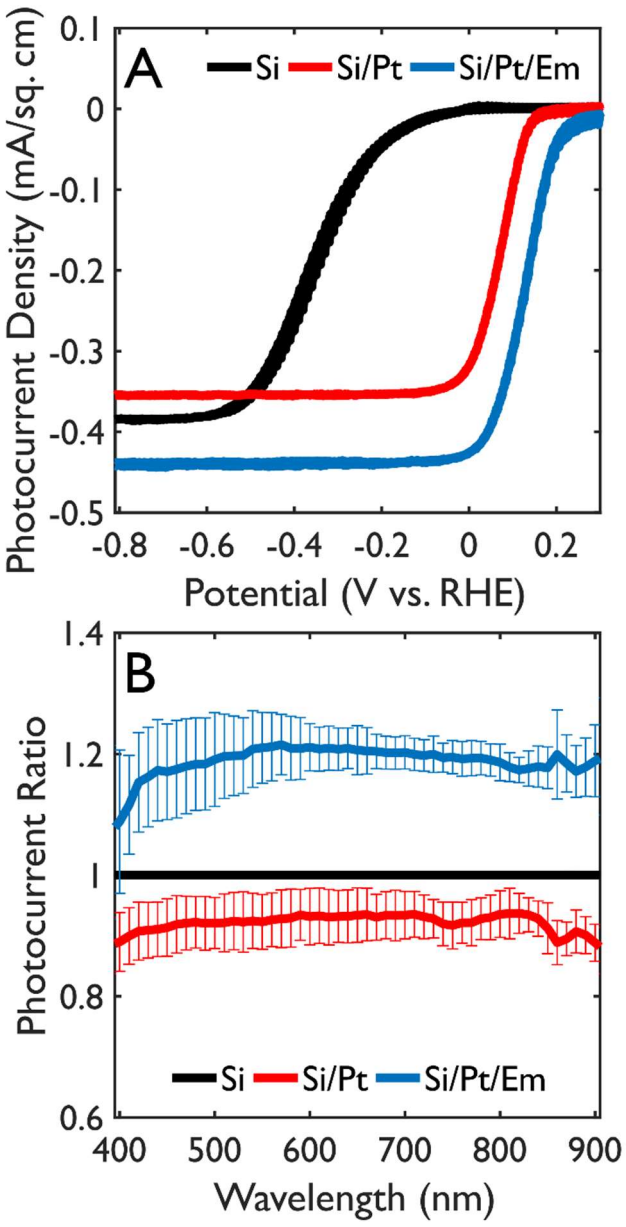

Figure 5.3: Photoelectrochemical measurements for Si/Pt photocathodes (A) Photoelectrochemical HER rates measured under normal-incidence 690 nm illumination (1.1 mW/cm^2) as a function of potential for planar Si, Si with Pt nanoparticles on the surface (Si/Pt), and Si with embedded Pt nanoparticles (Si/Pt/Em). (B) Light-limited photocurrent of Si with Pt nanoparticles on the surface (Si/Pt) and Si with embedded Pt nanoparticles (Si/Pt/Em) normalized with respect to the light-limited photocurrent for planar Si. The data shown are the averages of five identical experiments for Si/Pt and three for Si/Pt/Em. The error bars designate ±1 standard deviation from the mean photocurrent ratio.

data also show that when the Pt nanoparticles are embedded into the Si, the photocurrent is significantly enhanced.

To investigate the origin of the observed changes in the light-limited photocurrents upon the deposition and embedding of Pt nanoparticles, we used an integrating sphere apparatus to measure the optical properties of the photoelectrodes under near-normal incidence. We note that the Si chips were thick enough to prevent any detectable transmission at the relevant wavelengths. The data in Figure 5.4 show the fraction of light absorbed by the samples. Planar Si achieves a moderate absorptance below 60% for all wavelengths, which is not surprising considering that it is a relatively reflective substrate across the entire visible spectrum. The deposition of the Pt nanoparticles (150 nm hemispheres) onto the surface of Si at low surface coverage (6% of Si is covered by Pt) slightly increases the system absorptance at wavelengths shorter than 600 nm without otherwise significantly affecting it. Embedding the Pt nanoparticles into the Si electrode results in the significant overall increase in the system absorptance to values greater than 80% at all wavelengths.

We can make several conclusions by comparing the data in Figure 5.3B and Figure 5.4. The first is that the measured loss of light-limited photocurrent (Figure 5.3B) upon growing Pt nanoparticles on top of a planar Si surface is not directly due to the Pt-induced changes in the total absorptance of the system. We observed that the introduction of Pt leads to a very small change in the system absorptance. The data suggest that the loss in the light-limited current in these systems must be due to parasitic absorption by Pt nanoparticles. This absorption process would lead to the formation of short-lived energetic

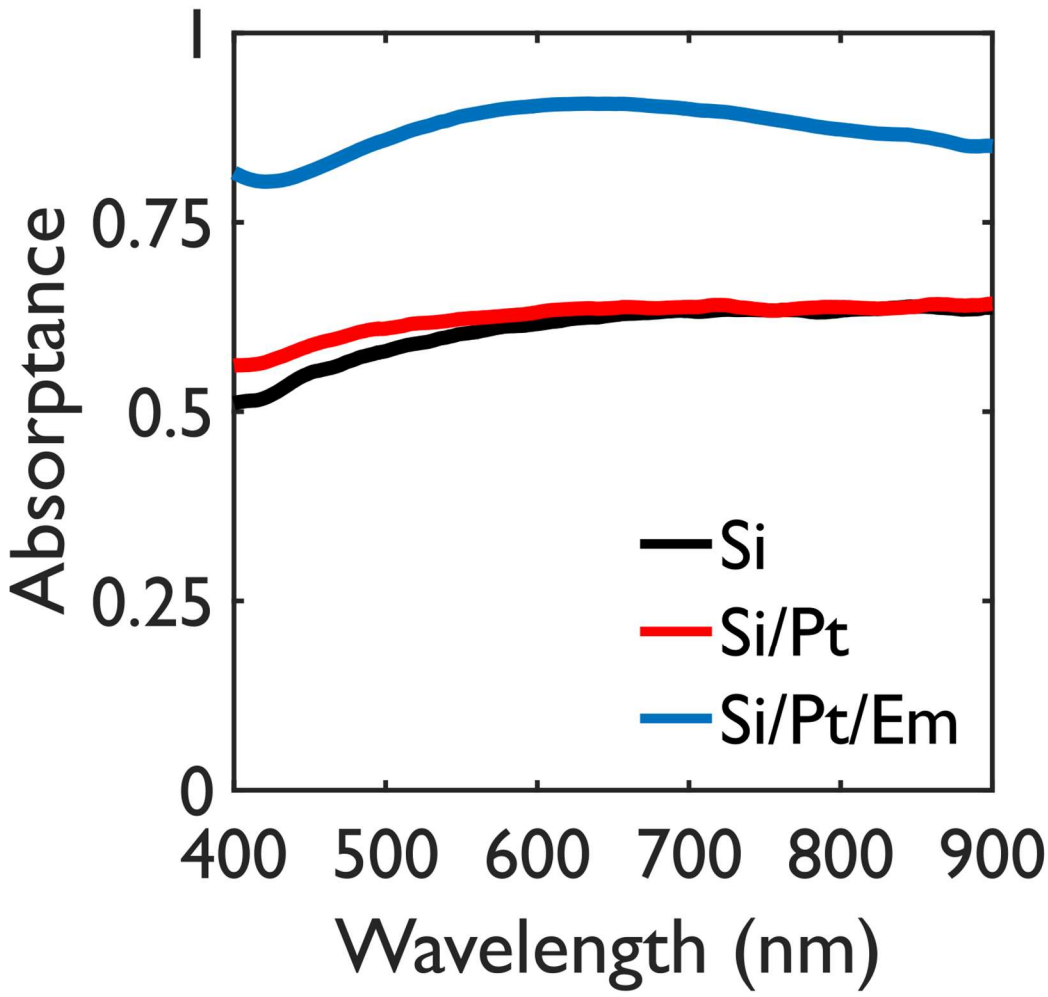

Figure 5.4: Experimental near-normal incidence absorptance spectra for planar Si, Si with Pt on the surface (Si/Pt), and Si with embedded Pt (Si/Pt/Em).

electron-hole pairs in Pt, with their energy rapidly dissipated into heat. The data in Figure 5.3B and Figure 5.4 also suggest that the significant enhancements in the limiting photocurrents observed upon embedding the Pt nanoparticles into Si are caused by significantly higher absorptance in these systems.

While the optical measurements described above quantify the overall absorptance by the different systems, they give little insight about the relative absorption by the individual building blocks: Pt and Si. To further characterize the optical properties of these systems, we performed 3D simulations of the behavior of these systems exposed to electromagnetic fields. These simulations were performed using MEEP,[36] which employs the finite-difference time-domain (FDTD) method to solve Maxwell's equations. The model systems included 150 nm diameter Pt hemispheres on Si or embedded into Si (see insets in Figure 5.5A), as well as bare Si. The Pt coverage on Si was set to match the experimentally measured 6% coverage. The calculations were performed with non-periodic boundary conditions to adequately mimic the experimental conditions. This is an important feature to consider since using periodic boundary conditions in the calculation introduces photonic structures that affect the optics but are not physically relevant for this system.[37,38] The optical properties of the components were specified by fitting Drude-Lorentz models to measured optical data for Si[25] and Pt.[39]

The data in Figure 5.5A show the calculated total absorptance spectra for Si and Si/Pt systems with varying pore depths (0, 75, and 375 nm). The calculated total absorptance in Figure 5.5A is qualitatively consistent with the experimentally measured data shown in Figure 5.4. For example, the simulation data show that at short wavelengths (below 600

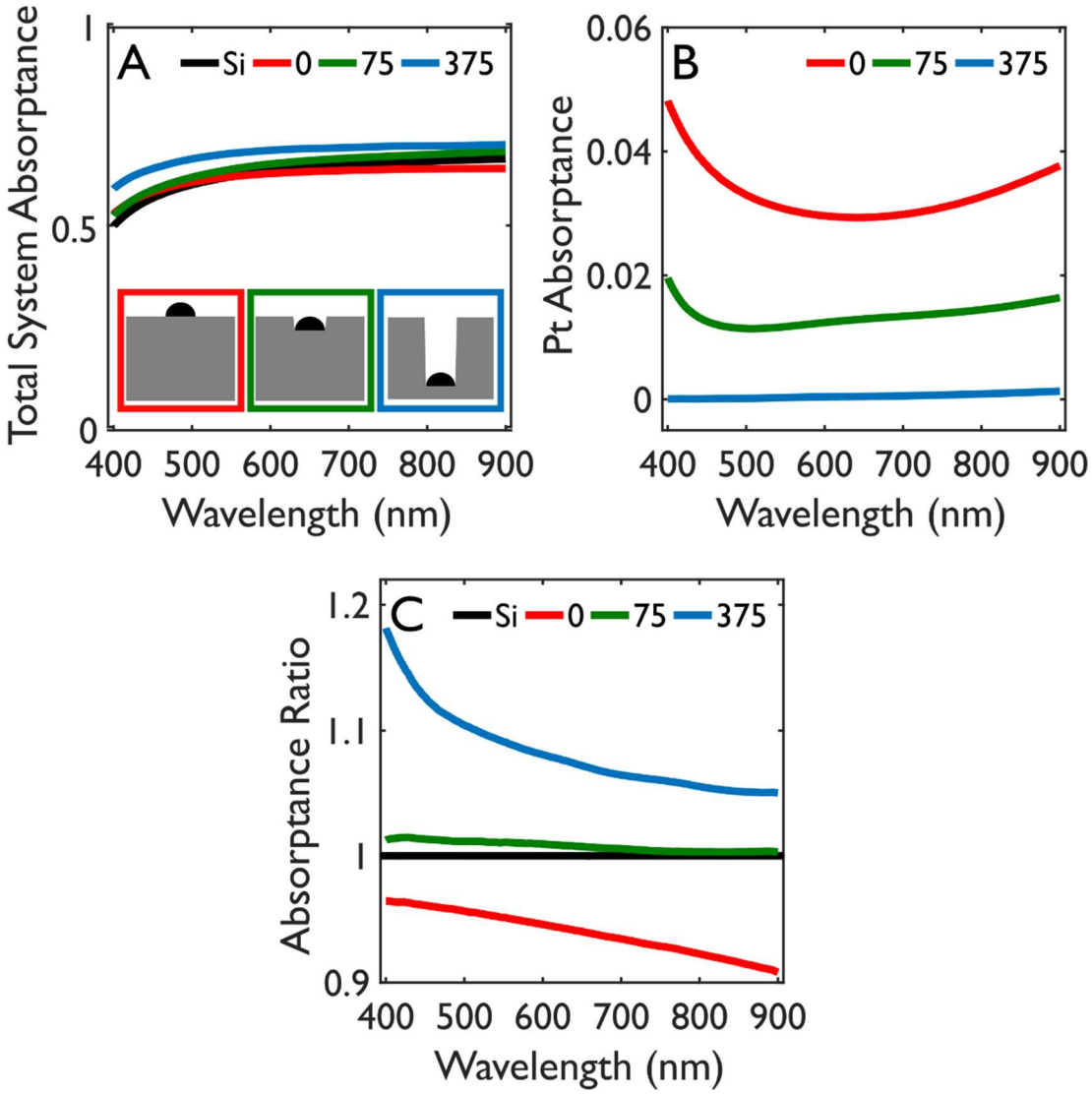

Figure 5.5: Calculated optical properties of planar Si and Si/Pt systems with 150 nm diameter hemispherical Pt nanoparticles in air. The pore depths were 0, 75, and 375 nm. (A) Total system absorptance. The inset figures are color-coded and depict cross-sections of the to-scale simulation cell geometries for the composite systems. (B) Parasitic absorptance in Pt nanoparticles in the composite systems. (C) Absorptance in Si for the different conditions relative to bare, planar Si.

nm) the introduction of on-surface Pt nanoparticles results in an elevated system absorptance, which is consistent with the experiments. The simulations also show that the total absorptance above 600 nm for bare Si is greater than for Si with on-surface Pt. The reason for this is that the introduction of Pt causes more light to be reflected. This is not observed experimentally. We believe that the main reason for this discrepancy is that the Pt nanoparticles are not perfect hemispheres, and that they promote more forward scattering toward the Si than what is captured in the simulations. More importantly, the simulation results in Figure 5.5A also show that for the Pt nanoparticles embedded into Si, there is a clear increase in the system absorptance compared to bare Si at all wavelengths. This increase in the absorptance is present for both shallow and deep pores. This observation is consistent with our experimental measurements in Figure 5.3B.

We have also used the electromagnetic simulations to analyze the absorptance by different components of the composite photoelectrocatalyst. The simulation data in Figure 5.5B show the absorptance by the Pt nanoparticles (150 nm diameter at 6% surface coverage) as a function of wavelength and pore depth. We reiterate that this is a parasitic absorption leading to a transient heating of the nanoparticles. The parasitic absorption in Pt is the result of interband transitions with the rates of absorption being proportional to the imaginary component of the Pt dielectric function. We expected that this parasitic Pt absorptance would exhibit relatively weak wavelength dependence. On the contrary, the data show that Pt absorptance is significantly greater at near UV wavelengths than at higher wavelengths. This greater UV absorptance appears to be a consequence of the excitation of Pt LSPR, which concentrates the electromagnetic energy in the Pt nanoparticles, in the

form of elevated electric fields, at these wavelengths. The LSPR-concentrated energy in the Pt nanoparticles is dissipated through the above-described parasitic absorption by Pt, which is enhanced at the LSPR wavelengths. The simulation data in Figure 5.5B also show that the parasitic Pt absorptance is the highest at all wavelengths for the nanoparticles on the surface of Si, and it gets progressively smaller as the depth of the pore increases. At a depth of 375 nm, this parasitic absorption by Pt is practically eliminated. The reason for this is that at these pore depths, the intensity of light reaching Pt is negligible due to the diffraction of light by the pores. The pore in the Si can be viewed as an aperture through which light is passing. Since the pore is only 150 nm wide, the 400 to 900 nm light passing through it is diffracted. This diffraction directs the incoming light radially outwards from the pore's central axis into the Si. As the pore depth in increased, the Pt particle at the bottom of the pore interacts with a decreasing fraction of the total incoming light, reducing how much it absorbs.

Since a well-functioning photocatalytic system requires high rates of absorption in a semiconductor, which lead to longer-lived energetic charge carriers compared to those formed by the direct absorption in metal, we also investigated the impact of Pt nanoparticles on the rate of absorption in Si. The simulation results in Figure 5.5C show the ratio of the rate of direct photon absorption by Si for a particular composite Si/Pt system to the rate of absorption in bare, planar Si. The data show that Pt nanoparticles deposited on the Si surface cause a reduction in useful absorption by Si across the entire visible range. This reduction is due to the aforementioned parasitic absorption by Pt. Upon embedding the Pt into shallow pores (e.g. 75 nm), the Pt parasitic absorption effect remains; however, some of its magnitude is offset by the forward scattering of light due to

the light diffraction through the pore described above (i.e., the reflection of light is decreased). With a deep pore, the parasitic absorption by Pt is almost completely eliminated and the pore-induced forward scattering, which reduces light reflection, is enhanced. These two effects result in a significant enhancement of the useful absorption in Si relative to bare Si at all relevant wavelengths. The Si/Pt/Em electrode performance suggests there are reduced parasitic absorption and reflectance losses due to the formation of pores with Pt nanoparticles resting at the bottom instead of on the Si surface.

5.5 Conclusion

To summarize, we have studied the impact of the introduction of metal nanoparticles on flat semiconductor electrodes. We demonstrate that, irrespective of the geometry of the metal-particle/semiconductor system, catalytically active metal nanoparticles enhance the surface reactions rates by providing active centers for the reactions to take place with smaller overpotential losses. On the other hand, we show that the metal/semiconductor geometry can have a significant impact on the optical properties of the systems. We demonstrate that in order to optimize the performance of these hybrid systems, it is important to design photocatalysts that minimize the direct interaction of metal nanoparticles with light and therefore limit the parasitic optical losses in the metal. We demonstrate that a geometry of interest involves embedding metal nanoparticles into the flat semiconductor. This embedding process lowers the reflection by the flat semiconductor surface by inducing significant forward scattering through the pores at the semiconductor surface and minimizes the direct interaction of light with the metal nanoparticles which are placed at the bottom of the pores. We note that this embedding of the metal particles in the semiconductor needs be done in way that it does not introduce

additional losses due to diminished transport of the reactant and products to and from the metal active sites, respectively.

5.6 References

(1) Walter, M.; Warren, E.; McKone, J. R.; Boettcher, S. W.; Mi, Q.; Santori, E. A.; Lewis, N. S. Solar Water Splitting Cells. *Chem. Rev.* **2010**, *110* (11), 6446–6473.

(2) Linic, S.; Christopher, P.; Ingram, D. B. Plasmonic-Metal Nanostructures for Efficient Conversion of Solar to Chemical Energy. *Nat. Mater.* **2011**, *10* (12), 911–921.

(3) Maeda, K.; Domen, K. Photocatalytic Water Splitting: Recent Progress and Future Challenges. *J. Phys. Chem. Lett.* **2010**, *1* (18), 2655–2661.

(4) Zhang, X.; Chen, Y. L.; Liu, R.-S.; Tsai, D. P. Plasmonic Photocatalysis. *Reports Prog. Phys.* **2013**, *76* (4), 46401.

(5) Dominey, R. N.; Lewis, N. S.; Bruce, J. A.; Bookbinder, D. C.; Wrighton, M. S. Improvement of Photoelectrochemical Hydrogen Generation by Surface Modification of P-Type Silicon Semiconductor Photocathodes. *JACS* **1982**, *104* (2), 467–482.

(6) Lombardi, I.; Marchionna, S.; Zangari, G.; Pizzini, S. Effect of Pt Particle Size and Distribution on Photoelectrochemical Hydrogen Evolution by P-Si Photocathodes. *Langmuir* **2007**, *23* (24), 12413–12420.

(7) McKone, J. R.; Warren, E. L.; Bierman, M. J.; Boettcher, S. W.; Brunschwig, B. S.; Lewis, N. S.; Gray, H. B. Evaluation of Pt, Ni, and Ni–Mo Electrocatalysts for Hydrogen Evolution on Crystalline Si Electrodes. *Energy Environ. Sci.* **2011**, *4* (9), 3573.

(8) Oh, I.; Kye, J.; Hwang, S. Enhanced Photoelectrochemical Hydrogen Production from Silicon Nanowire Array Photocathode. *Nano Lett.* **2012**, *12* (1), 298–302.

(9) Tanaka, A.; Sakaguchi, S.; Hashimoto, K.; Kominami, H. Preparation of Au/TiO_2 with Metal Cocatalysts Exhibiting Strong Surface Plasmon Resonance Effective for Photoinduced Hydrogen Formation under Irradiation of Visible Light. *ACS Catal.* **2013**, *3* (1), 79–85.

(10) Esposito, D. V; Levin, I.; Moffat, T. P.; Talin, A. A. H_2 Evolution at Si-Based Metal-Insulator-Semiconductor Photoelectrodes Enhanced by Inversion Channel Charge Collection and H Spillover. *Nat. Mater.* **2013**, *12* (6), 562–568.

(11) Kenney, M. J.; Gong, M.; Li, Y.; Wu, J. Z.; Feng, J.; Lanza, M.; Dai, H. High-Performance Silicon Photoanodes Passivated with Ultrathin Nickel Films for Water Oxidation. *Science* **2013**, *342* (6160), 836–840.

(12) Lin, F.; Boettcher, S. W. Adaptive Semiconductor/electrocatalyst Junctions in Water-Splitting Photoanodes. *Nat. Mater.* **2014**, *13* (1), 81–86.

(13) Huang, Z.; McKone, J. R.; Xiang, C.; Grimm, R. L.; Warren, E. L.; Spurgeon, J. M.; Lewerenz, H.-J.; Brunschwig, B. S.; Lewis, N. S. Comparison between the Measured and Modeled Hydrogen-Evolution Activity of Ni- or Pt-Coated Silicon Photocathodes. *Int. J. Hydrogen Energy* **2014**.

(14) Zhao, Y.; Anderson, N. C.; Zhu, K.; Aguiar, J. A.; Seabold, J. A.; van de Lagemaat, J.; Branz, H. M.; Neale, N. R.; Oh, J. Oxidatively Stable Nanoporous Silicon Photocathodes with Enhanced Onset Voltage for Photoelectrochemical Proton Reduction. *Nano Lett.* **2015**, *15* (4), 2517–2525.

(15) Chen, X.; Jia, B.; Saha, J. K.; Cai, B.; Stokes, N.; Qiao, Q.; Wang, Y.; Shi, Z.; Gu, M. Broadband Enhancement in Thin-Film Amorphous Silicon Solar Cells Enabled by Nucleated Silver Nanoparticles. *Nano Lett.* **2012**, *12* (5), 2187–2192.

(16) Theuring, M.; Wang, P. H.; Vehse, M.; Steenhoff, V.; von Maydell, K.; Agert, C.; Brolo, A. G. Comparison of Ag and SiO_2 Nanoparticles for Light Trapping Applications in Silicon Thin Film Solar Cells. *J. Phys. Chem. Lett.* **2014**, 3302–3306.

(17) Khurgin, J. B. How to Deal with the Loss in Plasmonics and Metamaterials. *Nat. Nanotechnol.* **2015**, *10* (1), 2–6.

(18) Tian, Y.; Tatsuma, T. Mechanisms and Applications of Plasmon-Induced Charge Separation at TiO_2 Films Loaded with Gold Nanoparticles. *JACS* **2005**, *127* (20), 7632–7637.

(19) Pillai, S.; Catchpole, K. Surface Plasmon Enhanced Silicon Solar Cells. *J. Appl. Phys.* **2007**, *101* (9), 93105.

(20) Atwater, H. A.; Polman, A. Plasmonics for Improved Photovoltaic Devices. *Nat. Mater.* **2010**, *9* (3), 205–213.

(21) Thomann, I.; Pinaud, B. A.; Chen, Z.; Clemens, B. M.; Jaramillo, T. F.; Brongersma, M. L. Plasmon Enhanced Solar-to-Fuel Energy Conversion. *Nano Lett.* **2011**, *11* (8), 3440–3446.

(22) Ingram, D. B.; Linic, S. Water Splitting on Composite Plasmonic-Metal/Semiconductor Photoelectrodes: Evidence for Selective Plasmon-Induced Formation of Charge Carriers near the Semiconductor Surface. *J. Am. Chem. Soc.* **2011**, *133* (14), 5202–5205.

(23) Wang, H.; You, T.; Shi, W.; Li, J.; Guo, L. $Au/TiO_2/Au$ as a Plasmonic Coupling Photocatalyst. *J. Phys. Chem. C* **2012**, *116* (10), 6490–6494.

(24) Ji, J.; Zhang, H.; Qiu, Y.; Wang, L.; Wang, Y.; Hu, L. Fabrication and Photoelectrochemical Properties of Ordered Si Nanohole Arrays. *Appl. Surf. Sci.* **2014**, *292*, 86–92.

(25) Green, M. A.; Keevers, M. J. Optical Properties of Intrinsic Silicon at 300 K. *Prog. Photovoltaics Res. Appl.* **1995**, *3* (3), 189–192.

(26) Lewis, N. S. A Quantitative Investigation of the Open-Circuit Photovoltage at the Semiconductor/Liquid Interface. *J. Electrochem. Soc.* **1984**, *131* (11), 2496.

(27) Conway, B. E.; Tilak, B. V. Interfacial Processes Involving Electrocatalytic Evolution and Oxidation of H_2, and the Role of Chemisorbed H. *Electrochim. Acta* **2002**, *47* (22), 3571–3594.

(28) Tsujino, K.; Matsumura, M. Boring Deep Cylindrical Nanoholes in Silicon Using Silver Nanoparticles as a Catalyst. *Adv. Mater.* **2005**, *17* (8), 1045–1047.

(29) Tsujino, K.; Matsumura, M. Morphology of Nanoholes Formed in Silicon by Wet Etching in Solutions Containing HF and H_2O_2 at Different Concentrations Using Silver Nanoparticles as Catalysts. *Electrochim. Acta* **2007**, *53* (1), 28–34.

(30) Branz, H. M.; Yost, V. E.; Ward, S.; Jones, K. M.; To, B.; Stradins, P. Nanostructured Black Silicon and the Optical Reflectance of Graded-Density Surfaces. *Appl. Phys. Lett.* **2009**, *94* (23), 231121.

(31) Oh, J.; Deutsch, T. G.; Yuan, H.-C.; Branz, H. M. Nanoporous Black Silicon Photocathode for H_2 Production by Photoelectrochemical Water Splitting. *Energy Environ. Sci.* **2011**, *4* (5), 1690.

(32) Aguiar, J. A.; Anderson, N. C.; Neale, N. R. Revealing the Semiconductor–catalyst Interface in Buried Platinum Black Silicon Photocathodes. *J. Mater. Chem. A* **2016**, *4* (21), 8123–8129.

(33) Hou, Y.; Abrams, B.; Vesborg, P. Bioinspired Molecular Co-Catalysts Bonded to a Silicon Photocathode for Solar Hydrogen Evolution. *Nat. Mater.* **2011**, *10* (6), 434–438.

(34) Nakato, Y.; Yano, H.; Nishiura, S.; Ueda, T.; Tsubomura, H. Hydrogen Photoevolution at P-Type Silicon Electrodes Coated with Discontinuous Metal Layers. *J. Electroanal. Chem. Interfacial Electrochem.* **1987**, *228* (1–2), 97–108.

(35) Schneider, C. A.; Rasband, W. S.; Eliceiri, K. W. NIH Image to ImageJ: 25 Years of Image Analysis. *Nat. Methods* **2012**, *9* (7), 671–675.

(36) Oskooi, A. F.; Roundy, D.; Ibanescu, M.; Bermel, P.; Joannopoulos, J. D.; Johnson, S. G. Meep: A Flexible Free-Software Package for Electromagnetic Simulations by the FDTD Method. *Comput. Phys. Commun.* **2010**, *181* (3), 687–702.

(37) Joannopoulos J.D, Pierre R. Villeneuve, S. F. Photonic Crystals: Putting a New Twist on Light. *Nature* **1997**, *386* (6621), 7.

(38) Joannopoulos, J. D.; Johnson, S. G.; Winn, J. N.; Meade, R. D. *Photonic Crystals: Molding the Flow of Light*, 2nd ed.; Princeton University Press, 2008.

(39) Lynch, D. W.; Hunter, W. R. Comments on the Optical Constants of Metals and an Introduction to the Data for Several Metals. In *Handbook of Optical Constants of Solids*; Palik, E., Ed.; Academic Press, 1997; pp 275–367.

CHAPTER 6

Engineering Interfaces to Improve Photoelectrochemical Efficiency

6.1 Summary

This chapter discusses the properties of the interfaces near the reactive sites for semiconductor photoelectrodes, with a specific focus on the interfaces involved with p-type and p-n Si/Pt devices. The first part of this chapter aims to explain some experimental observations seen in Chapter 5 where an improvement in the onset potential for Si/Pt is observed upon embedding the Pt. The second part of this chapter discusses the use of a p-n junction in combination with embedded co-catalysts to achieve improved efficiency. These combined strategies target the key parameters identified by the Diode/Butler-Volmer model in Chapter 4 (exchange current, photocurrent, and barrier height).

6.2 P-Type Si/Pt Devices

In Chapter 5, the improvement of the surface reaction rate and photocurrent was achieved on a Si photocathode for the HER was accomplished by depositing Pt nanoparticles onto the Si surface and then embedding them into the Si through a selective etching process. The Pt particles catalyze the HER, while the embedding process reduces the reflectance of the surface and reduces the parasitic absorption by Pt. However, upon embedding the Pt, the onset potential also shifts to a more positive (i.e., more efficient) potential. Figure 6.1 shows this shift to be about 0.06 V.

Initially, there were two possibilities considered to be the cause of onset potential change after embedding. The first is that the Pt surface area increased during the selective etching process. It has been suggested that Pt and Au are generally stable when used for metal-assisted etching, while the dissolution of Ag is common under most conditions.[1] However, the dissolution of Au has been observed when the embedding is performed on highly doped p-type silicon, regardless of the HF and H_2O_2 concentrations.[2] Pt is generally less resistant to oxidation and dissolution than Au based on the Pourbaix diagrams shown in Chapter 2, so this possibility must be considered. The Diode/Butler-Volmer model (Chapter 4) can be used to determine if an increase in the Pt surface area is responsible for the 0.06 V shift in the onset potential. The right panel of Figure 6.1 shows results from this model based on the Butler-Volmer kinetics of the Si/Pt surface for different Pt surface areas while generating a photocurrent of 0.35 mA/cm^2 to match the photocurrent density of the Si/Pt electrode in the left panel of Figure 6.1. The surface area of Pt on this kind of Si/Pt electrode has been consistently estimated to be around 0.12 cm^2/cm^2 Si (Chapters 4 and 5). This was used as a starting point for the analysis. When the Pt surface area is increased to 0.36 cm^2/cm^2 Si, the onset potential is nearly optimized, providing only a 0.007 V onset shift at -0.2 mA/cm^2. At very low ($4 \cdot 10^{-4}$ cm^2/cm^2 Si) and very high (36 cm^2/cm^2 Si) loadings of Pt, the onset potential is severely degraded. Based on these results, it is unlikely that an increase in Pt surface area is responsible for the 0.06 V onset shift.

The second possibility is that the gain in photocurrent upon embedding the Pt increased the photovoltage enough to shift the onset by 0.06 V. The photocurrent density increases from 0.35 to 0.44 mA/cm^2 (Figure 6.1 Left Panel). Using the Butler-Volmer model, the photovoltage would be expected to increase by only 0.01 V. Therefore, the

improvement of the onset potential cannot be explained solely by the simultaneous increase of Pt surface area and photovoltage.

With the effects of the Pt surface area and photocurrent ruled out as the main cause, the only major parameter remaining that can influence the performance, based on the Diode/Butler-Volmer model, is the barrier height. Based on this model and an ideality factor of 2, a barrier height increase of 0.06 V can cause an onset potential change of about 0.08 V. Practically speaking, this magnitude of barrier height change is feasible and can explain the change in onset potential upon embedding the Pt. Since the barrier height is descriptor of the interface quality, the effect of the transformation of the interface upon embedding was considered. Previous work on this system includes the cross-sectional SEM and TEM images of the Si/Pt and Si/Pt/Em electrodes, respectively (Figure 6.2). It is clear in these images that the only major change that occurs, beyond forming a pore, is that the Si surface becomes oxidized when Pt is embedded. There is no evidence of such extensive oxidation on the Si/Pt surface. Si normally oxidizes when exposed to air, but the lack of an observable oxide layer on the Si/Pt surface suggests that the H_2O_2 in the embedding solution is the cause of the significant oxidation. Experiments were performed to determine whether this oxidation causes the increase of the barrier height of the system.

6.2.1 Experimental Determination of Oxidation Role

To help confirm that the surface oxidation of the Si is the cause of the improved onset potential upon embedding Pt into Si, two different experiments were performed. The experimental methods used in this work are identical to the methods discussed in Chapter 5. In the first experiment, Si with Pt nanoparticles on the surface was oxidized by exposing it to 10 mL of a 0.16 M H_2O_2 solution for 150 seconds. Cyclic voltammetry was

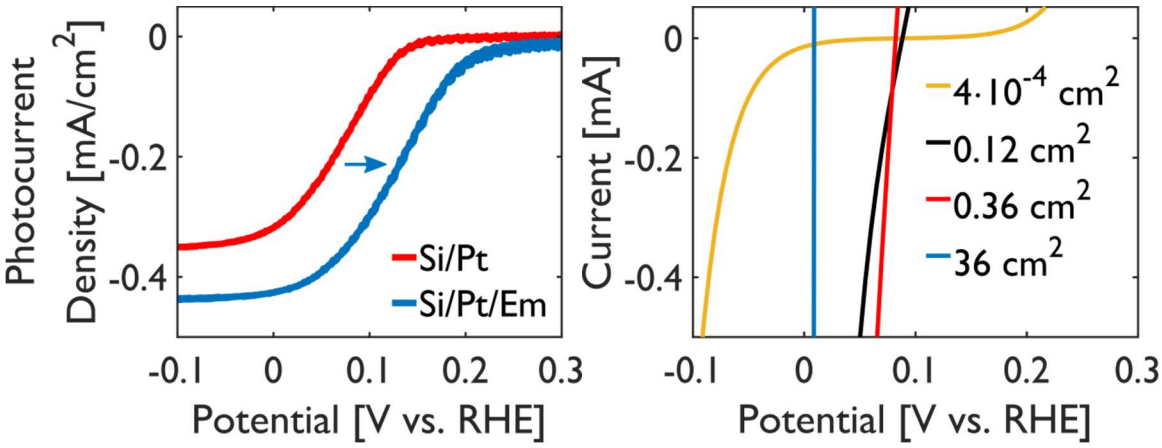

Figure 6.1: Onset potential shifts on Si/Pt electrodes (Left) Photocurrent vs. potential measurements for the Si/Pt electrodes discussed in Chapter 5. The Si/Pt electrode has Pt nanoparticles on the surface and the Si/Pt/Em electrode has the Pt particles embedded into the Si. The arrow designates the 0.06 V shift in the onset potential observed upon embedding the Pt. (Right) Plots for the modeled Butler-Volmer kinetics for different Pt areas on a Si electrode generating 0.35 mA/cm^2 of photocurrent. The projected area is 1 cm^2, so current and current density are equivalent in this case.

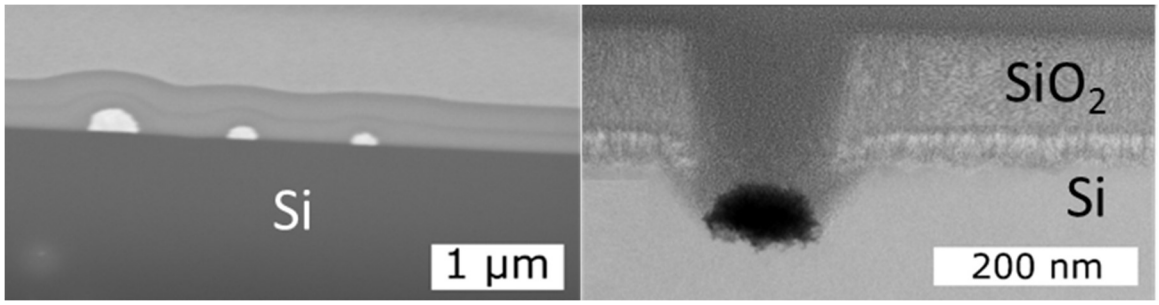

Figure 6.2: Electron microscopy analysis of Si/Pt interfaces (Left) Cross-sectional SEM image of the Si/Pt surface. There is no apparent alteration of the surface beyond adding the Pt particles. (Right) The Pt particle is embedded into the Si, but a layer of SiO_2 about 100 nm thick has formed on the surface. The Si/Pt interface does not appear to be oxidized based on this image and the EDS maps shown in Chapter 5.

performed on this electrode and an identical, but non-oxidized, electrode to determine the relationship between applied potential and current. The resulting current density (j) was then converted to kinetic current density (j_k) to remove effects caused by differences in the light-limited current density (j_L). Kinetic current is a measure of the rate of reaction on the catalyst surface in the absence of diffusion limitations. In this particular application, the diffusion limitation for which this correction is being made is the rate at which useful electrons arrive at the Pt catalyst. This conversion is performed using the Koutecky-Levich equation (Equation 6.1).

6.1 $$j_k = (1/j - 1/j_L)^{-1}$$

The results from this analysis are shown in the top panel of Figure 6.3. A kinetic current density of -0.1 mA/cm^2 for the non-oxidized Si/Pt electrode is achieved at 0.1 V vs. RHE. When the surface is oxidized, a kinetic current density of -0.1 mA/cm^2 is observed at 0 V vs. RHE. This represents a loss of efficiency induced by the oxidation of the electrode, which is the opposite of the trend seen with the embedded Pt electrode.

The reason for this opposite trend is that the oxidation process likely causes SiO_2 formation at the Si/Pt interface when the particle is not embedded. Cross-sectional SEM and EDS mapping needs to be performed to confirm this. However, there is previous work that supports this claim.[3,4] This work demonstrated that Pt nanoparticles, embedded into Si using the selective etching process, inhibit the oxidation of the Si at the Si/Pt interface by acting as a physical barrier to oxygen diffusion. When the Pt nanoparticles are not embedded, there is no barrier for the diffusion of oxygen into this interfacial region, causing it to oxidize. In both cases, the oxidation of the Si surface resulted in an

improvement of the onset potential, but when the Si/Pt interface became oxidized, the onset potential worsened. This result directly supports the observation from Figure 6.1.

The second experiment focused on the difference in onset potential between the as-prepared Si electrodes with embedded Pt (Si/Pt/Em) and Si/Pt/Em electrodes that were etched with 10 ml of 0.25 M HF for 2 minutes to remove the surface oxide grown during the embedding process (Si/Pt/Em/HF). Cyclic voltammetry was performed on these electrodes and the kinetic currents were calculated. This result is shown in the bottom panel of Figure 6.3. When the oxide surface is removed from a Si/Pt/Em electrode, the onset potential degrades relative to the Si/Pt/Em electrode.

These two sets of experiments give insight into the effect of oxidation on the onset potential. A thick insulating layer of SiO_2 formed at the Si/Pt interface prevents the passage of electrons from the Si into the Pt. More applied potential is then required to give the electrons the requisite energy to cross this barrier, resulting in hindered kinetic currents relative to non-oxidized interfaces. The improvement of the electrode onset potential occurs when the oxide is only present at the Si/electrolyte interface. In Chapter 2, the concept of Fermi level pinning was introduced as an interfacial phenomenon that is caused by a high density of surface states on the SC at the SC/electrolyte interface. Si typically is subject to this mechanism as a result of its covalent bonds.[5–8] The oxidation of these dangling Si bonds has been demonstrated to improve the barrier height of Si photoelectrodes by passivating these surface states.[9–12] The transformation of the surface allows the barrier height to be more dependent on the electrolyte Fermi level instead of the surface states. Since the barrier height at the Si/electrolyte interface is improved, and an efficient, non-oxidized path for electrons to reach the catalyst is preserved, the effective

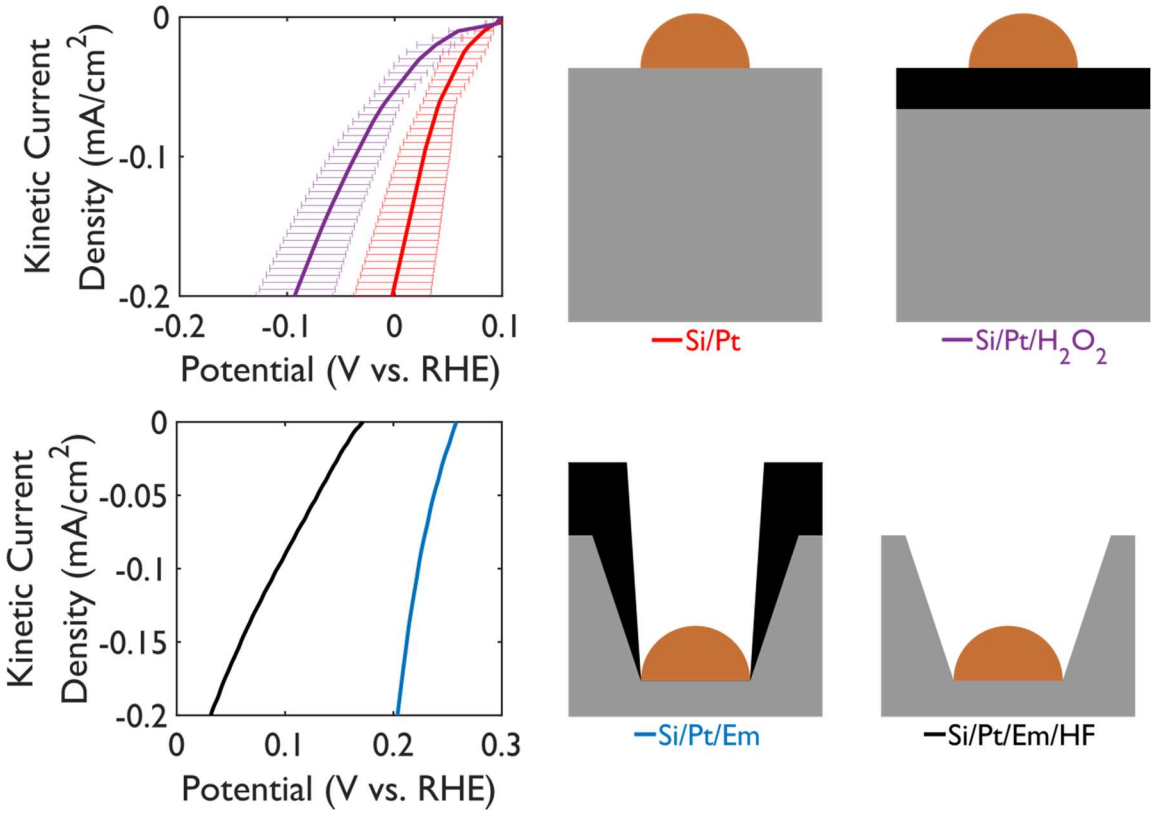

Figure 6.3: Si/Pt oxidation and etching experiments (Top) Kinetic current densities for Si electrodes with Pt loaded onto the surface. The red plot shows an as-prepared Si/Pt electrode while the purple plot shows a Si/Pt electrode treated with hydrogen peroxide. The oxidation of the entire Si interface is expected to be the cause of the loss of efficiency. (Bottom) Kinetic current densities for Pt embedded into Si (Si/Pt/Em, blue) and HF-etched Si/Pt/Em (Si/Pt/Em/HF, black) electrodes. The schematics to the right show the expected surfaces for each electrode. The gray areas are Si, the black are SiO_2, and the orange are Pt.

barrier height at the Si/Pt interface, which is also dependent on the pinch-off effect, is improved for the embedded Pt electrodes.

6.3 P-N Junction Si/Pt Devices

The oxidation of the Si at the Si/electrolyte interface is a potential route for improving the barrier height of the system, but the overall gains are modest. A more deliberate and impactful way to improve the interface to achieve higher efficiency is to use a p-n junction.

6.3.1 P-N Junctions

As mentioned in Chapter 2, the use of a p-n junction makes the barrier height of the system independent of the electrolyte equilibrium potential. There is evidence that suggests the barrier height also becomes independent of surface oxidation and the work function of metals at the original interface. Instead, the barrier height is dependent on the dopant concentration in the n-type layer of the p-n device. As this concentration increases, the difference in potential between the Fermi level and VB at the interface increases. The theoretical maximum barrier height of the system is equal to the band gap of the SC, which would occur when the dopant concentration is very high. Previous work using p-n junctions in Si photocathodes has shifted the onset potential to as high at 0.5 V vs. RHE.[13–15] This is a significant improvement relative to the 0.1-0.2 V vs. RHE onset potential for the Si/Pt/Em electrodes shown in Chapter 5.

The p-type Si used for this work has a resistivity of 2.5-2.6 Ω·cm. This corresponds to a boron dopant concentration of about $5.5 \cdot 10^{15}$ cm^{-3}. The n-type layer was formed to create a junction depth near 500 nm with a phosphorus dopant concentration around

$1 \cdot 10^{18}$ cm^{-3}. No doping profiles were collected, so these are just approximate values based on diffusion doping recipes available at the LNF.

6.3.2 Combining with Embedded Pt

The Diode/Butler-Volmer model discussed in Chapter 4 identified three parameters that are important for developing efficient photoelectrodes: surface reaction rate, photocurrent, and barrier height. The goal of this work is to build upon the improvements observed upon embedding Pt into the Si. This was discussed in Chapter 5 and was demonstrated to simultaneously provide a reactive surface for the HER, while also limiting optical losses through reflection and parasitic absorption by the Pt nanoparticle co-catalysts. The addition of a p-n junction to this electrode design is intended to improve the barrier height while maintaining the enhancements previously observed.

The results of PEC characterization of these electrodes are shown in Figure 6.4. The top panel shows that the limiting photocurrent is still improved upon embedding Pt into the pn-Si. The onset potential, defined by the half-wave potential, is 0.22 V vs. RHE for the Si/Pt electrode and 0.19 V vs. RHE for the embedded electrode. This is an improvement upon the work in Chapter 5, but the trend in onset potential change upon embedding Pt that was discussed in Section 6.2 is not observed. Without the p-n junction, the barrier height is dependent on the Si/electrolyte interface conditions. The bottom panel of Figure 6.4 illustrates this effect. With a p-n junction, the onset potential becomes slightly worse upon embedding.

6.3.3 COMSOL Calculations

Calculations were performed to clearly explain why the onset potential becomes worse upon embedding the Pt nanoparticles in to the p-n Si electrodes. In practice, the

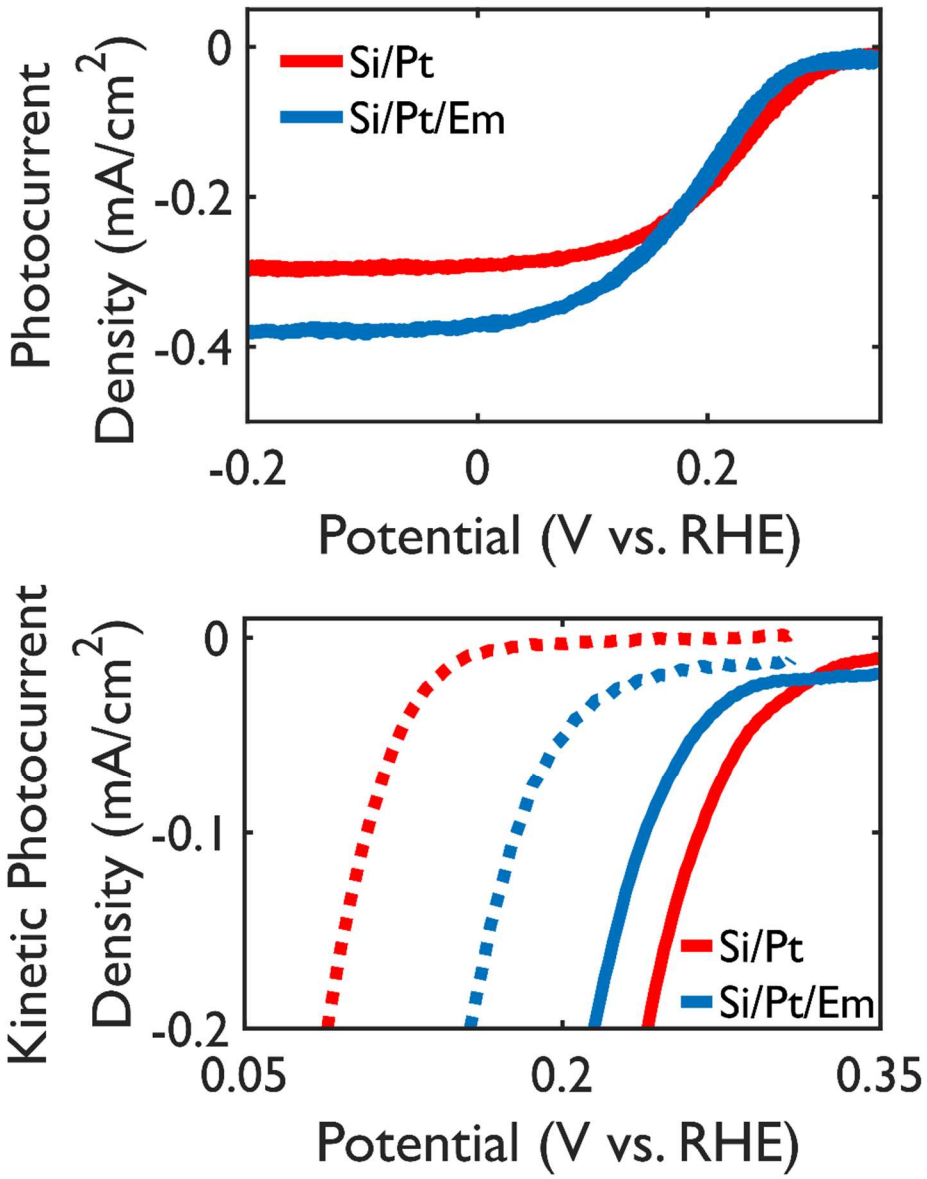

Figure 6.4: Photoelectrochemical characterization of pn-Si photoelectrodes loaded with Pt (Top) CV measurements for pn-Si with Pt nanoparticles on the surface (red) and embedded Pt nanoparticles (blue). (Bottom) Kinetic photocurrent densities for the pn-Si/Pt and pn-Si/Pt/Em electrodes (solid curves) and the p-type Si/Pt and Si/Pt/Em electrodes (from Chapter 5, dashed curves). All measurements were taken under 690 nm illumination.

doping of phosphorus into the top of the Si electrodes does not produce a consistent dopant concentration as a function of depth into the Si. The method of doping used creates a high doping concentration at the Si surface and decreases with depth into the Si. To mimic the expected experimental conditions, the acceptor doping concentration in the entire system was $1 \cdot 10^{16}$ cm^{-3} and the donor doping concentration in the first 10 nm of the Si slab was set to $1 \cdot 10^{18}$ cm^{-3}. Beyond this depth, the donor concentration was set to have an error function dependence on depth. The junction depth, which is the depth where the acceptor and donor concentrations are equal, was set to 500 nm. This dopant profile is shown in the top panel of Figure 6.5.

In these calculations, ohmic contact boundary conditions were applied to the front and back of the pn-Si system. To investigate the effect of making an embedded contact, the ohmic contact at the n-type surface was placed at different depths relative to the junction depth. The shape and position of the VB was calculated relative to the Fermi level for each depth to determine the expected barrier heights.

The bottom panel of Figure 6.5 and Table 6.1 show the outcome of these calculations. As the embedding depth increases, the barrier height decreases using the standard doping approach. This is because the donor concentration fades quickly into the Si. Based on the uncertainty involved in the experimental diffusion steps, it is plausible that the barrier height could be reduced significantly. The -0.03 V shift in onset potential observed can be explained by the calculated change in barrier height of 0.06 V. To overcome this issue, the concept of δ-doping can be used. This process differs from the method described in Chapter 3 in that is uses short, high-temperature exposure to dopant atoms over several cycles to achieve a homogeneous doping profile. The top panel of

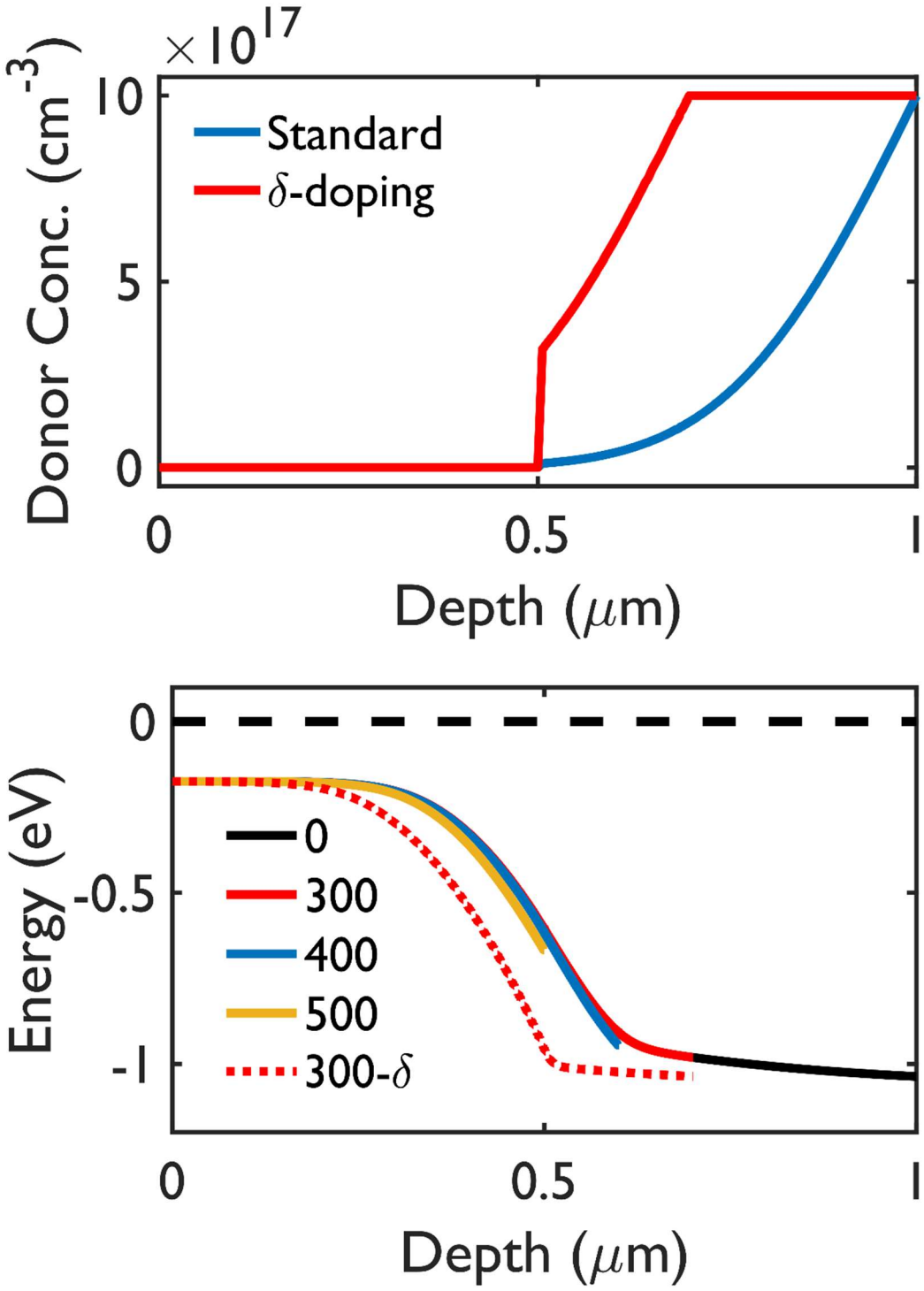

Figure 6.5: COMSOL conditions and calculation results for evaluating pn-Si barrier heights. (Top) Doping profiles for a method similar to the experimental doping (Standard) and for a potential δ-doping approach. (Bottom) Valance band energies calculated for different contact depths (in nm) into the Si. The dashed curve shows the δ-doping VB at a 300 nm contact depth.

Figure 6.5 suggests a potential δ-doping profile. With this type of profile, the loss of barrier height upon embedding could be significantly mitigated. Table 6.1 indicates that this δ-doping approach prevents the loss of barrier height at a depth of 300 nm relative to the standard doping approach at 0 nm.

Table 6.1: Calculated barrier heights for different contact depths in p-n Si.

Contact Depth (nm)	0	300	400	500	300-δ
Barrier Height (V)	1.04	0.98	0.95	0.67	1.04

6.4 Conclusion

The embedding of Pt into a Si photocathode caused an unexpected improvement in the onset potential for the HER. The Diode/Butler-Volmer model was used to rule out the influence of a change in Pt surface area and photocurrent. Instead, the barrier height was determined to be the only parameter capable of inducing such a change. PEC experiments were performed and strongly suggest that the formation of an oxide layer at the Si/electrolyte interface, but not at the Si/Pt interface increases the barrier height, which improves the onset potential. To more effectively exploit the barrier height to improve the onset potential, a thin n-type layer was formed at the Si/electrolyte interface. When combined with the embedded Pt nanoparticles, the barrier height, photocurrent, and reactive surface area were improved simultaneously. A small loss of barrier height was observed upon embedding the Pt because of the non-homogenous doping profile. A method called δ-doping is suggested as a means of avoiding this problem.

6.5 References

(1) Huang, Z.; Geyer, N.; Werner, P.; de Boor, J.; Gösele, U. Metal-Assisted Chemical Etching of Silicon: A Review. *Adv. Mater.* **2011**, *23* (2), 285–308.

(2) Mikhael, B.; Elise, B.; Xavier, M.; Sebastian, S.; Johann, M.; Laetitia, P. New Silicon

Architectures by Gold-Assisted Chemical Etching. *ACS Appl. Mater. Interfaces* **2011**, *3* (10), 3866–3873.

(3) Zhao, Y.; Anderson, N. C.; Zhu, K.; Aguiar, J. A.; Seabold, J. A.; van de Lagemaat, J.; Branz, H. M.; Neale, N. R.; Oh, J. Oxidatively Stable Nanoporous Silicon Photocathodes with Enhanced Onset Voltage for Photoelectrochemical Proton Reduction. *Nano Lett.* **2015**, *15* (4), 2517–2525.

(4) Aguiar, J. A.; Anderson, N. C.; Neale, N. R. Revealing the Semiconductor–catalyst Interface in Buried Platinum Black Silicon Photocathodes. *J. Mater. Chem. A* **2016**, *4* (21), 8123–8129.

(5) Sun, K.; Shen, S.; Liang, Y.; Burrows, P. E.; Mao, S. S.; Wang, D. Enabling Silicon for Solar-Fuel Production. *Chem. Rev.* **2014**.

(6) Zhang, Z.; Yates, J. T. Band Bending in Semiconductors: Chemical and Physical Consequences at Surfaces and Interfaces. *Chem. Rev.* **2012**, *112* (10), 5520–5551.

(7) Bard, A. J.; Bocarsly, A. B.; Fan, F. R. F.; Walton, E. G.; Wrighton, M. S. The Concept of Fermi Level Pinning at Semiconductor/liquid Junctions. Consequences for Energy Conversion Efficiency and Selection of Useful Solution Redox Couples in Solar Devices. *J. Am. Chem. Soc.* **1980**, *102* (11), 3671–3677.

(8) Zandi, O.; Hamann, T. W. Enhanced Water Splitting Efficiency Through Selective Surface State Removal. *J. Phys. Chem. Lett.* **2014**, 140410164458007.

(9) Rosenbluth, M. L.; Lieber, C. M.; Lewis, N. S. 630-mV Open Circuit Voltage, 12% Efficient N-Si Liquid Junction. *Appl. Phys. Lett.* **1984**, *45* (4), 423–425.

(10) Sheng, J.; Fan, K.; Wang, D.; Han, C.; Fang, J.; Gao, P.; Ye, J. Improvement of the SiOx Passivation Layer for High-Efficiency Si/PEDOT:PSS Heterojunction Solar Cells. *ACS Appl. Mater. Interfaces* **2014**, *6* (18), 16027–16034.

(11) Muñoz, A. G.; Lewerenz, H. J. Advances in Photoelectrocatalysis with Nanotopographical Photoelectrodes. *ChemPhysChem* **2010**, *11* (8), 1603–1615.

(12) Lewerenz, H. J.; Skorupska, K.; Muñoz, A. G.; Stempel, T.; Nüsse, N.; Lublow, M.; Vo-Dinh, T.; Kulesza, P. Micro- and Nanotopographies for Photoelectrochemical Energy Conversion. II: Photoelectrocatalysis – Classical and Advanced Systems. *Electrochim. Acta* **2011**, *56* (28), 10726–10736.

(13) Boettcher, S. W.; Warren, E. L.; Putnam, M. C.; Santori, E. A.; Turner-Evans, D.; Kelzenberg, M. D.; Walter, M. G.; McKone, J. R.; Brunschwig, B. S.; Atwater, H. A.; et al. Photoelectrochemical Hydrogen Evolution Using Si Microwire Arrays. *J. Am. Chem. Soc.* **2011**, *133* (5), 1216–1219.

(14) Seger, B.; Laursen, A. B.; Vesborg, P. C. K.; Pedersen, T.; Hansen, O.; Dahl, S.; Chorkendorff, I. Hydrogen Production Using a Molybdenum Sulfide Catalyst on a Titanium-Protected n^+p^- Silicon Photocathode. *Angew. Chemie Int. Ed.* **2012**, *51* (36),

9128–9131.

(15) Seger, B.; Pedersen, T. Using TiO_2 as a Conductive Protective Layer for Photocathodic H_2 Evolution. *J. Am. Chem. Soc.* **2013**, *135* (3), 1057–1064.

CHAPTER 7

Future Directions and Conclusions

7.1 Future Directions

7.1.1 Direct Characterization of the Si/Pt/Em and Interface

In Chapter 6, the improvement of the onset potential upon embedding the Pt nanoparticles into the Si was strongly suggested to be caused by the oxidation of the Si at the Si/electrolyte interface while the Si/Pt interface was unchanged. To confirm this, conductive atomic force microscopy (C-AFM) could be performed.

C-AFM is able to determine the topography of a surface while also applying a potential across the material at specific topographical features to characterize the local interfacial properties. The applied potential generates a current, which is measured. By analyzing this current over a range of potentials and at different locations on the Si/Pt and Si/Pt/Em electrodes, the barrier heights could potentially be directly measured through the Pt and SiO_2 regions.

Cross-sectional SEM imaging and EDS mapping of the Si/Pt/H_2O_2 electrodes also needs to be done to confirm that the Si is oxidized over the entire Si surface and at the Si/Pt interface when the Pt is on the surface and not embedded.

7.1.2 Pt Nanoparticle Size and Coverage

A typical Si/Pt electrode in this dissertation featured Pt nanoparticles of an average diameter of 150 nm covering about 6% of the Si surface, resulting in about 0.12 cm^2 of Pt

per cm^2 of projected electrode area. Based on the modeling work, the optimal surface area is closer to 0.36 cm^2 of Pt per cm^2 of projected electrode area. The size of these nanoparticles is also an issue because the surface area to volume ratio is fairly small. Additionally, the reflectance of the texturized Si (embedded Pt) was only reduced to about 15%. Both of these issues could be solved through the deposition of smaller Pt particles with a higher overall coverage.

If the coverage by Pt is increased and smaller particles are used, the Si surface will contain more pores that have smaller diameters. Chapter 5 explains that the small pore diameter relative to the incident wavelengths is the source of reduced parasitic absorption while the texturing reduces the reflectance. If this pore diameter is decreased and the surface roughness is increased, the quantum efficiency of the device could improve. Figure 7.1 shows 2D FDTD calculations supporting this idea.

In this dissertation research, the Pt nanoparticles were formed on the Si surface using an electroless deposition method. This was a very quick and reproducible approach, which was great for this focus of this work, but is not convenient for controlling the size and number density of particles on the Si. In the future, a reversed micelle electroless deposition method[1–3] or deposition via nanosphere lithography[4,5] could be used. The reversed micelle method is very similar to the electroless deposition method used, except the deposition solution is a mixture of the aqueous HF and metal precursor phase, a surfactant, and a nonpolar phase. The aqueous phase is contained in the reversed micelles,

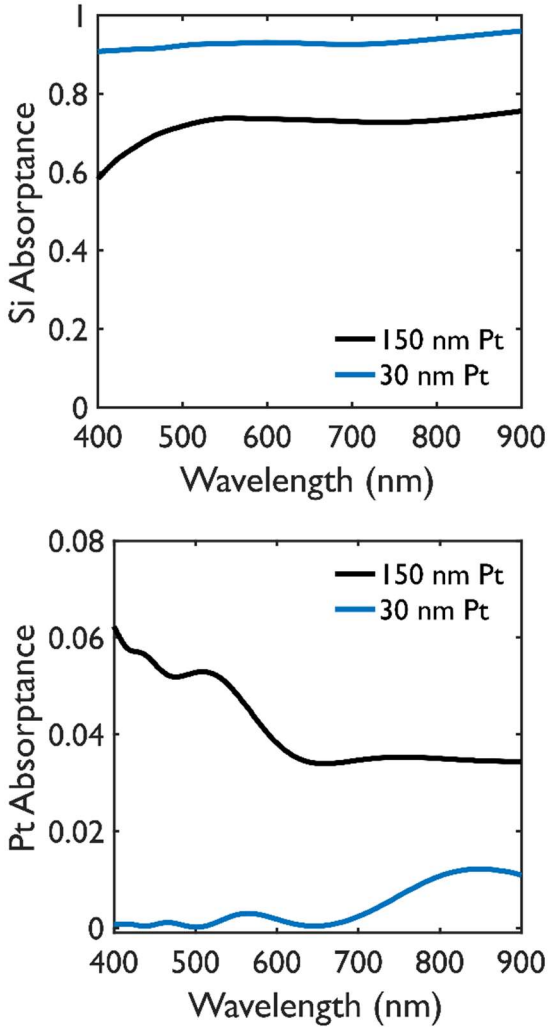

Figure 7.1: 2D FDTD calculations for Si with embedded Pt. The pores are 375 nm deep into the Si. The Pt and pore sizes are 150 nm (black) and 30 nm (blue). The Pt coverage is 28% and 40% for the 150 nm and 30 nm Pt, respectively.

with diameters that are determined by the surfactant concentration. The particle diameter is then directly related to the reversed micelle diameter. Small reversed micelles could be used to make small Pt nanoparticles. With nanosphere lithography, a monolayer of polystyrene nanoparticles is coated onto the Si. The metal is then evaporated onto the surface, covering the polystyrene but also depositing into the void spaces between the nanoparticles. The polystyrene spheres are then removed, leaving an ordered array of metal nanoparticles. The metal particle diameters are controlled by the diameters of the polystyrene spheres. Both of these methods are capable of producing nanoparticles with diameters as small as 40 nm.

7.2 Overall Conclusions

The primary focus of this dissertation was to explain how the different components of a photoelectrode, such as the absorbing semiconductor and co-catalytic materials should be integrated to maximize the efficiency of the device. A thorough analysis of a general photoelectrochemical system was performed through the use of the Diode/Butler-Volmer model. From this model, the catalytic activity and surface area, barrier height, and photocurrent were determined to be the key parameters governing the performance of photoelectrochemical devices.

The simple model system of single crystal p-type Si with Pt electrocatalysts for the hydrogen evolution reaction was used, not because it is the most practical system, but because it is a very stable and well understood system that is ideal for optimizing the integration of components that are very efficient for their particular roles. Silicon tends to absorb visible light at depths that do not result in high rates of bulk recombination, but reflects a high percentage of the incoming light and is a poor hydrogen evolution catalyst.

Pt nanoparticles are great at driving the hydrogen evolution reaction, but induce strong parasitic absorption and form low barrier height contacts with Si.

The optimization of these specific limitations was achieved simultaneously. The poor activity of the Si surface was rendered unimportant by incorporating Pt nanoparticles on the surface. The optical inefficiencies from Si and Pt were reduced by embedding the Pt nanoparticles into the Si, reducing the reflection and parasitic absorption losses. These systems were then also built on p-n Si to decouple the barrier height from the Si/electrolyte and Si/Pt interfaces.

The conclusions from this work can be applied to various composite semiconductor/metal photoelectrochemical devices. Similar analyses with cheaper materials could demonstrate their applicability for photocatalytic water splitting. Additionally, the OER component of these systems particularly suffers from poor reaction kinetics. The strategies demonstrated in this dissertation could be used to help compensate for these losses while parallel research continues to develop more efficient OER catalysts. Optimized HER and OER components maybe be combined with, ideally, enough photovoltage to drive the splitting of water at reasonable rates. With this achievement, a sustainable method of hydrogen production may be realized.

7.3 References

(1) Magagnin, L.; Bertani, V.; Cavallotti, P. L.; Maboudian, R.; Carraro, C. Selective Deposition of Gold Nanoclusters on Silicon by a Galvanic Displacement Process. *Microelectron. Eng.* **2002**, *64* (1–4), 479–485.

(2) Lombardi, I.; Marchionna, S.; Zangari, G.; Pizzini, S. Effect of Pt Particle Size and Distribution on Photoelectrochemical Hydrogen Evolution by P-Si Photocathodes. *Langmuir* **2007**, *23* (24), 12413–12420.

(3) Carraro, C.; Maboudian, R.; Magagnin, L. Metallization and Nanostructuring of Semiconductor Surfaces by Galvanic Displacement Processes. *Surf. Sci. Rep.* **2007**, *62*

(12), 499–525.

(4) Rossi, R. C.; Lewis, N. S. Investigation of the Size-Scaling Behavior of Spatially Nonuniform Barrier Height Contacts to Semiconductor Surfaces Using Ordered Nanometer-Scale Nickel Arrays on Silicon Electrodes. *J. Phys. Chem. B* **2001**, *105* (49), 12303–12318.

(5) Hulteen, J. C.; Duyne, R. P. Van. Nanosphere Lithography: A Materials General Fabrication Process for Periodic Particle Array Surfaces. *J. Vac. Sci. Technol. A Vacuum, Surfaces, Film.* **1995**, *13* (3), 1553.

APPENDIX A

PEC Data Analysis MATLAB Codes

A.1 Introduction

The following sections describe the codes used in MATLAB to convert the raw files generated by the potentiostat into the data presented in this dissertation. These codes will be stored on the Linic Group Wiki for access in the future.

A.2 Converting DTA to TXT Files (pstatdata2.m and pstatdataMS.m)

These scripts convert DTA files, which are generated by Gamry potentiostats, into TXT files. They must be executed in the folder where the DTA files exist and produces the corresponding TXT files at the same location. The script *pstatdata2.m* creates an individual TXT file for each CV cycle performed. This script is also used to convert CA files into TXT files. The script *pstatdataMS.m* is used to create TXT files for Mott-Schottky data processing and other electrochemical impedance measurements.

A.3 Plotting CV Data (siimport.m)

This script must be executed in the directory containing the TXT files generated by *pstatdata2.m*. This script plots the current-potential curves for each TXT file in the directory. The variables *electrode area*, *Ref*, and *pH* correspond to the illuminated electrode area, the potential of the reference electrode, and the electrolyte pH, respectively. These must be set according to the experimental conditions.

A.4 Plotting CA Data (pstatdatachrono.m)

This script must be executed in the directory containing the TXT files generated by *pstatdata2.m*. This script plots the current-potential curves for each TXT file in the directory. The variables *electrode area*, *Ref*, and *pH* correspond to the illuminated electrode area, the potential of the reference electrode, and the electrolyte pH, respectively. These must be set according to the experimental conditions.

A.5 Generating Photocurrent vs. Wavelength Plots (photocenhplotavg.m)

After the process described in Subsection 3.5.2 and Figure 3.8 is complete for all wavelengths for a given plot, this code is executed to plot the light-limited photocurrent vs. the wavelength. The wavelengths used must match those specified in the *wave* parameter. The *deltime* parameter is the minimum time (in seconds) between data points that must exist for the code to recognize a change from light to dark or dark to light. If there are gaps in the data that are longer than this specified time where there are no changes in the illumination condition, the code will not operate properly. This code must be run while the data of interest is selected in the plot.

A.6 Plotting Mott-Schottky Data (msimport.m)

This script must be executed in the directory containing the TXT files generated by *pstatdataMS.m*. This script plots the C^{-2} vs. potential curves for each TXT file in the directory. The variables *electrode area*, *Ref*, and *pH* correspond to the illuminated electrode area, the potential of the reference electrode, and the electrolyte pH, respectively. These must be set according to the experimental conditions. This script can be easily changed to plot other electrochemical impedance results, such as the real and imaginary impedance and the frequency, by commenting and uncommenting the appropriate lines 93 through 102.

APPENDIX B

Optical Calculation Codes

B.1 Introduction

The following sections describe the codes used for calculations involving MEEP. These codes will be stored on the Linic Group Wiki for access in the future.

B.2 Calculation Structure

This code collection is a series of scripts that are nested inside of each other. The master script is *prepper*. It creates a folder with a name based on the *DIRD* variable and copies all the calculation files into that folder. It also submits the job to the cluster queue to run using the command *sbatch shell_script.slurm*. This slurm file is used to specify the number of nodes and processors used for the calculation. The product of *–N* and *--ntasks-per-node* should equal *MACHINE_COUNT* and generally be a multiple of 20.

The slurm file runs the script *meeper*, which sets all the geometry parameters for the calculation. The variable *i* is used in a loop to dictate the wavelengths studied. When this variable is 1, 2, or 3, the wavelength ranges are 300-350 nm, 350-370 nm, and 370-900 nm, respectively. This was done to allow the usage of different DL models to capture the optical properties of Si adequately. The *fieldcalc* variable is set to *0* if no field calculations are needed and *1* if they are needed. *Slab*, *agrad*, *subfrac*, *hemi*, and *per* specify the thickness of the Si, the radius of the metal nanoparticle (Pt by default), whether the particle is hemispherical or not (0 for no, 1 for yes), and whether the simulation is periodic or not (0 for no, 1 for yes). The *hemi* and *per* parameters should not be changed unless you know what you are doing, especially regarding its effects on the control file. This code passes all

these parameters to the three separate MEEP calculations (to get absorption and scattering information) and then runs the post-processing octave scripts (the *.m* files).

The control file (*silver_sphere.ctl*) is written in the Scheme language and is what directly interacts with the MEEP software. It takes all the parameters from *meeper* and sets up the simulation. The first 50+ lines of the code take the parameters and convert them into quantities that allow for the mathematical definition of the structure and set up various settings for the calculation. The next 50 lines contain the DL material codes. This is where the output from *meepformat.m* (Section B.3) goes. The rest of the code sets up the geometry, the flux monitors, and the field calculations. These concepts can be studied at the MEEP reference webpage (http://ab-initio.mit.edu/wiki/index.php/Meep_Reference).

B.3 Fitting for Optical Data to DL (fittingformeepNK.m and meepformat.m)

This code is used to take TXT files from the *Optical Data* directory located in the *fittingformeep* directory that are wavelength (in nm) vs. refractive index data (e.g., *si_n.txt* and *si_k.txt* are the real and imaginary refractive index components for Si from Green[2]), convert them to the corresponding dielectric function data, and then fit the desired model to the data. Several models are included, but the Drude and Lorentz models are the defaults. Lines 36, 39, and 40 can be used to add constraints to the parameter values. Line 58 is used to specify the number of terms as the variable *terms_num*. This is a list of 5 numbers. The first should always be set to 1, and the second and fifth numbers correspond to the Debye and a modified Lorentz model, respectively. These should be kept at 0. The third number sets the number of Drude terms and the fourth digit sets the number of Lorentz terms. Lines 63 and 64 are used to set the minimum and maximum wavelengths (in nm). The specific refractive index files to be used are set in lines 67 and 68. This code

searches for the optimum result and outputs the Drude and Lorentz parameters to be used.

MEEP operates without units, so the parameters must be transformed by dimensionless numbers to be useful. The parameters from the fitting code must be inserted into the appropriate arrays (lines 9 through 17). The name of the material and the wavelength range should be specified in line 7 to give a means of identifying the specific set of parameters. Running this code produces a TXT files that presents the dimensionless parameters in language that MEEP can understand. This text is inserted into the MEEP control file (*sphere_silver.ctl*).

B.4 Visualizing the Simulation Geometry (geomplot2.m)

MEEP can be difficult to use because there is no graphical interface to know what structure is being analyzed. This MATLAB code uses a similar structure as the geometry definitions in *silver_sphere.ctl* to generate a plot of the geometry. This code is extremely helpful for troubleshooting when a new type of geometry is being mathematically constructed.

B.5 References

(1) Green, M. A.; Keevers, M. J. Optical Properties of Intrinsic Silicon at 300 K. *Prog. Photovoltaics Res. Appl.* **1995**, *3* (3), 189–192.

APPENDIX C

Absorption/Recombination Model

C.1 Introduction

The following section contains the MATLAB code used for the Absorption/Recombination model. This code will also be stored on the Linic Group Wiki for access in the future.

C.2 MATLAB Code

```
%This model estimates the effecet of a perfect plasmonic particle,
%parasitic particle, or 50/50 particle in a SC slab. The optical properties
%of this slab are currently based on the absorption depths and reflectivity
%of Silicon. The minority charge carrier diffusion length, slab thickness,
%and particle depths are set below. This model assumes that the space
%charge layer thickness is negligible, that there is no internal
%reflectance in the SC, and that metal particles do not affect the
%reflectivity of the SC surface.

clear all
SC=1; %(1=silicon, 2=TiO2 3=BiVO4)
%Si valid from 300-900, TiO2 from 180-390, BiVO4 from 303 to 697 nm
particles=[0 1 2 3];
%ABOVE LINE: 0: no particle, 1: SPR particle, 2: parasitic particle 3: half s-p KEEP
AS AN ARRAY.
lamin=[300,250,303]; %MIN WAVELENGTH (NM)
lamax=[900,350,675]; % MAX WAVELENGTH (NM)
lamin=lamin(SC);
lamax=lamax(SC);
del=5; %WAVELENGTH SPACING (NM)

pdep=500; %PARTICLE DEPTH MICRONS
%ediff=100% microns
%Si: 100-400 microns, TiO2 10nm, BiVO4 100nm
maxx=500; %THICKNESS OF THE SC SLAB IN MICRONS
%pdep=ediff/2; %DEPTH OF THE PARTICLE IN MICRONS
%pdep=10/1000; %DEPTH OF THE PARTICLE IN MICRONS
rdel=1; %fraction of original refl remaining
rfrac=1; %fractional refl (if 1, not used)
medium=1.33; %air 1 water 1.33 (OTHER VALUES WON'T WORK)

lam=lamin:del:lamax; %nm

for aa=particles
```

```
    if SC==1 %properties for Si
        ediff=100; %CHARGE CARRIER DIFFUSION LENGTH MICRONS

absdepth=[250,0.0054348;260,0.0050761;270,0.0045872;280,0.0042373;290,0.0044643;300,
0.0057803;310,0.0069444;320,0.0078125;330,0.008547;340,0.0091743;350,0.0096154;360,0
.0098039;370,0.014347;380,0.03413;390,0.066667;400,0.10504;410,0.14837;420,0.2;430,0
.2551;440,0.32154;450,0.39216;460,0.47619;470,0.5814;480,0.67568;490,0.7874;500,0.90
09;510,1.0309;520,1.1364;530,1.2739;540,1.4184;550,1.5649;560,1.7301;570,1.8797;580,
2.0492;590,2.2272;600,2.4155;610,2.6247;620,2.8409;630,3.0581;640,3.2895;650,3.5587;
660,3.876;670,4.2017;680,4.5249;690,4.878;700,5.2632;710,5.6497;720,6.0241;730,6.493
5;740,7.0423;750,7.6923;760,8.4034;770,9.0909;780,9.901;790,10.776;800,11.765;810,12
.903;820,14.144;830,15.456;840,16.92;850,18.692;860,20.833;870,23.148;880,26.11;890,
29.155;900,32.68;910,36.765;920,41.667;930,47.619;940,54.645;950,63.694;960,74.627;9
70,87.719;980,104.28;990,126.26;1000,156.25;1010,195.69;1020,250.63;1030,331.13;1040
,442.48;1050,613.5;1060,900.9;1070,1250;1080,1612.9;1090,2127.7;1100,2857.1;1110,370
3.7;1120,5000;1130,6666.7;1140,10000;1150,14706;1160,23810;1170,45455;1180,153850;11
90,277780;1200,454550;1210,769230;1220,1219500;1230,2127700;1240,4166700;1250,100000
00;1260,27778000;1270,50000000;1280,83333000;1290,140850000;1300,222220000;1310,3703
70000;1320,625000000;1330,1250000000;1340,2857100000];
        %The above line sets the optical properties of the system to be Si by
        %specifying the absorption depth (inverse of the absorption coefficient).
        abd=absdepth;
        lightpowset=lam.';
        lightpowset(:,2)=1;
        lightpow(:,1)=lam;
        lightpow(:,2)=interp1(lightpowset(:,1),lightpowset(:,2),lam);
        if medium==1

reflset=[250,0.672612594;260,0.705174000;270,0.732089553;280,0.722956411;290,0.68423
5361;300,0.623487589;310,0.590475835;320,0.574130338;330,0.565677412;340,0.561749318
;350,0.565380276;360,0.582911002;370,0.584270801;380,0.546502292;390,0.510973644;400
,0.486021028;410,0.466853260;420,0.451521581;430,0.439123249;440,0.428907265;450,0.4
19585700;460,0.411485950;470,0.404281394;480,0.397879181;490,0.391964733;500,0.38710
5531;510,0.382264522;520,0.377999092;530,0.374142014;540,0.370428522;550,0.367335936
;560,0.364216221;570,0.361451749;580,0.358667135;590,0.356344975;600,0.354106672;610
,0.351853614;620,0.349785241;630,0.348201339;640,0.346411480;650,0.344713928;660,0.3
43309316;670,0.341798625;680,0.340281901;690,0.338962422;700,0.337639002;710,0.33641
3285;720,0.335285625;730,0.334257590;740,0.333329999;750,0.332400673;760,0.331468652
;770,0.330534830;780,0.329598359;790,0.328764393;800,0.328032868;810,0.327300306;820
,0.326671301;830,0.326041006;840,0.325409976;850,0.324777931;860,0.324144650;870,0.3
23510569;880,0.322875469;890,0.322239190;900,0.321602046;910,0.320963878;920,0.32032
4684;930,0.319684464;940,0.319150064;950,0.318615045;960,0.318079311;970,0.317542859
;980,0.317113181;990,0.316683043;1000,0.316252445];
            %above line: reflectance of Si in air (based on Fresnel equation)
        elseif medium==1.33

reflset=[250,0.601;260,0.637;270,0.666;280,0.653;290,0.606;300,0.535;310,0.497;320,0
.479;330,0.469;340,0.464;350,0.468;360,0.487;370,0.488;380,0.446;390,0.407;400,0.380
;410,0.360;420,0.344;430,0.331;440,0.320;450,0.311;460,0.302;470,0.295;480,0.289;490
,0.283;500,0.278;510,0.273;520,0.269;530,0.265;540,0.261;550,0.258;560,0.255;570,0.2
52;580,0.250;590,0.247;600,0.245;610,0.243;620,0.241;630,0.239;640,0.238;650,0.236;6
60,0.235;670,0.233;680,0.232;690,0.231;700,0.229;710,0.228;720,0.227;730,0.226;740,0
.22500;750,0.22400;760,0.22300;770,0.22300;780,0.22200;790,0.22100;800,0.22000;810,0
.21900;820,0.21900;830,0.21800;840,0.21800;850,0.21700;860,0.21600;870,0.21600;880,0
```

```
.21500;890,0.21500;900,0.21400;910,0.213;920,0.213;930,0.212;940,0.212;950,0.211;960
,0.211;970,0.210;980,0.210;990,0.209;1000,0.209];
            %above line: reflectance of Si in water (based on Fresnel equation)
        end

    elseif SC==2 %properties for TiO2
        ediff=10/1000; %CHARGE CARRIER DIFFUSION LENGTH MICRONS

absdepth=[390,3103521.39000000;380,302394.391900000;370,0.892232257000000;360,0.1141
35019000000;350,0.0427967350000000;340,0.0247632620000000;330,0.0167286060000000;320
,0.0122668680000000;310,0.00902172900000000;300,0.00727776200000000;290,0.0065288330
0000000;280,0.00625784800000000;270,0.00626083;260,0.00647092700000000;250,0.0069870
9900000000;240,0.00778422400000000;230,0.00878254200000000;220,0.00969221300000000;2
10,0.0101280420000000;200,0.00938524300000000;190,0.00825672800000000;180,0.00716914
200000000];
        %The above line sets the optical properties of the system to be TiO2 by
        %specifying the absorption depth (inverse of the absorption coefficient).
        abd=absdepth;
        lightpowset=lam.';
        lightpowset(:,2)=1;
        lightpow(:,1)=lam;
        lightpow(:,2)=interp1(lightpowset(:,1),lightpowset(:,2),lam);
        if medium==1

reflset=[390,0.294727910000000;380,0.308466355000000;370,0.326000723000000;360,0.349
030091000000;350,0.411353192000000;340,0.460204877000000;330,0.496591655000000;320,0
.522450873000000;310,0.548251771000000;300,0.566023785000000;290,0.572360046000000;2
80,0.575902689000000;270,0.618973530000000;260,0.619924523000000;250,0.6014698110000
00;240,0.530200342000000;230,0.440275131000000;220,0.375770289000000;210,0.334404668
000000;200,0.339868120000000;190,0.372173934000000;180,0.429668638000000];
            %above line: reflectance of TiO2 in air (based on Fresnel equation)
        elseif medium==1.33

reflset=[390,0.188946739000000;380,0.201684403000000;370,0.218156913000000;360,0.238
594675000000;350,0.293716105000000;340,0.333726469000000;330,0.357907928000000;320,0
.365109877000000;310,0.353834073000000;300,0.314913977000000;290,0.235210633000000;2
80,0.186854653000000;270,0.0359079350000000;260,0.0101064600000000;250,0168663;240,0
146586;230,0.00164931;220,0.00138448200000000;210,0.00217109200000000;200,0.00515702
200000000;190,0.00511059300000000;180,0221646];
            %above line: reflectance of Si in water (based on Fresnel equation)
        end

    elseif SC==3 %properties for BiVO4
        ediff=100/1000; %CHARGE CARRIER DIFFUSION LENGTH MICRONS

absdepth=[303,0.0251119110;308,0.0254896860;313,0.0258611660;318,0.0262750970;323,0.
0266890540;328,0.0271125480;333,0.0276035390;338,0.0280429210;343,0.0285876670;348,0
.0292902110;353,0.0299328810;358,0.0307739470;363,0.0316298530;368,0.0326590540;373,
0.0337806230;378,0.0349137350;383,0.0361251530;388,0.0372357530;393,0.0382609330;398
,0.0391233720;403,0.0396928150;408,0.0401867660;413,0.0407639080;418,0.0415557930;42
3,0.0425083570;428,0.0440006980;433,0.0461158600;438,0.0495079550;443,0.0530661720;4
48,0.0575757680;453,0.0637741290;458,0.0714076570;463,0.0793221270;468,0.0895682520;
473,0.0999459050;478,0.112614515;483,0.125378892;488,0.141194129;493,0.156711612;498
,0.173217067;503,0.189955628;508,0.207655021;513,0.226350757;518,0.247268698;523,0.2
```

```
67211349;528,0.286849220;533,0.306448631;538,0.332935283;543,0.354130024;548,0.37907
1585;553,0.406298611;558,0.436082047;563,0.467831070;568,0.498255352;573,0.532747935
;578,0.573366617;583,0.612531445;588,0.654708517;593,0.698872831;598,0.759309776;603
,0.803075736;608,0.869850208;613,0.931207863;618,1.012243777;623,1.05255956;628,1.18
0114515;633,1.280386789;638,1.374025839;643,1.409379314;648,1.493792082;653,1.703085
832;658,1.736633847;663,1.790555033;668,1.93914288;673,2.135677329;678,2.276791278;6
83,2.650854878;688,3.162957154;693,3.545228521;697,4.793053088];
        %The above line sets the optical properties of the system to be Si by
        %specifying the absorption depth (inverse of the absorption coefficient).
        abd=absdepth;
        lightpowset=lam.';
        lightpowset(:,2)=1;
        lightpow(:,1)=lam;
        lightpow(:,2)=interp1(lightpowset(:,1),lightpowset(:,2),lam);
        if medium==1

reflset=[303,0.175210410;308,0.176984269;313,0.178932669;318,0.180735269;323,0.18261
4025;328,0.184480050;333,0.186215005;338,0.188315628;343,0.189930895;348,0.190914136
;353,0.192519502;358,0.193153376;363,0.193859878;368,0.193951932;373,0.193605780;378
,0.193350747;383,0.192904048;388,0.192537338;393,0.192224580;398,0.192762306;403,0.1
94100863;408,0.196159596;413,0.198854735;418,0.201951873;423,0.205179136;428,0.20798
5636;433,0.210121837;438,0.210391188;443,0.210855127;448,0.210254623;453,0.208811218
;458,0.206478596;463,0.204179163;468,0.200392586;473,0.197144426;478,0.193598110;483
,0.189522492;488,0.185927682;493,0.182614550;498,0.179398081;503,0.176312290;508,0.1
73487805;513,0.170573422;518,0.168206642;523,0.165940391;528,0.163681875;533,0.16179
7101;538,0.159869049;543,0.158423823;548,0.156855156;553,0.155176662;558,0.153716951
;563,0.152257713;568,0.150805148;573,0.149137185;578,0.148383183;583,0.146981989;588
,0.146179366;593,0.144692022;598,0.143359911;603,0.142231321;608,0.141260561;613,0.1
40560917;618,0.139711756;623,0.138814678;628,0.137936828;633,0.136893662;638,0.13613
5296;643,0.135122048;648,0.134046605;653,0.133695152;658,0.132845725;663,0.132112538
;668,0.131166678;673,0.130806124;678,0.130516238;683,0.129247330;688,0.128777816;693
,0.127700204;697,0.127230592];
            %above line: reflectance of Si in air (based on Fresnel equation)
        elseif medium==1.33

reflset=[303,0.0188958160000000;308,0.0207214330000000;313,0.0227098290000000;318,0.
0248593460000000;323,0.0270840550000000;328,0.0293477590000000;333,0.031898450000000
0;338,0.0344870800000000;343,0.0371430400000000;348,0.0399123600000000;353,0.0429007
460000000;358,0.0456819410000000;363,0.0484013010000000;368,0.0509835360000000;373,0
.0531883760000000;378,0.0552598380000000;383,0.0571399620000000;388,0.05859049400000
00;393,0.0597191860000000;398,0.0611796600000000;403,0.0626782200000000;408,0.064702
9420000000;413,0.0675432290000000;418,0.0712287660000000;423,0.0753125500000000;428,
0.0798701010000000;433,0.0845100330000000;438,0.0885739570000000;443,0.0922030070000
000;448,0.0949630450000000;453,0.0972251330000000;458,0.0983861960000000;463,0.09879
86320000000;468,0.0978506110000000;473,0.0967683880000000;478,0.0952958850000000;483
,0.0930204900000000;488,0.0910843010000000;493,0.0891191320000000;498,0.087114851000
0000;503,0.0851076900000000;508,0.0832478200000000;513,0.0812731170000000;518,0.0797
043180000000;523,0.0781572860000000;528,0.0765858340000000;533,0.0752802710000000;53
8,0.0739679220000000;543,0.0729711770000000;548,0.0718865600000000;553,0.07071620400
00000;558,0.0697063850000000;563,0.0686917040000000;568,0.0676713440000000;573,0.066
4945320000000;578,0.0659929240000000;583,0.0650073700000000;588,0.0644582490000000;5
93,0.0634074880000000;598,0.0624786270000000;603,0.0616839060000000;608,0.0610126040
000000;613,0.0605304080000000;618,0.0599441090000000;623,0.0593104220000000;628,0.05
87093260000000;633,0.0579813840000000;638,0.0574538670000000;643,0.0567389390000000;
```

```
648,0.0559871560000000;653,0.0557554760000000;658,0.0551592930000000;663,0.0546472820000000;668,0.0539924100000000;673,0.0537481220000000;678,0.0535499880000000;683,0.0526753940000000;688,0.0523569400000000;693,0.0516142540000000;697,0.0512965760000000
];
            %above line: reflectance of Si in water (based on Fresnel equation)
        end
    end

    refl(:,1)=lam;
    refl(:,2)=interp1(reflset(:,1),reflset(:,2),lam,'pchip');
    if aa>0
        refl(:,2)=refl(:,2)*rdel;
    end
    if ne(rfrac, 1)==1
        refl(:,2)=rfrac;
    end

    ad=interp1(absdepth(:,1),absdepth(:,2),lam,'pchip');
    abdd=interp1(absdepth(:,1),abd(:,2),lam,'pchip');

    clear depths
    % depths(1)=0;
    % %depths(2)=01;
    % depths(2)=maxx/10^7;
    % fac=15;
    % kk=3;
    % while depths(kk-1)<maxx/fac
    %     depths(kk)=depths(kk-1)*fac;
    %     kk=kk+1;
    % end
    depths(1)=0;
    for kk=2:1:32237
        depths(kk)=maxx/10^7*exp((kk-1)*(5*10^-4));
    end
    depths(kk+1)=maxx;
    tmp=sqrt((depths-pdep).^2);
    [idx idx]=min(tmp);
    pd=pdep;
    pdep=depths(idx);

    %no particle
    if aa==0
        for i=1:length(lam)
            for j=1:length(depths)
                absc(i,j)=1-1/exp(depths(j)/ad(i));
                recombc(j)=1-1/exp(depths(j)/ediff);
            end
        end
        for i=1:length(lam)
            abs(i,1)=0;
            recomb(1)=0;
            for j=2:length(depths)
                abs(i,j)=absc(i,j)-absc(i,j-1);
                recomb(j)=recombc(j)-recombc(j-1);
```

```
                col(i,j)=abs(i,j)*(1-recombc(j));
            end
        end
        abstot=absc(:,end);
    end

    %SPR particle
    if aa==1
        for l=1:length(depths)
            if depths(l)==pdep
                ll=l;
            end
        end
        for i=1:length(lam)
            for j=1:length(ll-1)
                absc(i,j)=1-1/exp(depths(j)/ad(i));
                recombc(j)=1-1/exp(depths(j)/ediff);
            end
            absc(i,ll)=1;
            recombc(ll)=1-1/exp(depths(ll)/ediff);
            for j=(ll+1):length(depths)
                absc(i,j)=absc(i,ll);
                recombc(j)=1-1/exp(depths(j)/ediff);
            end
        end
        for i=1:length(lam)
            abs(i,1)=0;
            recomb(1)=0;
            for j=2:length(depths)
                abs(i,j)=absc(i,j)-absc(i,j-1);
                recomb(j)=recombc(j)-recombc(j-1);
                col(i,j)=abs(i,j)*(1-recombc(j));
            end
        end
        abstot=absc(:,end)./absc(:,end);
    end

    %Parasitic particle
    if aa==2
        for l=1:length(depths)
            if depths(l)==pdep
                ll=l;
            end
        end
        for i=1:length(lam)
            for j=1:length(ll-1)
                absc(i,j)=1-1/exp(depths(j)/ad(i));
                recombc(j)=1-1/exp(depths(j)/ediff);
            end
            absc(i,ll)=absc(i,ll-1);
            recombc(ll)=1-1/exp(depths(ll)/ediff);
            for j=(ll+1):length(depths)
                absc(i,j)=absc(i,ll);
                recombc(j)=1-1/exp(depths(j)/ediff);
```

```
            end
        end
        for i=1:length(lam)
            abs(i,1)=0;
            recomb(1)=0;
            for j=2:length(depths)
                abs(i,j)=absc(i,j)-absc(i,j-1);
                recomb(j)=recombc(j)-recombc(j-1);
                col(i,j)=abs(i,j)*(1-recombc(j));
            end
        end
        abstot=absc(:,end)./absc(:,end);
    end

    %Half S/P particle
    if aa==3
        for l=1:length(depths)
            if depths(l)==pdep
                ll=l;
            end
        end
        for i=1:length(lam)
            for j=1:length(ll-1)
                absc(i,j)=1-1/exp(depths(j)/ad(i));
                recombc(j)=1-1/exp(depths(j)/ediff);
            end
            absc(i,ll)=(1+absc(i,ll-1))/2;
            recombc(ll)=1-1/exp(depths(ll)/ediff);
            for j=(ll+1):length(depths)
                absc(i,j)=absc(i,ll);
                recombc(j)=1-1/exp(depths(j)/ediff);
            end
        end
        for i=1:length(lam)
            abs(i,1)=0;
            recomb(1)=0;
            for j=2:length(depths)
                abs(i,j)=absc(i,j)-absc(i,j-1);
                recomb(j)=recombc(j)-recombc(j-1);
                col(i,j)=abs(i,j)*(1-recombc(j));
            end
        end
        abstot=absc(:,end)./absc(:,end);
    end


    for l=1:length(depths)
        if depths(l)==maxx
            index=l;
        end
    end

    for i=1:length(lam)
        colc(i,1)=0;
```

```
        for j=2:index
            colc(i,j)=colc(i,j-1)+col(i,j);
            photocs(i,j)=colc(i,j)*lightpow(i,2)*(1-refl(i,2));
        end
    end
    if aa==0
        base=photocs;
    end

    if aa==0
        colo=[0,0,0];
    elseif aa==1
        colo=[0,0.447,0.741];
    elseif aa==2
        colo=[1,0,0];
    elseif aa==3
        colo=[0.929,0.694,0.125];
    end


    zz=exist('figabs');
    if zz==0
        figabs=figure
        hold on
    else
        figure(figabs);
        hold on
    end
    hold on
    plot(lam(:),(lightpow(:,2).*(1-
refl(:,2)).*absc(:,index))./lightpow(:,2),'Color',colo,'LineWidth',4)
    box on
    xlabel('Wavelength (nm)');
    ylabel('Absorption Fraction','FontName','Gill Sans MT');
    xlim([lamin-5 lamax+5]);
    ax=gca;
    ww=ax.LineWidth;
    ax.LineWidth=2;
    set(gca,'fontsize',20)
    set(gca,'XTick',[300 500 700 900])
    axis square
    posy=get(gcf, 'Position');
    set(gcf, 'Position', [posy(1) posy(2) posy(4) posy(4)]);

    zz=exist('figphot');
    if zz==0
        figphot=figure
        hold on
    else
        figure(figphot);
        hold on
    end
    hold on
    plot(lam(:),photocs(:,end),'Color',colo,'LineWidth',4)
```

```
    box on
    xlabel('Wavelength (nm)');
    ylabel('External Quantum Efficiency','FontName','Gill Sans MT');
    xlim([lamin-5 lamax+5]);
    ax=gca;
    ww=ax.LineWidth;
    ax.LineWidth=2;
    set(gca,'fontsize',20)
    set(gca,'XTick',[300 500 700 900])
    axis square
    posy=get(gcf, 'Position');
    set(gcf, 'Position', [posy(1) posy(2) posy(4) posy(4)]);

%     zz=exist('figphotenh');
%     if zz==0
%         figphotenh=figure
%         hold on
%     else
%         figure(figphotenh);
%         hold on
%     end
%     hold on
%     plot(lam(:),photocs(:,end)./base(:,end),'Color',colo,'LineWidth',4)
%     box on
%     xlabel('Wavelength (nm)');
%     ylabel('Photocurrent Enhancement','FontName','Gill Sans MT');
%     xlim([lamin-5 lamax+5]);
%     ax=gca;
%     ww=ax.LineWidth;
%     ax.LineWidth=2;
%     set(gca,'fontsize',20)
%     set(gca,'XTick',[300 500 700 900])
%     axis square
%     posy=get(gcf, 'Position');
%     set(gcf, 'Position', [posy(1) posy(2) posy(4) posy(4)]);
%
%
%     zz=exist('figiqe');
%     if zz==0
%         figiqe=figure
%         hold on
%     else
%         figure(figiqe);
%         hold on
%     end
%     hold on
%     plot(lam(:),photocs(:,end)./((lightpow(:,2).*(1-
refl(:,2)).*abstot(:,end))./lightpow(:,2)),'Color',colo,'LineWidth',4)
%     box on
%     xlabel('Wavelength (nm)');
%     ylabel('Internal Quantum Efficiency','FontName','Gill Sans MT');
%     xlim([lamin-5 lamax+5]);
%     ylim([0-0.025 1+0.025]);
%     ax=gca;
```

```
%     ww=ax.LineWidth;
%     ax.LineWidth=2;
%     set(gca,'fontsize',20)
%     set(gca,'XTick',[300 500 700 900])
%     axis square
%     posy=get(gcf, 'Position');
%     set(gcf, 'Position', [posy(1) posy(2) posy(4) posy(4)]);
end
```

APPENDIX D

Diode/Butler-Volmer Model

D.1 Introduction

The following section contains the MATLAB code used for the Diode/Butler-Volmer model. This code will also be stored on the Linic Group Wiki for access in the future.

D.2 MATLAB Code

```
%This script runs the diode+butler-volmer model that Paul has developed. It
%starts with a diode cross sectional area of 1 cm^2 and computes the total
%surface roughness by accounting for the surface areas of hemispherical catalysts.
The hemispherical area is added to the original cross
%sectional area. Surface area can also be added through the inclusion of
%pores, which are tied to the Pt coverage and diameters. The depth of these
%pores must be specified to specify the total area added.

%only trust this script after you have gone through the entire contents and
understand it.
%the calculaions are wacky and hard to follow and definitely not optimized.

%1: The "run" variable dictates which things to plot. 0 plots the full
%model, 1 plots the diode component, 2 is the entire BV component for both
%materials, 3 is just for the silicon BV, 4 for just the Pt BV, 5 is the
%full model with not Eph, and 6 is the total BV with no Eph
clear all
run=[2 3 4 5 6 1];
%1=diode+bv 2=diode, 3=BV-all, 4=BV-Si, 5=BV-Pt, 6=BV-all-noEph
a=2;
bh=0.67; %barrier height V 0.73 vs 0.67 0.73
n=2; %Diode ideality factor
jl=[5]; %limiting current mA/cm2 0.2392

poredepth=000/10^7; %depth of pores (cm)
ptcoveragefrac=0.00; % percent coverage of Si surface by Pt particles
crossarea=1;
siareas=crossarea*1; %Si areas cm2 change this to alter roughness. otherwise, dont
touch
sicoveragefrac=0.0; %percent coverage by pores with no metal in them, dont typically
change
ptsize=150/10^7; %cm diameter of Pt particles
sisize=150/10^7; %cm diameter of pores without metal in them

rss=[000];%:4:32]; %solution resistance ohm SOLVES ITERATIVELY FROM PREVIOUS
```

```
SOLUTION. FOR HIGH RESISTANCE, GRADUALLY INCREASE FROM ZERO OHMS

for f=1:1
    %a=1;
    q=1.602176565*10^-19; %coulombs
    k=1.3806488*10^-23; %J/K
    Eo=0; %V vs RHE
    jpt=1; %exch current mA/cm2 Pt
    jag=10^-5; %exch current mA/cm2 Ag
    jsi=10^-9; %exch current mA/cm2 Si
    T=298; %K

    a_pt=0.5;  %alpha value for Pt
    a_si=0.5; %alpha values for Si
    e=2; %number of electrons per reaction

    sibase=pi*(sisize/2)^2;
    ptbase=pi*(ptsize/2)^2;
    ptareas=1*ptcoveragefrac*2; %HEMISPHERE Pt areas cm2 0.0659

    nsi=sicoveragefrac./sibase;
    npt=ptcoveragefrac./ptbase; %hemisphere
    porewall=(nsi)*(poredepth)*(sisize*pi)+(npt)*(poredepth)*(ptsize*pi);
    siareas=siareas-npt*ptbase+porewall;
    if sicoveragefrac > 0
        if ptareas==0
                porewall=(nsi)*(poredepth)*(sisize*pi);
                siareas=siareas+porewall;
        end
    end
    g=(siareas+ptareas)/crossarea; %set to 1 to remove
    rsh=Inf; %shunt resistance ohm (set to inf for no effect)
    Astar=1.2*10^6/100^2*1000; %mA/K^2/cm^2
    jo=Astar*T^2*exp(-q*bh/k/T);

end

for jj=1:length(jl)
    for r=1:length(rss)
        for l=1:length(siareas)
            for m=1:length(ptareas)
                for rr=1:length(run)
                    Asi=siareas(l);
                    Ac=crossarea;
                    Apt=ptareas(m);
                    Eph=n*k*T/q*log((jl(jj)/(jo*g))+1);
                    rs=rss(r);
                    il=-jl(jj)*Ac;
                    Ea=-1:0.005:0.9;
                    curin=zeros(size(Ea));
                    if exist('cur','var')==0
                        cur=zeros(size(Ea));
                    end
                    if isnan(sum(cur))==1
```

```
                        cur=zeros(size(Ea));
                    end
                    init=zeros(size(Ea));
                    for i=1:length(Ea)

                        init(i)=cur(i);

                        %diode
                        if run(rr)==2
                            curin(i)=1/(1/((Ac*(jo*g)*(exp(q*Ea(i)/k/T/n)-
1)+il+Ea(i)/rsh)))/Ac;
                            f=@(x) x-1/(1/((Ac*(jo*g)*(exp(q*Ea(i)/k/T/n)-
1)+il+Ea(i)/rsh)))/Ac;
                        end

                        %diodebv
                        if run(rr)==1
                            curin(i)=1/((1/((Apt*jpt*(exp(a_pt*e*q/k/T*(Ea(i)-Eo-
init(i)*Ac/1000*rs-Eph))-exp(-(1-a_pt)*e*q/k/T*(Ea(i)-Eo-init(i)*Ac/1000*rs-
Eph))))+(Asi*jsi*(exp(a_si*e*q/k/T*(Ea(i)-Eo-init(i)*Ac/1000*rs-Eph))-exp(-(1-
a_si)*e*q/k/T*(Ea(i)-Eo-init(i)*Ac/1000*rs-
Eph)))))+1/((Ac*(jo*g)*(exp(q*Ea(i)/k/T/n)-1)+il+Ea(i)/rsh))))/Ac;
                            f=@(x) x-1/((1/((Apt*jpt*(exp(a_pt*e*q/k/T*(Ea(i)-Eo-
x*Ac/1000*rs-Eph))-exp(-(1-a_pt)*e*q/k/T*(Ea(i)-Eo-x*Ac/1000*rs-
Eph))))+(Asi*jsi*(exp(a_si*e*q/k/T*(Ea(i)-Eo-x*Ac/1000*rs-Eph))-exp(-(1-
a_si)*e*q/k/T*(Ea(i)-Eo-x*Ac/1000*rs-Eph)))))+1/((Ac*(jo*g)*(exp(q*Ea(i)/k/T/n)-
1)+il+Ea(i)/rsh))))/Ac;
                        end

                        %bv_and_eph (bv+Eph shift)
%bv (no diode no photovoltage)
                        if run(rr)==3 || run(rr)==4 || run(rr)==5 || run(rr)==6
                            if run(rr)==4
                                Apt=0;
                            elseif run(rr)==5
                                Asi=0;
                            elseif run(rr)==6
                                Eph=0;
                            end
                            curin(i)=1/((1/((Apt*jpt*(exp(a_pt*e*q/k/T*(Ea(i)-Eo-
init(i)*Ac/1000*rs-Eph))-exp(-(1-a_pt)*e*q/k/T*(Ea(i)-Eo-init(i)*Ac/1000*rs-
Eph))))+(Asi*jsi*(exp(a_si*e*q/k/T*(Ea(i)-Eo-init(i)*Ac/1000*rs-Eph))-exp(-(1-
a_si)*e*q/k/T*(Ea(i)-Eo-init(i)*Ac/1000*init(i)*rs-Eph)))))))/Ac;
                            f=@(x) x-1/((1/((Apt*jpt*(exp(a_pt*e*q/k/T*(Ea(i)-Eo-
x*Ac/1000*rs-Eph))-exp(-(1-a_pt)*e*q/k/T*(Ea(i)-Eo-x*Ac/1000*rs-
Eph))))+(Asi*jsi*(exp(a_si*e*q/k/T*(Ea(i)-Eo-x*Ac/1000*rs-Eph))-exp(-(1-
a_si)*e*q/k/T*(Ea(i)-Eo-x*Ac/1000*rs-Eph)))))))/Ac;
                        end

                        cur(i)=fzero(f,curin(i));

                    end
                    hold on;
                    for i=1:length(Ea)
```

```
                        index=1;
                    end
                    name={'DBV' 'D' 'BV' 'BV-Si' 'BV-Pt' 'BV-noEph'};
                    if a==1
                        plot([Ea(1) Ea(end)],[0 0],'k:')
                        plot([Eo Eo],[-50 10],'k:')
                    end
                    %plot(Ea(1:end-index+1),cur(1:end-index+1),'LineWidth',
4,'DisplayName',[num2str(siareas(l)),':',num2str(ptareas(m)),', j_o = ',
num2str(jo),', r_s = ', num2str(rs),', j_l = ', num2str(il/Ac),', E_{ph} = ',
num2str(Eph),', run = ', char(name(run(rr)))]);
                    plot(Ea(1:end-index+1),Ac*cur(1:end-index+1),'k','LineWidth',
4,'DisplayName',[char(name(run(rr)))]);
                    a=a+1;
                end
            end
        end
    end
end

plotedit on
set(0,'defaultAxesFontName', 'Gill Sans MT')
set(0,'defaultTextFontName', 'Gill Sans MT')
%clear all
box on
xlabel('Potential [V vs. RHE]', 'FontSize', 16)
%ylabel('Current Density (mA/cm^2)', 'FontSize', 16)
ylabel('Current [mA]', 'FontSize', 16)

set(gcf,'Color',[1,1,1])
grid off
set(gca,'fontsize',25)
ax=gca;
ylim([-1.15*max(jl),0.15*max(jl)])%jo
ww=ax.LineWidth;
ax.LineWidth=2;
```